Lutz Winkelmann

Injection-locked high power oscillator for advanced gravitational wave observatories
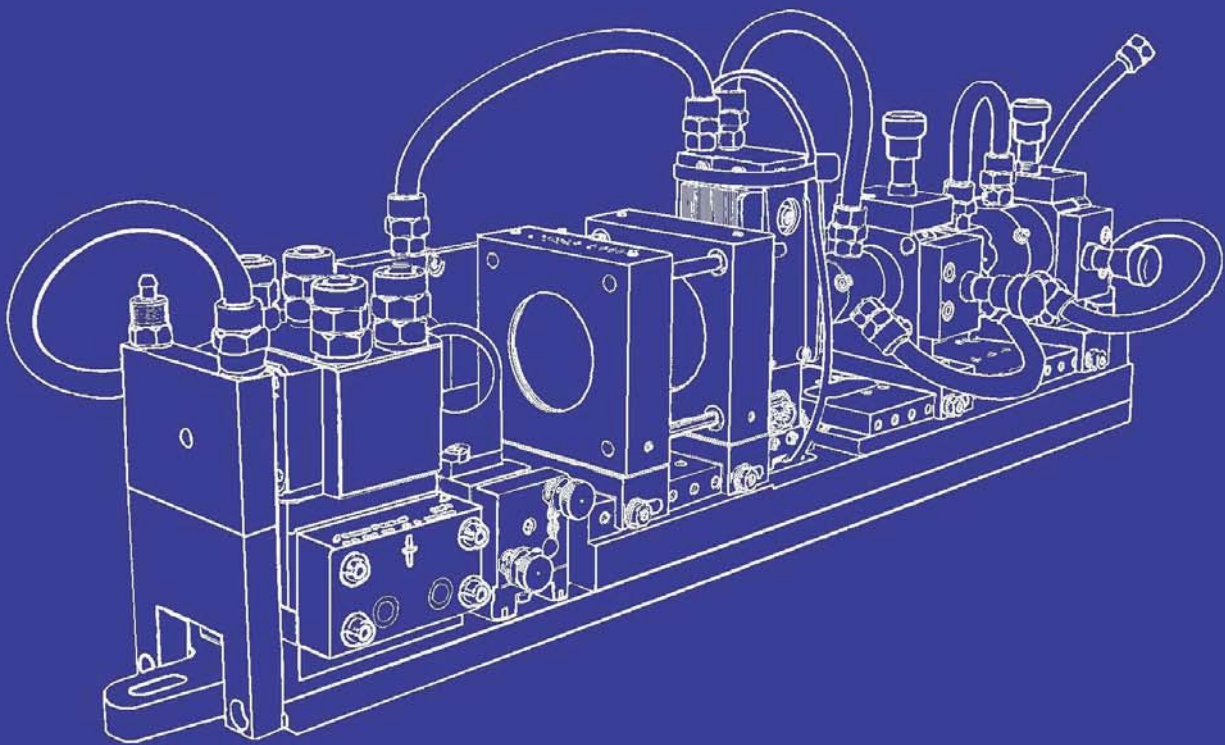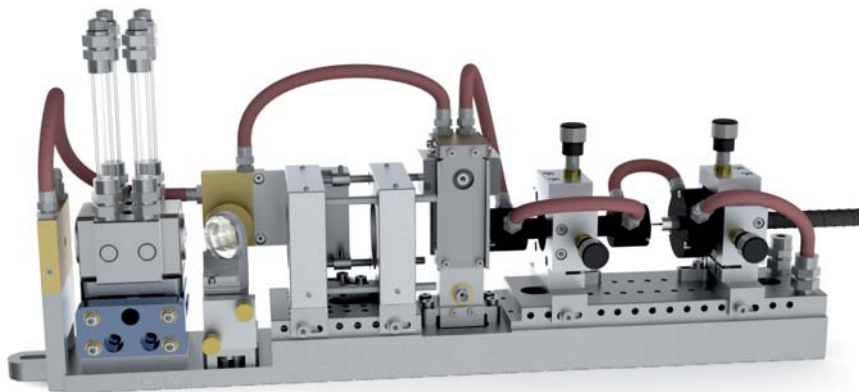
Injection-locked high power oscillator for advanced gravitational wave observatories

Injection-locked high power oscillator for advanced gravitational wave observatories

Injection-locked high power oscillator for advanced gravitational wave observatories

Von der Fakultät Maschinenbau
der Gottfried Wilhelm Leibniz Universität Hannover
zur Erlangung des akademischen Grades
Doktor-Ingenieur
genehmigte Dissertation
von

Dipl.-Ing.(FH) Lutz Winkelmann

geboren am 18.09.1979 in Oelde

2012

1. Referent:	Prof. Dr.-Ing. Ludger Overmeyer
2. Referent:	Prof. Dr. Uwe Morgner

Tag der Promotion: 10.04.2012

Kurzfassung

Eine Methode zum Nachweis der von Albert Einstein in seiner allgemeinen Relativitäts-theorie postulierten Graviationswellen stellen terrestrische, auf der interferometrischen Längenmessung basierende Observatorien dar. Die Reichweite dieser Detektoren ist zur Zeit auf maximal 15 Megaparsec (Mpc) beschränkt, da das Schrotrauschen innerhalb des Detektors im Frequenzband des Gravitationswellensignals (10 Hz – 10 kHz) die Empfind-lichkeit limitiert. Durch eine Ausgangsleistungssteigerung der Laserstrahlquelle kann eben diese Limitierung aufgehoben und die Empfindlichkeit um eine Größenordnung gesteigert werden. Somit wird die Wahrscheinlichkeit der Detektion einer Graviationswelle um den Faktor 1000 erhöht bzw. die Reichweite auf mehr als 150 Mpc erweitert.

Im Rahmen dieser Arbeit wurde zum ersten Mal ein Lasersystem demonstriert, das den hohen Anforderungen an Leistungs- und Frequenzstabilität, sowie Strahlqualität für die nächste Generation von Gravitationswellendetektoren genügt. Für das zu entwickelnde Lasersystem ist dabei ein zweistufiges Konzept vorgesehen. Es wird durch eine aktive Leistungs- und Frequenzstabilisierung ergänzt, die jedoch nicht Teil der vorliegenden Ar-beit ist. Ein 35 W Nd:YVO$_4$-Verstärkersystem mit einer Emissionswellenlänge von 1064 nm bildet die Frequenzreferenz und gleichzeitig den *Seed*-Laser für den mittels Injektions-skopplung angebundenen Hochleistungsoszillator. Der auf dem *Master Oscillator Power Amplifier* Konzept aufbauende 35 W Verstärker wird bereits in aktuellen Gravitation-swellendetektoren eingesetzt und hat sich dort im Langzeiteinsatz bewährt. Die hohe linear-polarisierte Ausgangsleistung von mehr als 200 W wird in der nachgeschalteten Oszilla-torstufe erzeugt, wobei diese aus vier in einem asymmetrischen Ringresonator angeordneten Nd:YAG Kristallen besteht. Zur Kompensation der durch thermisch induzierte Doppel-brechung in den longitudinal gepumpten Laserkristallen auftretenden Verluste wurde eine abbildende Depolarisationskompensation verwendet.

Zur Optimierung der Ausgangsleistung des Hochleistungsoszillators wurde ein numerisch-es Modell zur Berechnung der Resonatoreigenschaften eingesetzt. Dieses Modell und die darauf aufbauenden Untersuchungen bildeten die Grundlage für die Dimensionierung und mechanische Konstruktion des endgültigen Oszillators.

Bei der Kopplung von Laserquellen mittels der Injektionskopplung wird der Hochleistungs-oszillator durch Resonatorlängenanpassung mit der Trägerfrequenz des *Seeds*-Lasers aktiv in Resonanz gehalten. Veränderungen der Temperatur der mechanischen Komponenten bewirken eine Längenvariation, die sich störend auf die Kopplung beider Laser auswirkt. Zur Kompensation der thermischen Ausdehnung wurden verschiedene Modelle qualitativ betrachtet und eine geeignete Lösung bestehend aus angepasster Materialauswahl und ak-tiver Kühlung gewählt. Des Weiteren wurde ein zusätzlicher, langsamer Aktuator in die Regelung integriert, der eine Kompensation für Störungen wie Raumtemperaturänderun-gen und Luftdruckänderungen vornehmen kann.

Mit dem entwickelten Lasersystem war es möglich eine konstante Ausgangleistung von 220 W zu demonstrieren, wobei sich mehr als 165 W dieser Leistung innerhalb der fun-damentalen Grundmode befinden. Ausserdem wurden in Zusammenarbeit mit dem Albert Einstein Institut für Gravitationswellenphysik in Hannover die von der LIGO VIRGO Scientific Colaboration (LVC) aufgestellten Anforderungen zur Eignung des Lasers für die nächste Generation von Gravitationswellendetektoren (*Advanced LIGO*) demonstriert. Daher wird dieses Lasersystem ab Anfang 2011 als Strahlquelle in den weltweit größten Gravitationswellendetektoren eingesetzt werden.

Abstract

One approach to detect gravitational waves, which have been postulated by Albert Einstein in his General Theory of Relativity, is based on interferometric measurements of length variations with a large-scale Michelson interferometer. The detection range of these ground-based observatories is currently limited to approx. 15 Megaparsec (Mpc) because of a reduced sensitivity at detection frequencies of 10 Hz – 10 kHz by shot noise. These limitations can be overcome by an output power increase of the detector's light source, which will enhance the sensitivity by an order of magnitude. Thus, the possibility of detecting a gravitational wave will be raised by a factor of 1000 and the detection range will be increased to 150 Mpc, accordingly.

In this work a laser systems is presented, which fulfills the free-running laser requirements on stability and beam quality required by the next generation of gravitational wave detectors for the first time. The developed laser system is based on a two-stage concept, supplemented with an active amplitude and frequency stabilization, which is not part of this work. A 35 W Nd:YVO$_4$ amplifier system with an emission wavelength of 1064 nm represents the frequency reference of the laser system and is used as the seed for an injection-locked high power oscillator. This amplifier, which is based on a *Master Oscillator Power Amplifier* scheme, is already used in today's gravitational wave detectors and has been proven to be reliable in long-term operation. The linearly polarized output power of more than 200 W is generated inside the oscillator stage, which consists of four Nd:YAG crystals arranged in an asymmetric ring resonator configuration. To compensate for losses due to thermal birefringence inside the longitudinally pumped laser crystals, an imaging depolarization compensation is used.

To optimize the output power of the high power oscillator a numerical model was used to calculate the resonator properties. The results derived from this model combined with experimental data are the basis for the dimensions and mechanical design of the final oscillator setup.

For the injection-locking of the two laser sources, the resonator length of the high power oscillator has to be adapted and actively stabilized to be resonant with the incident seed frequency. Changes in temperature of the mechanical components result in length variations which will negatively affect the coupling of both laser systems. To compensate for this thermally induced elongation, various mechanical models have been qualitatively studied and an adequate solution consisting of a combination of adapted materials and active cooling was chosen. Furthermore, an additional slow actuator was included into the laser control, which compensates for room temperature and pressure variation induced distortions.

With the developed laser system a constant single-frequency output power of 220 W with more than 165 W in the fundamental mode was obtained. Furthermore, it was possible to fulfill the LIGO VIRGO Scientific Collaboration (LVC) free-running laser requirements for their next generation of gravitational wave detectors (advanced LIGO) in cooperation with the Max-Planck Institute for Gravitational Physics in Hannover. Thus, the installation of the presented laser system in the world largest terrestrial gravitational wave observatories started in spring 2011.

Contents

List of acronyms

Acronym	Definition
AOM	Acousto-Optical Modulator
ASE	Amplified Spontaneous Emission
BEM	Boundary Element Method
BP	Brewster Plate
BS	Beam Splitter
Caltech	California Institute of Technology
CCD	Charge-Coupled Device camera
CFD	Computational Fluid Dynamics
DAQ	Data AcQuisition
DC	Direct Current
DI	DeIonized
EOM	Electro-Optical Modulator
ET	Einstein Telescope
ETM	End Test Mass
FC	Fiber-optic Connector
FDM	Finite Difference Method
FEM	Finite Element Method
FI	Faraday Isolator
FPC	Fabry-Perot Cavity
FSR	Free Spectral Range
FSS	Frequency Stabilization Servo
FWHM	Full-Width Half-Max
GW	Gravitational Wave
GWD	Gravitational Wave Detector
HA	Halo Aperture
HF	High Frequency
HPFI	High Power Faraday Isolator
HR	Highly Reflective mirror
HV	High Voltage
IBS	Ion-Beam Sputtered
IL	In-Loop
IL-PD	Injection Locking PhotoDiode

Acronym	Definition
Inj.-Lock.	Injection-Locked
INVAR	InVariant low expansion nickel-iron alloy
ISS	Intensity Stabilization Servo
LAE	Laser Area Enclosure
LDB	Laser Diode Box
LDR	Laser Diode Room
LF	Low Frequency
LG	LaGuerre mode
LH	Laser Head
LIGO	Laser Interferometer Gravitational wave Observatory
LRA	Long Range Actuator
LVC	LIGO Virgo Scientific Collaboration
LXT	Low-eXTractable piping supplied by Harvel Plastics Inc.
LZH	Laser Zentrum Hannover e.V.
MACOR	Corning machinable glass ceramic
MIT	Massachusetts Institute of Technology
MM	Mode-Matching
MOPA	Master Oscillator Power Amplifier
NA	Numerical Aperture
N-BK7	SCHOTT crown glass
Nd:YAG	Yttrium Aluminum Garnet doped with Neodymium ions
Nd:YVO$_4$	Yttrium ortho-Vanadate doped with Neodymium ions
NPRO	Non-Planar Ring Oscillator
NS	Neutron Star
OC	Output Coupler
OOL	Out-Of-Loop
OPD	Optical Path length Difference
PCX	Plano-ConveX lens
PD	PhotoDiode
PDH	Pound-Drever-Hall
PID	Proportional, Integral and Differential controller
PL	Pump Light
PM	Power Meter
PMC	Pre-Mode Cleaner
POM	PolyOxyMethylene

Acronym	Definition
PRM	Power Recycling Mirror
PSL	Pre-Stabilized Laser
PTFE	PolyTetraFluorEthylene
PZT	PieZoelectric Transducer
QR	Quartz Rotator
S	Shutter
SBS	Stimulated Brillouin Scattering
SMA	SubMiniature version A fiber connector
SPC	Stored Program Control
SRM	Signal Recycling Mirror
TEC	ThermoElectric Cooler
TEM	Transverse ElektroMagnetic
TFP	Thin Film Polarizer
UHV	Ultra-High Vacuum
US	United States
USA	United States of America
VNC	Virtual Network Computing connection

List of symbols

Symbol	Unit	Definition
α	cm^{-1}	Linear absorption coefficient
A, B, C, D		Elements of the transfer matrix of an optical element/system
$\alpha_{eff}(z)$	cm^{-1}	Effective absorption coefficient at the position z
$\alpha(\lambda)$	cm^{-1}	Wavelength dependent linear absorption coefficient
$\alpha(T)$	K^{-1}	Temperature dependent linear thermal expansion coefficient
$a(t)$	m/s^2	Acceleration
β		EOM modulation index
β_i	rad	Phase thickness for a layer of a thin film coating
bpp	mm mrad	Beam parameter product
c	m/s	Speed of light
$C_{r,t}$		Constants for the radial and tangential stress components
C_w	Ws/(kg °C)	Specific heat of the coolant
$\Delta\Phi(t)$	rad	Phase shift generated by a GW passing through the interferometer
$\delta\Phi$	rad	Phase shift generated by a frequency fluctuation of the laser light
D_1	m	Laser crystal rod diameter
$D_2(l)$	m	Variable flow tube diameter at the axial position l
ΔL	m	Length difference between L_x and L_y
$\delta\nu$	Hz	Frequency difference in respect to the laser's carrier frequency
$\frac{dn}{dT}(T)$		Temperature dependent refractive index variation
$d(z)$	m	Distance of a light ray from the optical axis
η	%	Photodetector efficiency

Symbol	Unit	Definition
η_h	%	Fractional thermal loading coefficient
$E_c(z)$		Electromagnetic field of the slave oscillator inside the cavity
E_i		Electromagnetic field of the master laser beam with modulated sidebands
E_M		Electromagnetic field of the master laser beam
E_m		Electromagnetic field of the transmitted master laser beam
E_r		Electromagnetic field of the reflected master laser beam
E_t		Electromagnetic field of the slave oscillator coupled out of the cavity
f	Hz	Frequency
f	mm	Focal length of a lens
$F(t)$	N	Force
G	Nm^2/kg^2	Gravitational Constant
g_{total}		Combined gain
$\hbar$	Js	Planck's constance
h		Relative length displacement or GW strain
J_n		Bessel function of the order n
k	m^{-1}	Propagation constant
$K(T)$	W/(m K)	Temperature dependent thermal conductivity
K_w	W/(m °C)	Thermal conductivity of the coolant
λ	nm	Wavelength
λ_{air}	W/(m^{2}K)	Heat transfer coefficient for laminar flowing air
λ_k	W/(m^{2}K)	Heat transfer coefficient
λ_p	nm	Wavelength of the pump light
∇^2		Laplace operator
L	m	Length
L^l_p		Laguerre polynomial with p and l representing the radial and angular mode number

Symbol	Unit	Definition
$L_{x,y}$	m	Length of the corresponding interferometer arm
μ	kg/(m s)	Fluid viscosity
m	kg	Mass
$M_\odot$	kg	Solar mass
M^2		Beam quality factor
ν_L	Hz	Carrier frequency of the laser
$N_{Pr}(l)$		Variable Prandtl number at the axial position l
$N_{Re}(l)$		Variable Reynolds number at the axial position l
ν		Poisson's ratio
$\vec{n}$		Surface normal vector on the cylindrical surface of the laser crystal
n_0		Refractive index
n_w		Refractive index of water
$n_{Nd:YAG}$		Refractive index of Nd:YAG
$OPD(r)$	m^{-1}	Optical path length difference at a radial position r
$OPD_{fit}(r)$	m^{-1}	Parabolic fit of the optical path length difference at a radial position r
π		Ludolph's constant
$\phi(z)$	rad	Gouy phase
$\Phi_{pl}(z)$	rad	Gouy phase of a Gaussian Laguerre mode with order pl
$\phi(z)$	rad	Divergence angle
$p_{i,j}$		Photo-elastic coefficients for Nd:YAG
$p(\lambda, z)$	W/nm	Spectral power distribution at the position z
P_{BS}	W	Power at the beam splitter inside the interferometer
P_{in}	W	Integrated total incident pump power
P_M	W	Master laser incident power
P_S	W	Slave oscillator output power
$\psi(x, y, z)$		Paraxial approximation of the electromagnetic field of the coherent laser light

Symbol	Unit	Definition
$P(z)$		Complex phase shift
$Q(r, z)$		Thermal power density
Q_s		Quality factor for the slave oscillator cavity
$q(z)$		Complex beam parameter
ρ	kg/m^3	Mass density
R	m	Distance to the Earth
R	m	Laser crystal radius
R	%	Reflectivity of a thin film coated glass substrate
$R(z)$	m	Wave front curvature
r	m	Radial position inside the laser crystal rod
r_0	m	Distance between two stars
r_0	m	Laser crystal radius
$r_{S1,S2}$	m	Schwarzschild radius of the corresponding star
$S_0 - S_3$		Components of the Stokes vector
$s(t)$	m	Travel length
τ_s	s	Light storage time
T	K	Temperature
$T\|_0$	K	Temperature at the surface of the laser crystal
T_k	K	Coolant temperature
$T(r, z)$	°C	Temperature at the radial position r and axial position z inside the laser crystal
θ		Phase shift per round trip
u	m/s	Fluid velocity
$u(x, y, z)$		Electromagnetic field or potential of the coherent laser light
V	m/s	Speed of the laminar air flow
Ω	MHz	Sideband modulation frequency
ω_0	m	Beam waist
$\omega_p(z)$	m	Beam waist of the pump light at a position z
ω_{p0}	m	Smallest beam waist of the pump light
$\omega_{pl}(z)$	m	Beam waist at the position z for a Gaussian Laguerre mode with the order pl

Symbol	Unit	Definition
x, y, z		Cartesian coordinates
z	m	Position along the z-axis
z_0	m	Start and end point for the calculation of the round trip matrix
z_c	m	Rayleigh range

Chapter 1

Introduction

When Albert Einstein postulated his General Theory of Relativity, his main intention was to overcome the limitations of Newton's Theory of Gravity [Ein15]. One solution of the equation of general relativity revealed the theoretically existence of gravitational waves [Ein16]. These waves are ripples in space-time that travel at the speed of light. Even though these waves pass through the Earth on a daily basis most of them are much too weak to be ever noticed or detected. Only waves with a very high amplitude, created by high-mass stellar objects, like neutron star - neutron star binaries, massive black holes or collapsing massive stars, are detectable to us.

Although no detection of gravitational waves has been successful so far, various scientists over the past 80 years were eager to measure these waves as a direct experimental proof of Albert Einstein's theory. The first major break through was done when Russell Hulse and Robert Taylor investigated a pair of pulsars (PRS 1913 + 16) spinning around each other [Hul75, Tay76]. These pulsars send out a detectable radio burst that hits the Earth every 7.75 h. Measuring the period of this signal over a long time scale they found that the pulsars were slowly drawn together. The energy lost during this process perfectly fitted the predicted energy loss caused by gravitational waves. For these experiments both scientists were awarded with the Nobel Prize in Physics in 1993.

Today technological evolution has made huge progress, so that the detection of gravitational waves is within reach. Large-scale Michelson interferometers with arm lengths of up to 4 km achieve sensitivities for gravitational waves that could lead to the first detection. Measuring the distance between quasi free falling mirrors (in direction of the propagating beam), called test masses inside the L-shaped interferometer arms, a displacement sensitivity of 10^{-22} per meter per root Hertz could be demonstrated, recently [Abb09].

The largest detectors of this type are the ***Laser Interferometer Gravitational wave Observatories*** (*LIGO*). Built by a collaboration of the Californian Institute of Technology (Caltech) and the Massachusetts Institute of Technology (MIT) three detectors are operated today. Two of these are located at Hanford, Washington state, and share one building. One detector with two 4 km long arms between beam splitter and the test masses and one with 2 km. Separated by 3000 km, located at Livingston, Louisiana, a third detector with 4 km arm length was constructed. These detectors are the most sensitive for gravitational waves today.

In theory, two interferometers would be sufficient to detect gravitational waves and confirm the authenticity by a coincidence measurement. Nevertheless, a deeper insight into the origin, orientation and polarization of these waves is only gained by having more than two detectors. Therefore, different groups around the world working in the same field and with their own observatories, joint together and formed a collaboration called LIGO Virgo Scientific Collaboration (LVC). Amongst these detectors are the French-Italian detector Virgo (3 km arm length) near Pisa, Italy, the German-British detector GEO600 (600 m arm length) near Hannover, Germany and TAMA300 (300 m arm length), built and located in, Tokyo, Japan.

Even though a detection is possible with the sensitivity of the today's LIGO, a plan to increase the sensitivity and hence the detection range for theses observatories was developed during the last years, called *Advanced LIGO* [Fri08]. Various groups all over the world will supply the latest in technology for this major upgrade until the end of 2014. One limitation in the interferometric detection of length variations in the sub attometer scale is the photon shot noise. As shot noise level decreases proportionally to the light source power an increase in output power of the laser system used is desired. To increase the sensitivity by a factor of 10 from LIGO to Advanced LIGO, a significant increase in laser output power is needed. Calculations showed that 200 W of light emitted from such a laser source would be sufficient (taking losses for active stabilization, filter cavities, and for sideband modulation, etc. into account).

To increase the circulating power inside the arms of the interferometer and therefore the light's storage time, resonant high-finesse Fabry Perot cavities are installed. Additional power and signal recycling mirrors furthermore increase the circulating power to a maximum of 800 kW (for Advanced LIGO) [Har10]. To couple a laser beam in such a resonant large scale cavity, the beam profile has to have a pure Gaussian shape. In addition, the emitted light should only oscillate at one single frequency.

Within the second chapter of this work, an up-to-date description of the current and future LIGO detectors is given. Considering the development of the Advanced LIGO

Project during recent years, the final design requirements for a laser system for this gravitational wave detector are presented. This section is followed by an overview of the underlying technological background which led to the development of the first laboratory laser prototype by Frede et al. [Fre05b]. Additionally, an overview of the laser technology, which is actually installed and operated inside the various observatories is given. At the end of this chapter, the final design laser concept, which was chosen as the light source for Advanced LIGO, is described.

In chapter three, the theoretical background needed for the optimization of the laser system for Advanced LIGO is presented. First of all, the thermal effects inside the laser active media of a high power laser system are reviewed and two methods to obtain numerical results for the thermal lens within the laser crystals are given. With these results, a numerical model for the resonator stability and internal mode diameters is developed. The results obtained can then be used to predict the best operation point of a given dynamically stable laser configuration and for further optimization of the resonator. Furthermore, the Pound-Drever-Hall injection-locking technique is discussed, which was used to achieve a high output power in a single longitudinal mode by coupling the high power oscillator to a low power seed.

The theoretical guidelines derived with the previously mentioned models were then incorporated in the development process of the injection-locked high power oscillator. Prior to that, experimental results used to verify the suitability of an asymmetric resonator configuration for higher-order mode discrimination are presented. Based on the derived experimental data and the numerical calculations an optical setup for the high power oscillator is presented in chapter four. The derived optical scheme was then implemented into a mechanical design for the high power oscillator, which was optimized for long term operation and high stability. To compensate for thermal effects, which greatly influence the mechanical structure and thus the alignment of the laser, a cooling scheme was developed and verified by simulations and thermo optical measurements.

In chapter five all results of a full characterization of the injection-locked laser system for Advanced LIGO are presented. In contrast to industrial high power Nd:YAG lasers it is not sufficient for a laser system designed for a gravitational wave detector to measure output power and beam quality only. Special attention is paid to the power and frequency noise characteristics of the laser and especially the higher-order mode content of its output beam. Furthermore, the injection locking behavior, which has a strong impact on the long term stability of the laser system, is examined in more detail. For a concluding performance overview a short section with the latest output characteristics of the actively stabilized laser system is given. Even though

these results were not generated as part of this work, they will contribute to a more detailed overview of the laser system's performance.

As described in the previous section, the laser system fulfilled the requirements and is currently installed as the next generation light source inside the Advanced LIGO observatories. From the design descriptions and pictures in this manuscript one will see that the complete laser system is a fairly large and complicated assembly. To deliver and install such a delicate optical laser system to the United States, extensive planning and foresight during the mechanical development of the laser was needed. Therefore, a short overview of the shipping procedure, on-site installation and support is given in the outlook section of this work.

Even though the development of advanced gravitational wave detectors will result in the detection of such waves on a yearly basis, a detailed description of astrophysical phenomena will need a more sensitive detection method for the future. Although, the newest generation of LIGO detectors and others are not operational at this time, a project to build a third generation detector called *Einstein Telescope* was formed. This Earth bound observatory also relies on an interferometric detection of length variations caused by gravitational waves, but with much higher sensitivity. For this observatory, new lasers with even higher output power levels in a fundamental mode beam or in a different wavelength regime are desired. As a foresight what comes next in the field of gravitational physics, an outlook of these new technologies is presented in chapter six.

At the end of this work a conclusive overview of the achievements during the development of the Advanced LIGO high power oscillator will be given in chapter seven.

Chapter 2

Light sources for gravitational wave detectors

The essence of Albert Einstein's General Theory of Relativity is that mass and energy produce a curvature of four-dimensional space-time, and that all matter will move in response to that curvature. Similar to Maxwell's equation describing the interaction of an electric charge and an electromagnetic field, Einstein's equations characterize the interaction of mass and space-time curvature. Gravitational waves (GW) are time-dependent vacuum solutions for curvatures field equations. A similar structure can be seen in Maxwell's time-dependent in vacuum solution, which describes electromagnetic waves. GWs can be imagined as ripples or strain oscillations perpendicular to a reference flat, or Minkowski, space-time metric.

Experimentally, the variation of this metric could be detected as a delay of light traveling from one free falling test mass to another. If the orientation of these test masses is well adapted to the orientation of the GW, the relative distance change can be described as [Sau94]

$$\frac{\delta L}{L} = \frac{|h|}{2}, \tag{2.1}$$

with h being the amplitude of the GW or GW strain, as it describes the fraction of stretch and compression of the space-time. Similar to electromagnetic waves, GWs travel at the speed of light. Because their interaction with the surrounding masses is relatively low, they can pass objects without being perturbed. In comparison to electromagnetic waves, which are dipole in nature, GWs are quadrupole. This means that the strain pattern of these waves contracts and stretches space-time along the propagation pass. The transverse strain field of the GW comes in two different polarizations. The basic +-polarization and the rotated by 45° ×-polarization can be observed. Normally, the astrophysical GW comprises both orientations.

As mentioned above, the interaction of gravitational waves with matter is very weak. From astrophysical considerations, the largest strain that can reach the Earth would have to be produced by a catastrophical event, such as a nearby supernova or the merging of two black holes. Estimates say that this strain could reach levels of $h \approx 1 \cdot 10^{-18}$. As such events are very rare, an approximation of the amplitude and hence displacement generated by a gravitational wave which is more likely to be detected on a daily basis was performed. Therefore the amplitude h of a GW that is created by two neutron stars (NS) orbiting around each other in a distance R to the Earth can be described as [Sau94]

$$h \approx \frac{r_{S1} r_{S2}}{r_0 R}, \tag{2.2}$$

with r_0 the distance in between the two stars and $r_i = 2GM_i/c^2$ the corresponding Schwarzschild radii. As an example the gravitational constant is given as $G = 6.67259 \cdot 10^{-11} \text{Nm}^2/\text{kg}^2$ and the mass of one of the two stars is 1.44 times the solar mass $M_\odot = 3 \cdot 10^{30}$kg. With a distance of 50 million light years located in the Virgo cluster these NS binary stars rotate within a distance of 80 km to each other. Under these conditions the estimated GW strain would be $h \approx 1 \cdot 10^{-21}$. Hence the sensitivity of a gravitational wave detector (GWD) should be in the range of $h \approx 1 \cdot 10^{-21}$ to $h \approx 1 \cdot 10^{-22}$. This corresponds over a distance of 1 km to a length displacement of 1 – 10 attometers. The first attempts to measure a GW were made by Weber in 1960 [Web60]. For his detector he used a large (approximately 1 t) aluminum cylinder, hanging suspended in a vacuum chamber. A GW that passes through the detector will cause the cylinder into oscillate. These oscillations can be detected by high precision transducers attached to the cylinder. With this setup a GW strain sensitivity of $h \approx 1 \cdot 10^{-16}$ was achieved. With the development of new cooling techniques to temperature levels of 0.1 K for the oscillating cylinder the sensitivity of these GWD was improved significantly [Ast97]. Even though the sensitivity of this device is in the range to detect a GW it only has the ability of detecting these waves at discrete resonant frequencies.

To measure in a more broadly spread range of frequencies and thus increase the probability of detecting a GW, a concept based on the optical measurement of length variations was chosen. Used to study the impact of the ether on light waves by Michelson in 1881 and further on in a more sensitive experiment by Michelson and Morley in 1887 [Mic87], a light interferometer was developed. Based on the ability to measure length deviations of two orthogonal arms with high precision, Pirani, Weiss and Forward proposed the use of an interferometer as a gravitational wave antenna [Pir56, For78, Wei72].
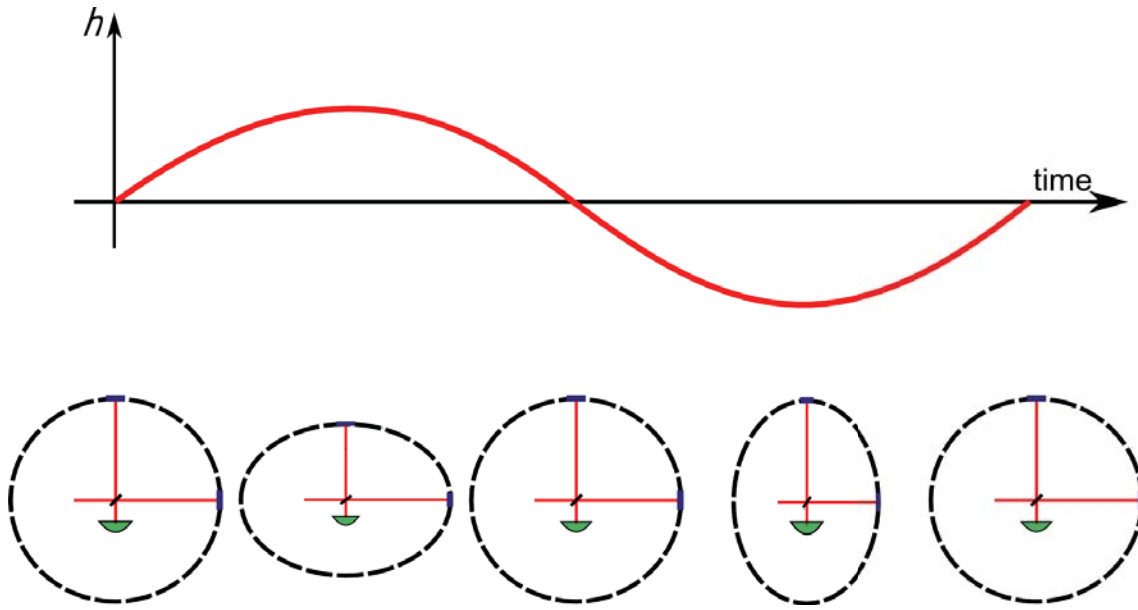
Figure 2.1: Gravitational wave with the strain h perpendicular to the plane of the diagram. A figurative circle of particles around a Michelson interferometer is transformed into an ellipse. One arm gets elongated during one half-cycle while the other gets compressed. In the next half-cycle the other direction is stretched and the orthogonal one compressed. The oscillation can be measured as a light modulation at the output of the interferometer (**green**).

In a Michelson interferometer the injected light is divided by a beam splitter into two beams traveling in orthogonal directions. These two rays are reflected by mirrors and interfere when being overlapped at the beam splitter. If a GW passes the interferometer the arm lengths are compressed or stretched, respectively. In Fig. 2.1 an incident GW with a sinusoidal oscillation and its impact on the interferometer is shown. Sending light with a single frequency into the interferometer, a phase shift of

$$\Delta\Phi(t) = \frac{4 \cdot \pi \cdot L}{\lambda} \cdot h(t), \tag{2.3}$$

corresponding to strain $h(t)$ of the GW can be detected at the output. To increase the signal to noise ratio the arm lengths of the basic Michelson interferometer configuration are chosen so that the light will interfere destructively at the output port. Under this so called *dark fringe condition* the phase modulated sidebands, which are caused by the passing GW, will interfere constructively with an amplitude depending on the GW strain, as shown in Fig. 2.2.
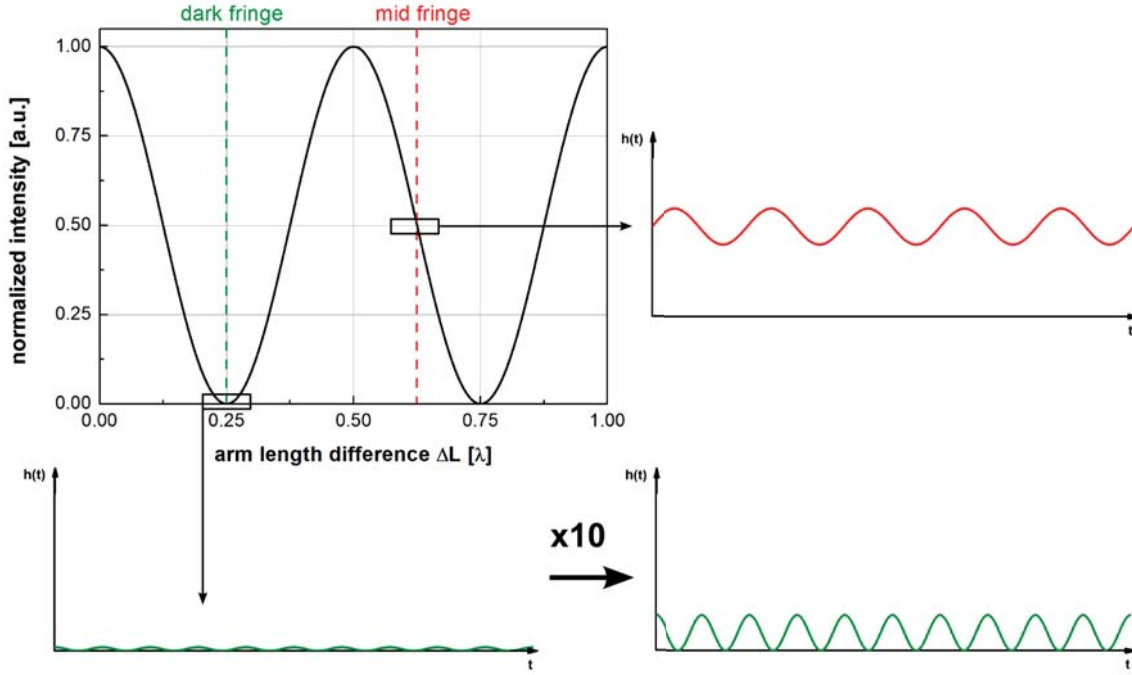
Figure 2.2: GWD response to a differential displacement of the interferometers end masses to a gravitational wave in dark fringe condition.

To increase the sensitivity of the interferometer for GW signals additional changes apart from the standard Michelson configuration have been introduced. Two different parameters of the interferometer configuration have a direct very high impact on the sensitivity of the detector: the power incident on the beam splitter and the light storage time inside the interferometer. Both parameters reduce the limiting sensing noise above 10 Hz, which is dominated by shot noise. The ideal shot noise limited strain can be described as [Abb09]

$$\tilde{h}(f) = \sqrt{\frac{\pi\hbar\lambda}{\eta P_{BS}c}} \frac{\sqrt{1 + (4\pi f \tau_s)^2}}{4\pi\tau_s}, \tag{2.4}$$

where η is the photodetector's efficiency, f the GW-frequency, λ the wavelength of the light-source, τ_s the light storage time, P_{BS} the laser power at the beam splitter, $\hbar$ the Planck's constance, and c the speed of light. To raise the light storage time τ_s, resonant Fabry-Perot cavities (FPC) are installed in each of the interferometer's arms as shown in Fig. 2.3. These cavities cause the light to perform several round-trips in the arms, which increases the carrier power and phase shift for a given GW strain amplitude and frequency [Mue03]. To scale the power inside the detector even more a scheme, called power recycling, is applied. When the Michelson interferometer is operated in the *dark fringe configuration* all optical power reflected from the end

test masses / mirrors (ETM) of the detector arms is send back in direction of the light source. To recycle this power a power recycling mirror (PRM) is placed in between the light source and the beam splitter (BS).
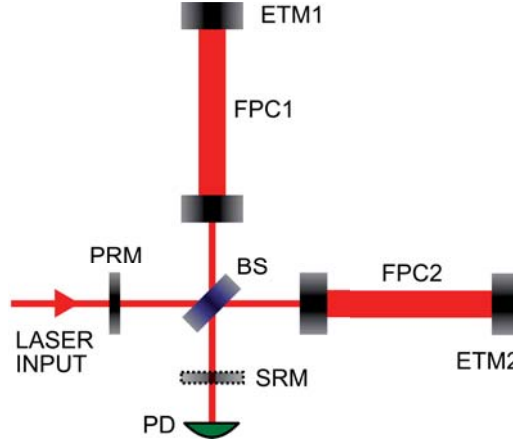

Figure 2.3: Schematic of the LIGO interferometer with end test masses (ETM1 and ETM2), Fabry-Perot cavities (FPC1 and FPC2), beam splitter (BS), power recycling-mirror (PRM), signal recycling mirror (SRM) and photodetector (PD).

Another method of increasing the sensitivity is the installation of a signal recycling mirror (SRM) [Str91, Hei98]. First introduced in the GEO600 detector, it sends the sidebands produced by GWs back into the interferometer. Inside the detector the signal is amplified even more, picking up more phase from the passing GW. Additionally this scheme offers one the ability to control the frequency range, in which the detector is most sensitive to GW [Wil02]. Although this mirror was not included in the LIGO detectors, it is planned to be installed in Advanced LIGO [Fri08].

Besides these sensitivity scaling techniques for the interferometric GWDs, much more technical issues have to be solved to achieve the performance of today's gravitational wave observatories. Seismic isolation, featuring multiple pendulum constructions, isolate the test masses from the Earth's motion to guarantee the quasi free-falling characteristic in the direction of the propagating laser beam. The mirrors themselves are temperature controlled and positioned by actively stabilized contact-free actuators. All beams and optics are positioned into vacuum to compensate for air fluctuations coupling into the detector's signals. This vacuum system for LIGO, with its tubes running 4 km in one and 4 km in the other direction, is the largest ultra-high vacuum (UHV) system in the world. In fact, various groups all over the world worked with much effort to reach the initial LIGO sensitivity of $h = 3 \cdot 10^{-22}$ at 100 Hz.

2.1   Laser requirements

From Eq. (2.4) in the previous section one can see that the shot noise of a GWD is directly proportional to the inverse square root of the power incident on the beam splitter. This power is directly defined by the laser power that is coupled through the power recycling mirror into the interferometer setup. Because the arms of the Michelson interferometer are equipped with resonant high Finesse Fabry-Perot cavities, only laser beams with a pure Gaussian intensity profile oscillating in a single longitudinal mode can be used. To guarantee that the light incident on the beam splitter has a pure TEM_{00} beam profile, passive filtering cavities are installed upstream of the entrance window to the interferometer input [Wil98].

For the next generation of the LIGO GWD – Advanced LIGO – a laser output power increase of a factor of 20 compared with the laser used in the initial setup is desired. First estimations showed that a power level of 125 W at the beam splitter is needed to achieve a significant reduction of the limiting shot noise of the GWD. With a light source capable of supplying such power levels in a single-frequency pure TEM_{00} beam, the sensitivity for the detection of inspiral NS-NS binaries can be increased by a factor of 10 compared with the initial detector [Fri08]. Consequently, this will lead to a 1000 times higher detection rate for GWs.

In fact, an output power of more than 165 W in a pure Gaussian intensity distribution is needed to compensate for the losses at the input of the interferometer and for the generation of side bands, which are required for interferometer control loops. This sets the power requirements for a laser system for Advanced LIGO to more than 200 W of output power in a single-frequency fundamental mode. As specified, only 10% of this power can be tolerated in higher-order modes. These higher-order modes can be filtered out by passive filter cavities directly after the laser system and in front of the interferometer input.

Besides the output power and modal characteristic of the laser beam, the fluctuations of the laser frequency and power are limiting factors in optical GWDs. A frequency shift of the laser light inside the Michelson interferometer causes a phase shift at the output port. For an interferometer with arms having exactly the same length, this differential effect would cancel out. Unfortunately, it is technically not possible to build a 4 km Michelson interferometer with equal arm length. When an arm length difference of $\Delta L = L_x - L_y$ is assumed, the frequency differences $\delta\nu$ of the laser with a carrier frequency ν_L causes a phase shift

$$\delta\Phi = \frac{2\pi}{c}\left[\delta\nu\Delta L + \nu_L\delta\Delta L\right], \tag{2.5}$$

which directly couples into the GW-detection signal as described in the previous section. Thus, the signals from the frequency fluctuations have to be kept lower than that caused by the arm length variation δL caused by a passing gravitational wave. Estimations of this value over the detectors frequency range led to a requirement for the frequency stability of the laser system which is given in Table 2.1. Furthermore, a Michelson interferometer can only be tuned to the dark fringe operation point described in the section above to a certain extent. Because of small offsets inside the electronic control loops, which keep the interferometer locked at the dark fringe point, small phase offsets are generated. In combination with a slightly mis-aligned beam, imperfect coatings of the test mass surfaces and the radiation pressure on these masses, laser output power variations can couple into the phase signal of the interferometer, causing a frequency dependent strain variation. As a consequence, the requirements for laser output power variations are well defined. Presumed values for the power fluctuations of the laser beam for specific frequency ranges of the GWD can be found in the requirement Table 2.1 as well.

Parameter	Specifications
wavelength	1064 nm
output power	> 200 W
power in higher-order modes	< 20 W
frequency fluctuations	$< 1 \cdot 10^{4} \mathrm{Hz}/\sqrt{\mathrm{Hz}} \cdot [1 \ \mathrm{Hz}/f]$ between 1 Hz and 10 kHz (same as NPRO free running)
relative power fluctuations	$< 10^{-2}/\sqrt{\mathrm{Hz}}$ between 0.1 Hz and 10 Hz $< 10^{-5}/\sqrt{\mathrm{Hz}}$ between 10 Hz and 10 kHz $< 3.6 \cdot 10^{-9}/\sqrt{\mathrm{Hz}}$ for $f > 9$ MHz (3 dB above shot noise of 50 mA photocurrent)

Table 2.1: Target specifications for the final free-running Advanced LIGO laser.

To understand the development process for the Advanced LIGO laser presented in this work, one has to distinguish between a free running laser system and an actively stabilized laser. With a free running laser, the requirements regarding frequency and amplitude noise given by the system parameters of the Advanced LIGO detector are not achievable. To reach the desired specifications of the laser an active stabilization scheme developed by the Max Planck Institute for Gravitational Physics in Hannover is applied to the laser system described in this work. Even though all data presented in this work are only related to the free running laser, special consideration was

taken during the development process to be able to reach the requirements for a stabilized laser in the end.

Besides the specifications given in Table 2.1 the laser system has to be operable in an environment with a varying temperature of 3 K peak-to-peak and a pressure variation of 50 hPa around the average atmospheric pressure. The requirements for long term stability can be derived from the intended availability of 90% of the GWDs with a minimal continuous period of operation of 40 hours over many years. Therefore, special attention was paid to the mechanical and optical design of the laser system, which influences the long-term stability and the ease of maintenance.

2.2   Best available laser technology in GWDs

Various different laser light sources are used inside ground-based GWDs around the world. All of these laser systems have one thing in common: They use a highly stable single crystal laser as frequency reference. These non-planar ring oscillators (NPRO) are based on a monolithic ring resonator design, where the cavity is formed inside the active media [Kan85]. Because of the laser's fairly small resonator length, the emitted light is oscillating with a single frequency. Furthermore, the laser line width of a few kHz of these devices is advantageous for the development of a laser for GWDs.

Unfortunately, the output power of commercially available laser's based on this design is limited to approximately 2 W. To further increase the optical power two different approaches have been followed. The first is the direct amplification, passing the beam through multiple active media. In this so called *Master Oscillator Power Amplifier* (MOPA) configuration the NPRO serves as the frequency and beam profile reference and though is the *Master Oscillator*. In most cases the *Power Amplifier* consists of longitudinally pumped solid-state laser crystals, in which the low power beam of the *Master Oscillator* gets amplified in a single pass. As active media for this kind of amplifier $Nd:YVO_4$ was found to be most suitable. Offering a very high gain it is widely used in MOPA systems.

The second approach, injection locking, is based on the resonant coupling of a high power oscillator to a low power seed laser. For this purpose, a piezo actuated mirror is introduced into the high power oscillator's cavity. Moving the piezo actuated mirror, the resonance frequency of this cavity is brought near the carrier frequency of the injected low power seed. At that point, the good frequency properties (longitudinal single-frequency, low frequency noise, etc.) are imprinted on the high power beam. The injection-locking process of both laser systems is performed by an automated

analog servo system following the Pound-Drever-Hall (PDH) scheme [Dre83]. In most cases ring lasers with two or more laser crystals are used as high power oscillators. As active media Nd:YAG and Nd:YVO$_4$ are the most common. However, the thermal properties of Nd:YVO$_4$ make its use for high power laser systems above the 100 W level unfeasible.

A list of all laser systems used in today's GWDs and their concept is given below in Table 2.2.

Detector	Gain media	Concept	Output power	Reference
Initial LIGO	Nd:YAG	MOPA	10 W	[Sav98]
Enhanced LIGO	Nd:YAG+Nd:YVO$_4$	MOPA	35 W	[Fre07b]
Virgo	Nd:YVO$_4$	Inj.–Lock.	20 W	[Ace08]
GEO600	Nd:YAG	Inj.–Lock.	10 W	[Zaw02]
TAMA300	Nd:YAG	Inj.–Lock.	10 W	[And05]

Table 2.2: Overview of laser systems used in Earth bound gravitational wave detectors.

Both concepts, injection locking and the MOPA design, offer different advantages and disadvantages. From the technical side the MOPA concept is the most reliable and easiest to maintain, because it does not use an active resonator length stabilization scheme. Furthermore, fluctuations of the surrounding environment (temperature, air pressure and humidity) have a lower impact on the output performance compared to a laser with a length stabilized cavity. Unfortunately, the output power achievable with solid-state MOPA systems is limited, because the beam gets distorted by the thermal lens in each laser crystal, picking up more and more distortions with every additional active media of a multi-stage amplifier. By comparison, high power oscillators in an injection-locked system offer a beam filtering ability due to their resonator. For this reason, Frede et al. decided at the beginning of the design and development process of a laser system for the next generation of LIGO to combine a high power solid-state oscillator with a low power seed [Fre07a].

During the first stage of this development phase an injection-locked two head laser system with a single-frequency output power of 87 W was presented [Fre04]. In the following experiments, the power was scaled by doubling the number of laser crystals resulting in the first prototype of a four head ring laser setup. With this laser an output power of 213 W with a fundamental mode beam profile, but without injection-locking, was achieved in a table-top laboratory experiment [Fre05c].

Similar to the two head laser, the four head ring laser was injection-locked following the Pound-Drever-Hall scheme. By comparison to the two head experiments the low output power of several hundred mW of the NPRO was not sufficient to es-

tablish a stable injection lock for the high power slave laser. As shown in Fig. 2.4, an intermediate stage was introduced into the setup. This stage is an exact copy of the GEO600 slave oscillator, which is injection-locked to the low power NPRO by a second set of Pound-Drever-Hall locking equipment. The single-frequency output beam with a power of approximately 10 W was then coupled into the high power slave oscillator. With this multi-staged laser an output power of 196 W in single-frequency operation was demonstrated [Fre05b]. Furthermore, the laser system passed the *Conceptual Design Review* [Fre05a], which was the first evaluation phase to verify the laser concept's suitability for use in Advanced LIGO.
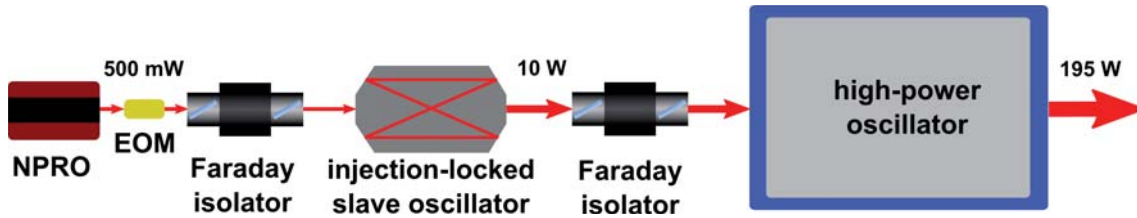

Figure 2.4: Schematic of the laboratory setup developed by Frede for the first demonstration of the feasibility as a laser for the next generation of GWD.

2.3   Laser concept

The final development process of the Advanced LIGO laser system, which will be described in this thesis, started immediately after the successfully passed conceptual design review phase. In this phase, the use of a multi-staged injection-locked setup incorporating a four head high power oscillator stage was defined. Even though the performance level of the first experimental laboratory setup was able to supply the required output power, the final Advanced LIGO requirements on higher-order mode content, frequency and power stability as well as long term stable operation could not be demonstrated. Thus the development of the Advanced LIGO laser concentrated on the optimization of the following laser output parameters to fulfill the requirements for the GWD's light source (see Table 2.1):

- Low power levels in residual higher-order modes, consequently optimization for highest power in TEM_{00} mode, which requires a laser resonator or spatial filter to control the higher-order mode content.

- Acceptable frequency and power noise levels, which can be controlled to the required range with an active stabilization scheme in a second development step (performed at the Max-Planck Institute for Gravitations Physics in Hannover).

- Long term stability in injection-locked operation and minimization of output power drifts due to environmental impacts.

These optical design goals were then taken and incorporated with the mechanical requirements, as they are:

- Optical packaging and positioning of all laser components to support a flexible laser resonator design and a compact high power oscillator system.

- Reduction of mechanical and thermal distortions on the laser's output performance.

- Modular structure for ease of maintenance.

- Rigid mechanical structure to survive transportation to the LIGO sites.

- Fully integrated cooling schemes incorporating design of water circuits and choice of appropriate materials.

As a result, a completely reengineered mechanical design of the laser system and especially of the high power oscillator for Advanced LIGO was developed. In Fig. 2.5 a block diagram of the high power oscillator development process, which was carried out during the herewith presented work, is given.

In contrast to the conceptual design prototype laser the actual system does not rely on a double injection locked scheme any more. The GEO600 10 W laser, which was used as an intermediate stage for the injection locking of the high power oscillator was replaced by a 35 W Nd:YVO$_4$ MOPA system. Still an NPRO, in this case a commercial Mephisto 2 W laser produced by the InnoLight GmbH, is the frequency reference for the complete laser system. By passing the NPRO's beam in a single pass through four end-pumped Nd:YVO$_4$ crystals an output power of 35 W is obtained [Fre07b]. As mentioned in the previous section, this MOPA system (developed by LZH and optimized by the spin-off company neoLASE GmbH) is already used as the light source for the intermediate upgrade of the LIGO detector, called *Enhanced LIGO*.

In Fig. 2.6 a schematic of the complete laser system is shown. The primary component of the laser for Advanced LIGO is the high power oscillator. To achieve high output power levels of more than 200 W, four laser crystals are arranged in a ring laser configuration. Each laser crystal is longitudinally pumped by seven fiber coupled laser diodes, which can provide a maximum pump-power of 315 W per laser rod. The combined pump spectrum of these diodes has a center wavelength of 808 nm and a full-width-half-max (FWHM) of 2.5 nm. During the development process of the
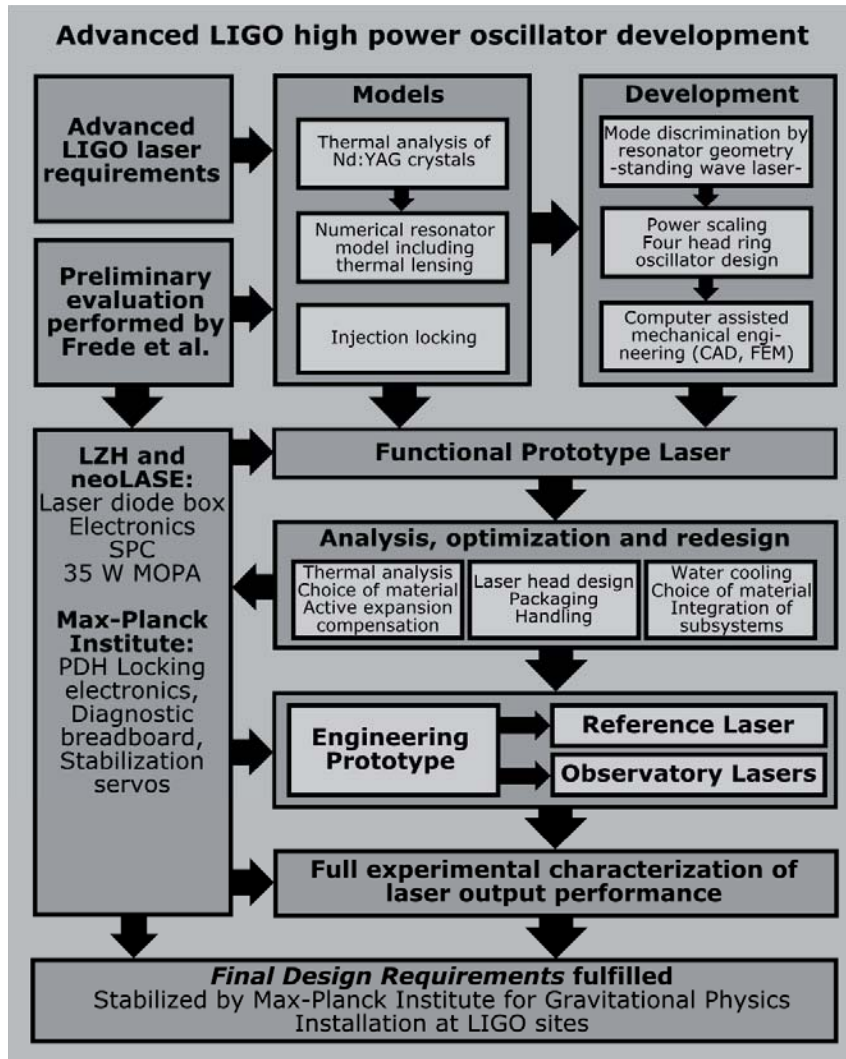
Figure 2.5: Block diagram of the high power oscillator development process.

high power oscillator setup in this work, an asymmetric cavity design turned out to be the best solution to achieve a maximum higher-order mode discrimination. With this laser resonator setup the TEM_{00} mode content was enhanced to the required level. For single-frequency operation, the high power oscillator is injection-locked to the 35 W MOPA system. To keep the frequency of the high power oscillator in resonance with the single-frequency seed a piezo actuated mirror was included into the asymmetric cavity. This mirror is connected to a Pound-Drever-Hall injection-locking servo which constantly adjusts the length of the high power slave resonator to match the frequency of the master laser.

To control the laser and all electrical components (power supplies, shutters, photo-diodes etc.), a software based stored program control (SPC) was used. With this system, a communication between the high power laser and the laser diode room

(LDR), which is located outside of the interferometer core building, is set up. The pump light and all data connections are transferred via optical fibers to the laser area enclosure (LAE). The separation of electronic laser hardware from the optical setup was necessary to shield the sensitive measurement equipment inside the LAE against electromagnetic interference generated by the used high power switching power supplies.
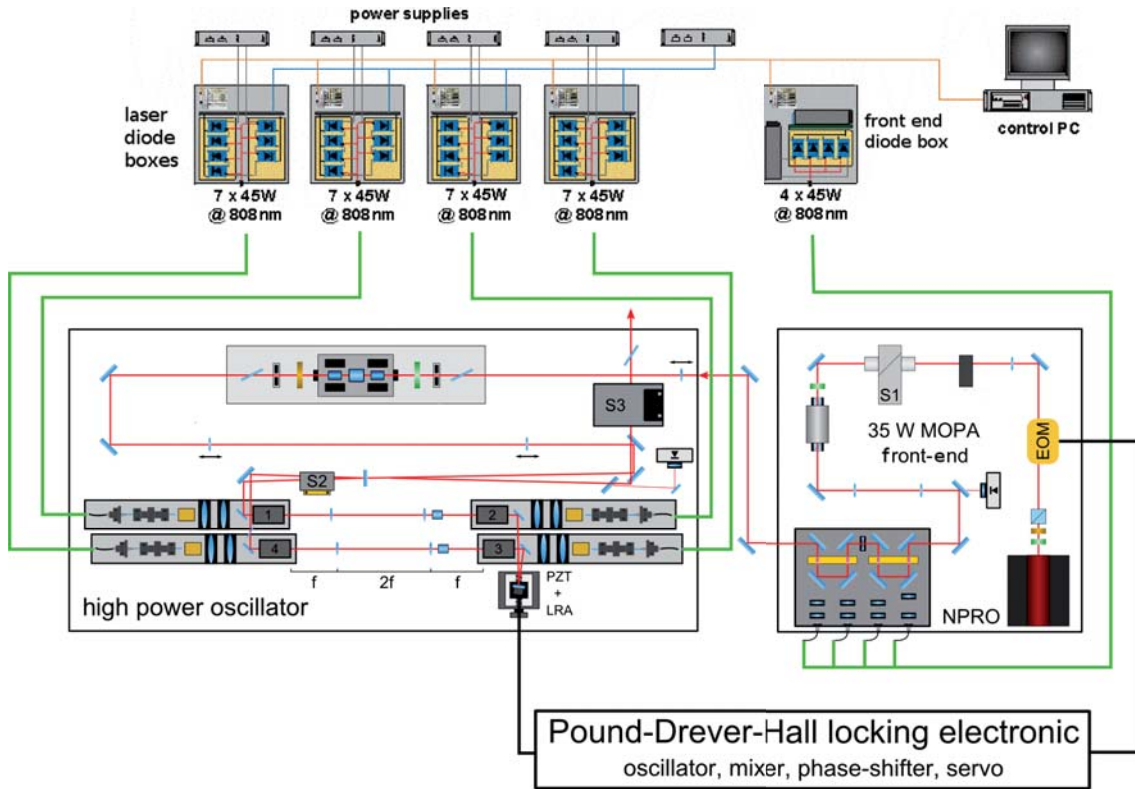

Figure 2.6: Schematic layout of the developed high power laser system. For more details of the individual components of the system see Chapter 4.

As described in Chapter 4, a constant operation of the full laser system at changing environmental conditions required the implementation of a water cooling scheme for the mechanical structure. Additionally, thermally induced fluctuations of the resonator length were compensated by a slow actuator, which also counteracts the pressure and humidity related optical path length changes of the surrounding air. Furthermore, the form factor of the complete high power oscillator was reduced. For this, all mechanical internal components were grouped in subsets and arranged in a manner to minimize the form factor of the rigid base-plate, whilst keeping optical distances unchanged. When being operated, dust on the laser optics is the main source for damage and hence malfunction of the injection-locked laser. To reduce the hazard of dust related damage, a dust sealed laser housing was designed.

Furthermore, the whole laser was assembled and tested in a clean room environment (applying to ISO6 standard). To ensure the same quality standards for all three laser systems, incoming inspections for the optical and mechanical parts were performed and test reports were stored for each component.

With this laser system it was possible to fulfill the free-running *Final Design Requirements* given in Table 2.1 for a laser system for the next generation gravitational wave detector Advanced LIGO [Kim10]. In fact, the first laser system installation began in March 2011 in the LIGO detector located at Livingston, Louisiana and was completed in June 2011.

Chapter 3

Models for system development

In this chapter the models needed for the development of the laser system for Advanced LIGO are discussed. As part of this chapter, a description of thermal effects in end-pumped laser crystals and their influence on resonator stability will be given in Section 3.1. Furthermore, higher-order modes and their mitigation by choice of resonator design will be presented in Section 3.2 and 3.3.

Within Section 3.4, the fundamentals that describe the coupling of a high power oscillator to a low power seed laser via injection locking are discussed. The derived basics are then used in an electronic feedback control, which is applied to the laser system presented in this work.

3.1 Thermo-optical effects in end-pumped Nd:YAG crystals

Optical pumping of solid-state laser active media always results in heat generated inside the crystal lattice. The fraction of the incident pump energy or power which is transferred into heat can be defined by the fractional thermal loading coefficient η_h, which depends on the spectrum of the incident pump light and the material properties of the used laser gain media. For Nd:YAG solid-state lasers pumped with a small spectral bandwidth light source the fractional thermal loading coefficient varies from 25% to 40% depending on the concentration of the dopant and the purity of the crystal material [Fan93]. The heat inside the laser active media primarily arises because of the following effects:

- The Stokes or quantum defect of the incident pump light to the emitted laser light, which is the nonradiative relaxation of electrons from the pump to the upper metastable level and from the lower laser level to the ground state of the Nd:YAG material, and

- the nonradiative sites and cross relaxations from the pump to the ground level.

In general, the quantum defect, which is defined as the energy fraction between pump and laser photon, is the largest contribution to the heat generated inside the Nd:YAG crystal. Given that the pump light source emits at a center wavelength of 808 nm and the laser emission wavelength is at 1064 nm, 24% of the incident pump power is transferred into heat. The fraction of heat introduced into the laser crystal by emission-free relaxations mainly depends on the material properties of the Nd:YAG media. The higher the doping concentration of the laser crystal with the active ion (Nd^{3+}), the higher the fraction of pump light energy transferred into heat [Bro98b].

In contrast to side pumped lasers, diode end-pumped schemes offer a higher efficiency due to the better spatial overlap of the pump light distribution and the laser mode. As a consequence of the longitudinal injection of the pump light through the end-facet of the laser crystal, a non-uniform temperature distribution arises inside the crystal. Consequently, the axial heat distribution changes the refractive index of the material leading to a thermal lens profile. In addition to that, stress is induced by this temperature gradient in the rod structure, which leads to birefringence of the Nd:YAG material.

3.1.1   Analytical treatment

For a treatment of the thermal effects inside an end-pumped Nd:YAG crystal, a laser rod with a symmetric geometry along its optical axis is assumed. In that case, the stationary heat flow can be described by the equation:

$$\frac{1}{r}\frac{\partial}{\partial r}\left[r\frac{\partial T(r,z)}{\partial r}\right] + \frac{Q(r,z)}{K(T)} = 0, \tag{3.1}$$

where $K(T)$ is the temperature dependent thermal conductivity of the laser rod, and $Q(r,z)$ represents the thermal power density, i.e. the spatial heat load distribution generated by the incident pump light depending on the radial position r and the axial position z. In an end-pumped laser geometry the heat load generated by pumping the active media with a fiber coupled source can be approximated by a circular Gaussian spatial function with a beam waist of $\omega_p(z)$ [Wil09]

$$Q(r,z) = \frac{2\eta_h P_{in}}{\pi\omega_p(z)^2\left[1 - \exp(-2R^2/\omega_p(z)^2)\right]}\cdot\alpha_{\text{eff}}(z)\cdot\exp\left[-\frac{2r^2}{\omega_p(z)^2}\right]\exp\left[-\int_0^z \alpha_{\text{eff}}(z)dz\right], \tag{3.2}$$

where P_{in} is the incident pump power, R the crystal radius and $\alpha_{\text{eff}}(z)$ the effective absorption coefficient. This coefficient has to be introduced to solve the Lambert-Beer's law for pump light with a spectrally broad distribution instead of just one discrete wavelength. In Fig. 3.1a, the calculated impact of the effective absorption coefficient on a spectral pump light distribution with a Gaussian shape, a full-width-half-max (FWHM) of 2.5 nm and a center wavelength of 808 nm is shown at different positions inside a 0.1 at.%[1] doped Nd:YAG crystal. It can be seen that single spectral components of this pump light distribution are unequally absorbed by the active media corresponding to the absorption spectrum of the Nd:YAG material. The effective absorption coefficient can be derived by

$$\alpha_{\text{eff}}(z) = \frac{\int_0^\infty \alpha(\lambda)p(\lambda,z)d\lambda}{\int_0^\infty p(\lambda,z)d\lambda} = \frac{1}{P_{in}} \int_0^\infty \alpha(\lambda)p(\lambda,z)d\lambda, \tag{3.3}$$

where $\alpha(\lambda)$ is the wavelength dependent absorption coefficient of Nd:YAG, $p(\lambda,z)$ is the spectral power distribution of the pump light at the position z and P_{in} is the integrated total incident pump power. The pump power at a given position z inside the laser crystal can be estimated for a laser active medium by an absorption coefficient for the center wavelength of the pump light and an effective one. The resulting residual pump power for a given propagation length inside the crystal is shown in Fig. 3.1b. As the total absorbed pump power has the largest influence on the thermal distribution inside the crystal the effective absorption model was used for the following calculations.
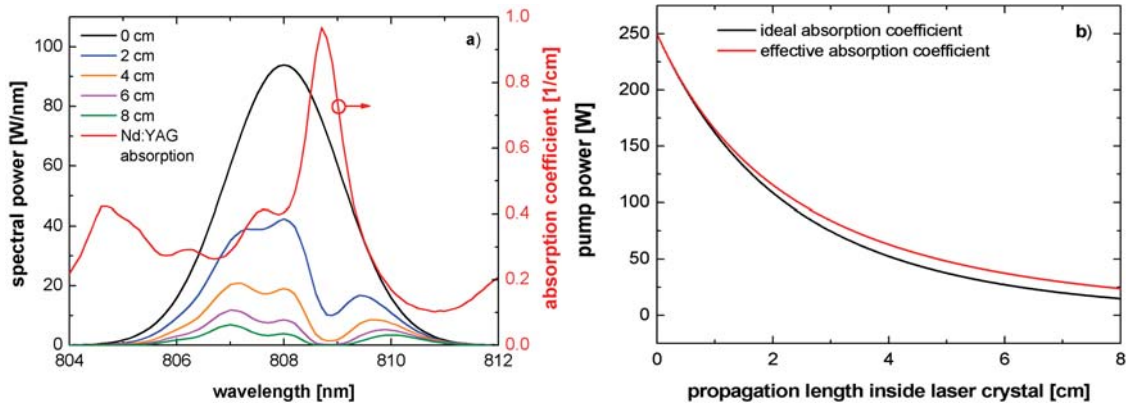

Figure 3.1: In a) the absorption spectrum of a 0.1 at.% doped Nd:YAG crystal is given (red curve). Furthermore, the corresponding spectrum of the incident pump light after different propagation lengths through the crystal is shown. In graph b) the calculated residual pump power with and without taking the effective absorption coefficient into account is shown.

---

[1]The **atomic percent** or at.% defines the percentage of one kind of atoms relative to the total number of atoms in a substance.

The variation of the pump spot radius along the z-axis of the active media can be described by

$$\omega_p^2(z) = \omega_{p0}^2 \left[1 + \left(\frac{M^2 \lambda_p z}{\pi n_0 \omega_{p0}^2}\right)^2\right], \tag{3.4}$$

where n_0 is the refractive index of the Nd:YAG crystal material, ω_{p0} is the beam waist of the pump laser or so called *pump spot*, and λ_p is the center wavelength of the pump light source with beam quality factor M^2.

For a laser crystal rod, which is cooled at the outer surface, the Newtonian boundary conditions define the temperature values $T|_0$ at the surface of the laser crystal

$$K(T) \frac{dT}{d\vec{n}}\bigg|_0 = \lambda_k(T_k - T|_0), \tag{3.5}$$

where $\vec{n}$ is the surface normal vector on the cylindrical surface of the laser crystal, λ_k is the heat transfer coefficient for the corresponding Nd:YAG and cooling material with its temperature T_k. For a laser crystal rod, which is directly cooled by water, the heat transfer coefficient is calculated depending on the type of fluid flow – laminar or turbulent. In a high power laser system, a turbulent flow of water around the laser crystal rod is mandatory, because it significantly increases the heat transfer coefficient. Given that the fluid flow is turbulent, the heat transfer coefficient can be estimated by [Hsü63]

$$\lambda_k(l) = 0.02 \frac{K_w}{D_2(l) - D_1} \left(\frac{D_2(l)}{D_1}\right)^{0.53} N_{Re}(l)^{0.8} N_{Pr}(l), \tag{3.6}$$

where D_1 is the rod diameter and $D_2(l)$ is the variable diameter of the flow tube surrounding the crystal at a position l. $N_{Re}(l) = [\rho u(D_2(l) - D_1)]/\mu$ and $N_{Pr}(l) = C_w \mu / K_w$ are the corresponding Reynolds and Prandtl numbers depending on $D_2(l)$, the mass density ρ, the fluid velocity u, viscosity μ, specific heat C_w and the thermal conductivity K_w of the coolant. A good overview and table of needed constants to calculate $\lambda_k(l)$ is given by Kim et al. [Kim91]. It is worth mentioning that the surfaces of all components in contact with the cooling liquid are assumed to be macroscopically smooth.

3.1.2 Numerical treatment

Various approaches have been carried out to solve the heat conduction equation for the specific case of laser induced heating of a solid-state crystal rod. The most

common approach is to find an analytic solution by simplification of the boundary and initial conditions for the given problem. Solutions for different laser configurations can be found in Refs. [Koe70, Far88] for side-pumped lasers and in Refs. [Inn90, Cou92, Tid92, Cla01, Pen04, Wil08] for end-pumped laser designs.

In most cases a straight-forward solution of the heat equation inside a laser rod is desired. For this purpose numerical calculation models have been written. In the literature, a solution for the differential equation defining the conduction of heat in solids can be approximated by various different methods. With the *finite difference method* (FDM) a solution for the differential heat equation by replacing derivative expressions with approximately equivalent difference quotients is obtained [Tsu97, YJ06]. For the *boundary element method* (BEM) the linear partial differential equations are transformed into integral equations of the boundary integral form. Using computer algorithms to solve these integrals, one can find a solution for the temperature distribution of a pumped solid-state laser crystal [Sov07]. The most common computational method to solve the differential heat flow equation is the *finite element method* (FEM) [Pen01, Web98, Kra05, Wil09]. For this method the mesh of the finite solid is split up in discrete areas. For these so called nodes the partial differential equation is either eliminated (steady-state) or it is rendered into an approximating system of ordinary differential equations that can be solved with an integral approximation. By contrast to the FDM and BEM methods, commercial software products that perform an FEM analysis are broadly available. Another method utilizes a numerical *Fourier-Bessel* approach to solve the stationary heat equation in a cylindrically symmetric geometry. This approach eliminates the need for extensive computational calculations, while taking axial heat transport and the temperature dependent material properties into account. A software package called *Rod Designer* implementing this approach was developed by Wilhelm et al. [Wil09]. A more detailed description of this software can be found in Appendix B.

For an initial detailed approximation of the temperature distribution inside the laser crystals, the FEM software ANSYS was used. The obtained results were then compared with data generated with Rod Designer to verify their consistency.
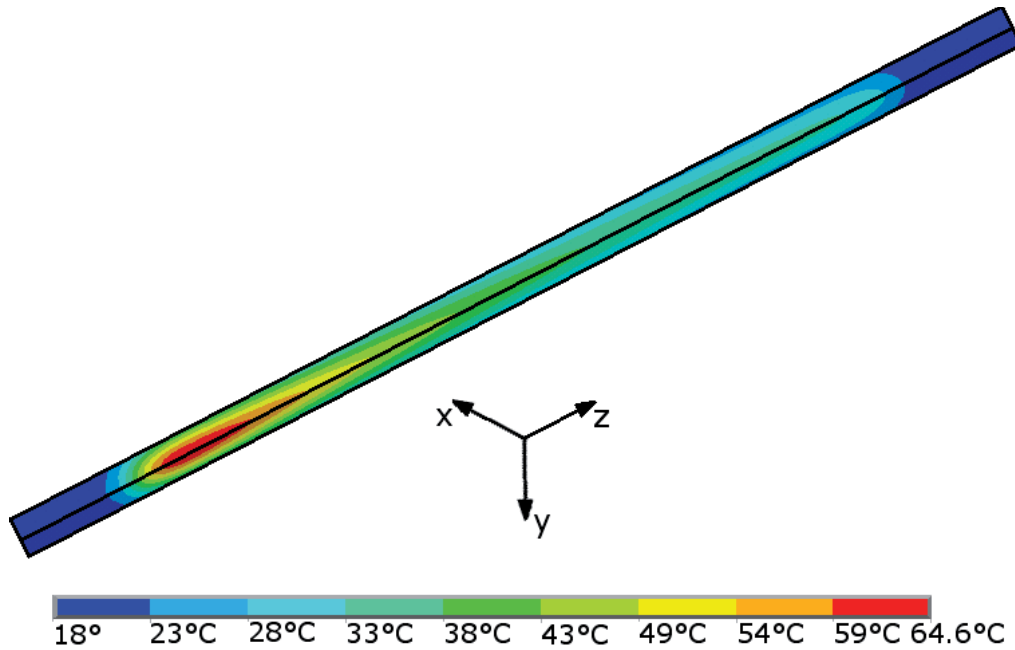
Figure 3.2: Temperature distribution obtained after steady-state thermal analysis with ANSYS.

For a simplification of the model, the cylindrically symmetric rod structure was reduced to a quarter of the rod's aperture. The length and the material structure was then modeled within the preprocessor of the FEM software. At points of interest, e.g. at the pump spot position or boundaries of doped and undoped YAG material, the number of longitudinal nodes was doubled to increase the accuracy in this region (2 nodes per mm). The material properties for Nd:YAG given in the Appendix A are applied to the solid model of the laser crystal for the simulation. With Eq. (3.2) the heat generated in the doped region of the laser crystal by absorption can be calculated for each element of the rod structure. The data is then fed into the simulation as an array of data points, corresponding to the position of each node inside the laser rod model. Actually, the calculation of the pump light induced heating can also be performed for pump light distributions determined by a ray tracing analysis of the complete optical system.

The outer wall of the laser crystal is usually in contact with a cooling liquid, in this case deionized water. As described above, the heat transfer from the rod structure to the coolant strongly depends on the mass flow and the velocity of the liquid. With Eq. (3.6) the needed heat transfer coefficient for the Newtonian boundary condition can be calculated for arbitrary flow rates and geometries. This coefficient is inserted either as a distribution or a constant along the length of the laser crystal, to account for the heat flow by convection into the cooling liquid. A detailed description

of the cooling chamber's geometry surrounding the laser crystal can be found in Section 4.2.7.

After all, the parametrized model is solved in a steady-state analysis. The resulting axial temperature distribution for a laser rod with 0.1 at.% Nd^{3+} doping concentration, two 7 mm long undoped end-caps and an overall length of 54 mm is shown in Fig. 3.2. An incident pump power of 250 W at a center wavelength of 808 nm with a FWHM of 2.5 nm was used during the calculation.

In a following step, the determined thermal loads for the FEM model can be processed in a nodal stress and strain analysis of the model. Afterwards, the resulting stress data is combined with the temperature distribution for the calculation of the crystal's internal thermal lens. In general, the refractive index of a solid depends on three different effects: the localized heating of the material, the expansion due to heat and the stress induced birefringence. The resulting *optical path length difference* (OPD) for a pumped laser crystal of length l and radius r_0 can be derived from the numerical temperature distribution $T(r, z)$:

$$OPD(r) = \int_0^l T(r, z) \left[\frac{dn}{dT}(T) + n_0^3 \cdot \alpha(T) \cdot C_{r,t} + \frac{\alpha(T) \cdot r_0 \cdot (n_0 - 1)}{l} \right] dz, \quad (3.7)$$

where $n_0 = 1.82$ is the refractive index of Nd:YAG and $\frac{dn}{dT}(T)$ is the temperature dependent refractive index variation of Nd:YAG. $\alpha(T)$ is the linear thermal expansion coefficient and $C_{r,t}$ are constants for the tangential and radial stress components. A detailed description of the determination of all these temperature dependent material constants can be found in Ref. [Bro98a]. A comprehensive overview of all necessary functions and constants to determine the OPD for the simulated temperature, stress and strain data is given in the Appendix C.

In Fig. 3.3a the resulting temperature distribution of the previously simulated laser crystal rod is presented in an color plot of the x-z-plane. As mentioned above, the laser crystal has two undoped end-caps with a length of 7 mm each. Thus, the highest temperature arises approximately 10 mm inside the laser crystal. This position shows a good overlap with the pump spot position used for the simulation (see Section 4.2.5 for a diagram of the pump light distribution inside the crystal). In fact, the undoped end-cap has three positive effects. When optically pumped through the facet, the end surface of a laser crystal without end-caps would bulge under the thermal load. This bulging, which is caused by the temperature dependent thermal expansion of the Nd:YAG material, would lead to a convex-shaped surface at the ends of the crystal rod and a high tensile strain at those positions. With the diffusion bonded end-caps, the interface of doped and undoped media is shifted to the inside of the bulk

material. As the point of the highest load is located at this interface, the formation of tensile strain at the lattice is converted in compressive strain, which eliminates the bulging effect. Furthermore, the risk of a failure due to a high tensile load is avoided, which increases the fracture limit of such a laser crystal and consequently the applicable pump power. Last but not least, the undoped end cap improves the life time of the applied coatings, as their quality would degrade because of the high thermal load at the doped material interface.
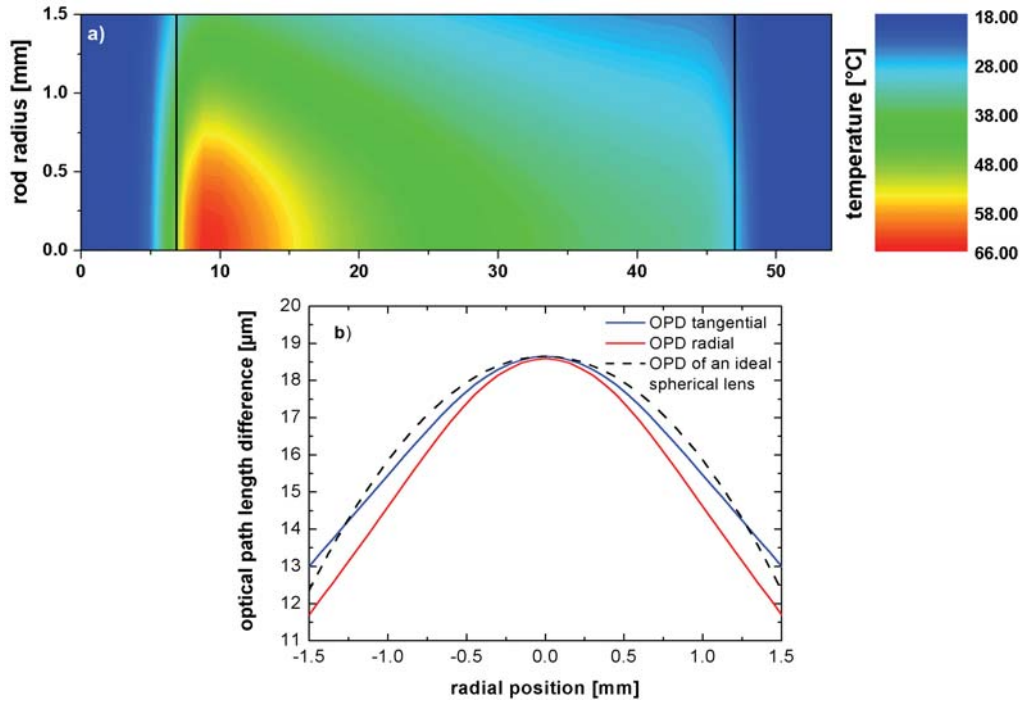
Figure 3.3: a) Temperature distribution in the x-z-plane. Black lines indicate the undoped to doped crystal material interconnection. b) Resulting optical path length difference in respect to the rod radius. For comparison, the OPD for an ideal spherical lens is given (dashed black line).

With Eq. (3.7) the data generated by the FEM analysis can be interpolated over the x-z-plane. After integration of the resulting optical path length differences for each element of the crystal model, an overall OPD in z-direction was obtained. Neglecting the temperature dependence of $K(T)$ an ideal thermal lens, which is only generated within a homogeneously pumped laser crystal, would form a parabolic OPD profile (black dashed line in Fig. 3.3). For an end-pumped laser crystal rod, the shape of the OPD distribution deviates from a parabola with increasing distance from the center of the rod as displayed in red and blue for tangential and radial polarized light in Fig. 3.3b. As a consequence, the resulting thermal lens has an aspherical shape.

Even though the aspheric form of the thermal lens causes beam distortions for beams with a large cross-section, the effect of a varying focal length depending on the beam diameter can be utilized in the resonator design. A detailed description of the effect of higher-order mode discrimination by resonator design, which involves the aspherical shape of the thermal lens, is given briefly in Section 3.3 and in greater detail in Chapter 4.

Several other effects, which have an impact on the performance of an end-pumped solid-state laser system, can be analyzed performing the same numerical FEM analysis. The ones which influence the performance the most, are the thermally induced birefringence of Nd:YAG and the associated depolarization of the laser beam, and fracturing of the laser rod itself due to thermal stress above the failure threshold. As part of the preliminary experiments performed by Frede et al. the laser crystal design was chosen, to withstand high pump power levels without mechanical failure. A detailed evaluation process for the determination of this design can be found in Ref. [Fre07a].

The effect of thermally induced birefringence in Nd:YAG laser crystal rods is widely discussed in literature [Tid92, Lü95a, Sch98, Fre07a]. Usually, for a laser system uncompensated for resonator internal depolarization, which is caused by this birefringence, the output power in the linearly polarized fundamental mode is limited to 40 W [Mur96]. This limitation can be eliminated using an optical depolarization scheme inside the laser resonator. A setup of such an optical system, which is now a standard technique in multi-rod laser resonators, is described in Section 4.1.1 in more detail. A good overview of other effects that can be derived from the results of the FEM temperature and stress analysis of the laser crystal can be found in Ref. [Sch98].

For further treatment it is necessary to calculate the refractive power or so called thermal lens with the aid of the optical path length data. Because of the deviation of the OPD's shape from a parabola, this has to be done for different beam sizes. For this purpose, a parabola with

$$OPD_{fit}(r) = A + C \cdot r^2 \tag{3.8}$$

is fitted to a chosen data range of the OPD profile, spanning from the center of the crystal to the desired beam radius r. The second derivative of the fit-function $OPD_{fit}(r)'' = 2C$ determines the refractive power of the corresponding thermal lens. As described in the following section, these values can be used for an analysis of the resonator stability for a given laser cavity.

To qualify the Rod Designer software for prediction of mechanical and optical parameters of end-pumped laser crystals, a comparison of OPDs obtained by FEM analysis and Rod Designer data was performed. In fact, the Rod Designer showed a deviation of the numerically calculated thermal lens of 2.5/0.85/2.2 % and 11.1/7.5/7.5 % for radially and tangentially polarized beams with radii of 0.5/1.0/1.5 mm, respectively. Examples of the comparison of the OPD for a pumped laser crystal determined with FEM analysis and the results obtained by inserting the same parameters into the Rod Designer are shown in Fig. 3.4.
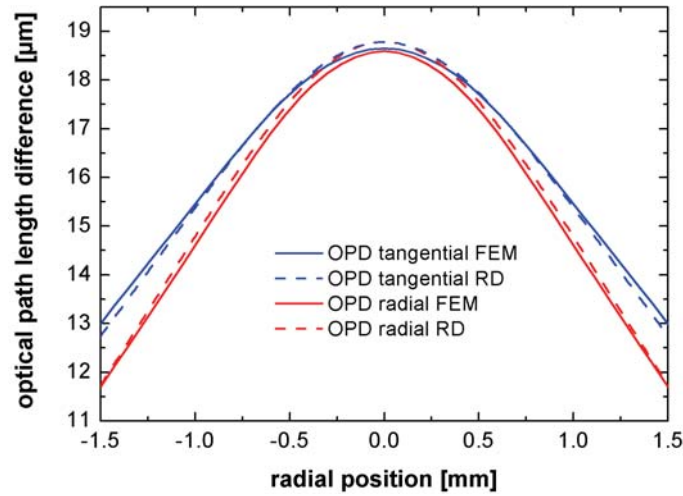
Figure 3.4: OPD obtained by a FEM simulation (solid lines) of an end-pumped laser crystal compared with the data determined with the Rod Designer program for identical system parameters (dashed lines).

In most cases the expected error for data obtained by a Rod Designer calculation stays within the standard deviation of known and inserted laser parameters, e.g. pump spot diameter, pump light distribution, doping concentration and gradient, and actual laser mode field diameter. In conclusion, it is a powerful, fast and easy to use tool for the prediction of thermal effects in end-pumped laser crystals. For a detailed analysis or evaluation of new laser crystal designs the FEM method is preferable because of its greater accuracy.

3.2   Gaussian beams and higher-order modes

In this section, an overview of the theory of Gaussian optics, based on the publication of Kogelnik [Kog66] and Magni [Mag91], will be given to the extent needed to describe dynamically stable laser resonators with an aspherical thermal lens.

3.2.1 Higher-order Gaussian modes

Even though laser beams are similar in many respects to plane waves, their intensity profile is not uniform, but concentrated near the axis of propagation z. Additionally, the phase front of these waves is slightly curved. To derive a formula that describes the propagation of a beam in a uniform media the Helmholtz wave equation is used

$$\left(\nabla^2 + k^2\right) u = 0, \tag{3.9}$$

where $k = 2\pi/\lambda$ is the propagation constant in the medium and $u(x, y, z)$ is an electromagnetic field component or potential of the coherent light. For light traveling in z-direction a functional form

$$u(x, y, z) = \psi(x, y, z) \exp(-ikz), \tag{3.10}$$

can be defined, where the non-plane-wave behavior is described by ψ. Inserting this into Eq. (3.9) the reduced wave equation of the form

$$\frac{\partial^2 \psi}{\partial x^2} + \frac{\partial^2 \psi}{\partial y^2} + \frac{\partial^2 \psi}{\partial z^2} - 2ik\frac{\partial \psi}{\partial z} = 0, \tag{3.11}$$

is obtained. As the variation of ψ is slow along the z-axis compared to the one in x and y direction, the third term can be dropped by applying the *slowly varying envelope approximation*. This leads to the symmetric paraxial wave equation in cylindrical coordinates with $r^2 = x^2 + y^2$

$$\frac{\partial^2 \psi}{\partial r^2} + \frac{1}{r}\frac{\partial \psi}{\partial r} - 2ik\frac{\partial \psi}{\partial z} = 0. \tag{3.12}$$

For this equation a solution of the following form can be found

$$\psi(r, z) = \exp\left\{-i\left[P(z) + \frac{k}{2q(z)}r^2\right]\right\}. \tag{3.13}$$

The parameter $P(z)$ represents a complex phase shift associated with the propagation of the corresponding beam. $q(z)$ is the complex beam parameter which defines the intensity variation of the beam at a distance r from the optical axis, as well as the curvature of the phase front $R(z)$.

Both parameters have to fulfill the following conditions

$$
\begin{aligned}
\frac{1}{q(z)} &= \frac{1}{R(z)} - i\frac{\lambda}{\pi\omega^2(z)} \Rightarrow \frac{\partial P}{\partial z} = -\frac{i}{q(z)}, \\
\frac{\partial q(z)}{\partial z} &= 1 \Rightarrow q(z) = q_0 + z,
\end{aligned}
\tag{3.14}
$$

where

$$
\omega = \omega_0 \sqrt{1 + \left(\frac{z}{z_c}\right)^2},
\tag{3.15}
$$

$$
R = z\left(1 + \left(\frac{z_c}{z}\right)^2\right),
\tag{3.16}
$$

and

$$
z_c = \frac{\pi\omega_0^2}{\lambda}.
\tag{3.17}
$$

ω is defined as the beam radius where the amplitude of the electric field profile has reached a level of $1/e^2$ of its maximum value on the z-axis. The parameter ω_0 is the minimum beam radius or beam waist. R can be identified as the radius of curvature of the phase front where it intersects the z-axis and z_c is the confocal distance where the radius of curvature of the beam has a minimum.

Integrating $\frac{\partial P}{\partial z}$ one can see that the real part of P represents a phase shift difference $\Phi(z)$ between the Gaussian beam and an ideal plane wave (*Gouy phase*), while the imaginary part gives the expected intensity decrease as an amplitude factor $\omega_0/\omega(z)$. With these results for a fundamental Gaussian beam, Eq.(3.10) can be rewritten as

$$
u(r,z) = \frac{\omega_0}{\omega(z)} \cdot \exp\left[-\frac{r^2}{\omega(z)^2}\right] \exp\left\{-i\left[\frac{k}{2R(z)} + kz - \Phi(z)\right]\right\},
\tag{3.18}
$$

where

$$
\Phi(z) = \arctan\left(\frac{z}{z_c}\right).
\tag{3.19}
$$

This is only one possible solution of Eq. (3.11) that describes a light beam with an intensity profile given by the same function in every beam cross-section, namely, a Gaussian. In fact, other solutions for Eq. (3.11) can be found that form a complete and orthogonal set of functions, which are called the *modes of propagation* or *higher-order modes*. These modes of a beam can be either described in Cartesian coordinates, for optical systems with square apertures and optics, or in cylindrical coordinates.

For an optical system with cylindrical geometry one can expand Eq. (3.13) to the form

$$\psi(r,z) = g\left[\frac{r}{\omega(z)}\right] \cdot \exp\left\{-i\left[P(z) + \frac{k}{2q(z)}r^2 + l\Phi(z)\right]\right\}. \tag{3.20}$$

After some calculations one finds a solution for g with

$$g = \left(\sqrt{2}\frac{r}{\omega}\right)^l \cdot L_p^l\left(2\frac{r^2}{\omega^2}\right) \tag{3.21}$$

where L_p^l is a generalized Laguerre polynomial, and p and l are the radial and angular mode numbers. To classify different higher-order transverse electromagnetic modes, the abbreviation TEM_{pl} with the corresponding mode numbers p and l as indices is introduced. Some examples of polynomials of lower order are

$$
\begin{aligned}
L_0^l(x) &= 1 \\
L_1^l(x) &= l + 1 - x \\
L_2^l(x) &= \frac{1}{2}(l+1)(l+2) - (l+2)x + \frac{1}{2}x^2.
\end{aligned}
\tag{3.22}
$$

The parameter $R(z)$ in Eq.(3.18) is the same for all modes, which implies that the phase-front curvature for all Gaussian modes is the same and changes in the same way for all higher-order modes. However, the phase shift of the corresponding modes is dependent on the mode order, which means that the phase velocity increases with decreasing mode number. The *Gouy phase* of a Gaussian Laguerre mode is then given by

$$\Phi_{pl}(z) = (2p + l + 1) \cdot \arctan\left(\frac{z}{z_c}\right). \tag{3.23}$$

Furthermore, the diameter of a beam with a higher-order mode intensity distribution differs from the one for a fundamental Gaussian distribution. A simple relation between the fundamental mode radius and the estimated beam radius of the corresponding higher-order mode is given by

$$\omega_{pl}(z) = \sqrt{2p + l + 1} \cdot \omega(z). \tag{3.24}$$

Because of the rather complicated beam pattern of higher-order modes it is not possible to define the beam size of such a mode by a $1/e^2$ drop in amplitude as for a TEM_{00} mode. To obtain a relationship of beam diameter and divergence of such a cylindrical higher-order mode its diameter is defined as a circle containing 90 % of the energy.

3.2.2 Matrix formalism

As presented in Fig. 3.5 rays of light traveling through optical systems are characterized by their distance d and their angle ϕ to the optical axis.
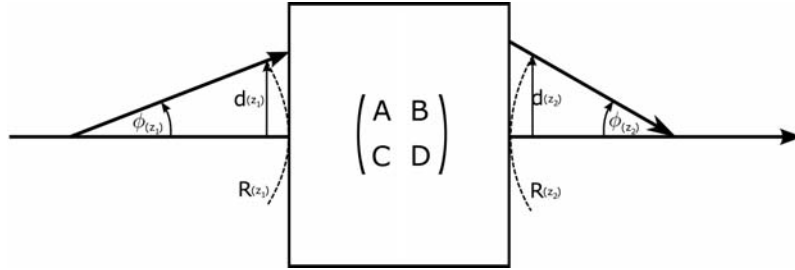

Figure 3.5: Propagation of ordinary spherical waves through an arbitrary optical system.

For rays with a small divergence angle ϕ, a paraxial approximation can be performed where $\sin(\phi) \approx \phi$. Now d and ϕ are linearly coupled and their transformation during propagation through an optical system is described by a matrix multiplication of the form:

$$\begin{pmatrix} d(z_2) \\ \phi(z_2) \end{pmatrix} = \begin{pmatrix} A & B \\ C & D \end{pmatrix} \begin{pmatrix} d(z_1) \\ \phi(z_1) \end{pmatrix} \tag{3.25}$$

The matrix elements A, B, C and D are real numbers. The determinant of the ABCD ray matrix $AD - BC = 1$, as long as the incoming and outgoing beams are propagating in the same medium. An overview of standard ray matrices for optical systems is given in Table 3.1. The corresponding ABCD matrix for an optical system

Beam propagation along distance L:	$\begin{pmatrix} 1 & L \\ 0 & 1 \end{pmatrix}$
Transit from medium n_1 to n_2:	$\begin{pmatrix} 1 & 0 \\ 0 & \frac{n_1}{n_2} \end{pmatrix}$
Thin lens with focal length f:	$\begin{pmatrix} 1 & 0 \\ -\frac{1}{f} & 1 \end{pmatrix}$

Table 3.1: Table of common matrices for optical elements

can then be calculated by multiplication of the fundamental matrices given above. From Kogelnik [Kog65] it can be seen that rays associated with a spherical wave are

perpendicular to the plane of the corresponding wavefront. The radius $R(z)$ of this wavefront depends on the slope $\phi(z)$ and position $d(z)$ of the paraxial ray, with

$$R(z) = \frac{d(z)}{\phi(z)}. \tag{3.26}$$

For a given optical element defined by an ABCD matrix the transformation of the wavefront for a passing paraxial ray can be determined from

$$R(z_2) = \frac{AR(z_1) + B}{CR(z_1) + D}. \tag{3.27}$$

If this formalism is extended to Gaussian-like spherical waves using the complex beam parameter $q(z)$, the following formula for the propagation through an optical element or system can be derived [Kog66]

$$q(z_2) = \frac{Aq(z_1) + B}{Cq(z_1) + D}. \tag{3.28}$$

In ideal laser resonators with spherical mirrors of infinite size and an active medium with homogeneous gain, the solution for the fundamental mode can be approximated as a Gaussian intensity distribution. This assumption is also valid for real resonators with spatially limited optics. Thus, the beam path for a given cavity can be calculated as a set of matrices for the resonator internal optical elements.
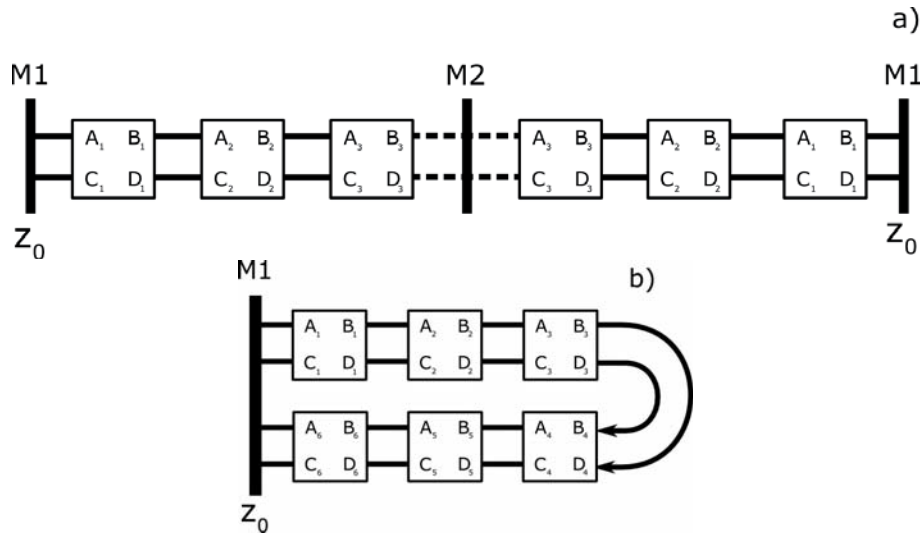

Figure 3.6: Periodic matrix sequence for **a)** a standing wave resonator and **b)** a ring resonator setup.

For this purpose a sequence of matrices corresponding to the optical elements, which are passed in a full round trip through the optical resonator, is multiplied. This can be done for any start or end position z_0 inside the resonator. For a standing wave cavity, in which the beam bounces back and forth, the sequence of matrices represents the beam path, in which the beam passes through each optical element two times for a complete round trip (see Fig 3.6a). In a ring resonator, the position z_0 is reached again after a single pass through the optical elements. Hence the sequence for a ring resonator only contains the matrices for the internal optical components once, as shown in Fig. 3.6b. For stable oscillation of the fundamental mode inside the resonator the complex beam parameter $q(z)$ has to reproduce itself after one round trip. Assuming that $q(z_1) = q(z_2) = q(z_0)$ a quadratic equation can be derived from Eq. (3.28), which has a solution for q given by

$$\frac{1}{q} = \frac{D - A}{2B} - \frac{i}{2\,|B|}\sqrt{4 - (A + D)^2}, \tag{3.29}$$

where A, B, C and D are the matrix elements of the round trip cavity matrix derived by multiplication of the periodic sequence of matrices. With Eq. (3.15) and Eq. (3.17) the beam radius and the wave front curvature at the position z_0 can be expressed by

$$\omega^2(z_0) = \frac{\lambda\,|B|}{\pi}\sqrt{\left[1 - \left(\frac{A + D}{2}\right)^2\right]^{-1}}, \tag{3.30}$$

$$R(z_0) = \frac{2B}{D - A}. \tag{3.31}$$

As a criteria for the stability of a resonator setup the beam radius must be real and greater than zero at any position inside the resonator. From Eq. (3.29), a stability criterion can be derived, with

$$|A + D| < 2. \tag{3.32}$$

To distinguish between a stable and unstable resonator, it is sufficient to calculate the matrix for one round trip at any position, because it covers the full path through the optical system.

3.3 Dynamically stable resonators with an aspherical thermal lens

With the tool at hand to express a laser resonator as a combination of matrices for its internal optical elements, a prediction about the stability of real laser resonators was established in this work. For the numerical calculations the thermal lens positions inside the optical laser resonator are approximated by thin lenses at the plane of the highest heat load inside the laser crystal. As illustrated in Fig. 3.7a the OPD and hence the thermal lens of a laser crystal rod under optical end-pumping has a shape deviating from the ideal parabolic distribution. Consequently, the focal length of this lens does not only depend on the pump power, but also on the laser mode field diameter inside the laser crystal rod.
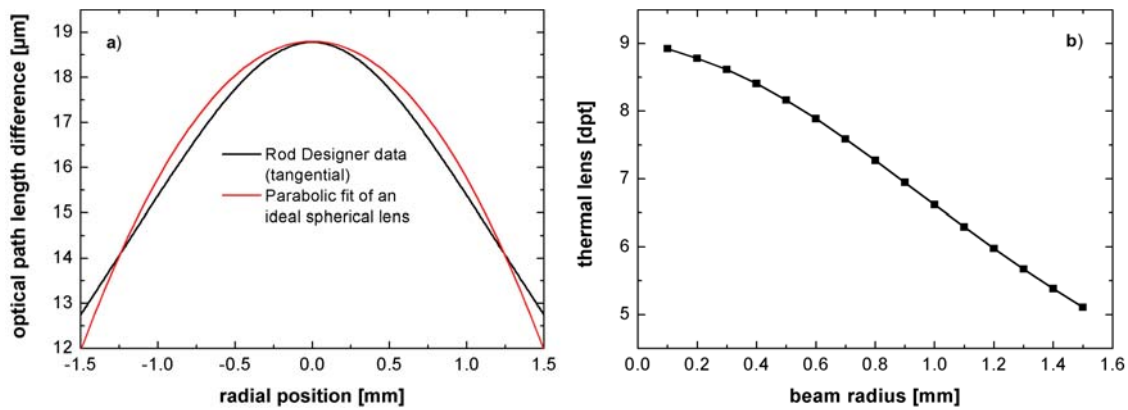
Figure 3.7: a) Resulting optical path length difference from the numerical simulation at an incident pump power of 250 W at a center wavelength of 808 nm with a FWHM of 2.5 nm. For reference, a parabolic OPD distribution of a spherical lens with the same peak value and minimum deviation from the simulated curve is drawn in red. b) Refractive power derived from fitting Eq. 3.8 for different beam radii.

In Fig. 3.7a, the optical path length difference at different radial positions of a laser crystal pumped with 250 W is shown. The data for this graph was calculated with *Rod Designer*, from which the results have sufficient accuracy compared with other numerical methods (see Section 3.1 and the Appendix B for more details). The effective thermal lens can then be approximated by a parabolic fit of the refractive index profile over the incident laser beam radius and also varies with beam size. In Fig. 3.7b, it is shown that the effective thermal lens decreases with increasing beam size.

To define the thermal lens for a range of pump power levels, a set of optical path length differences was calculated for a pump power range from 0–315 W. Afterwards a polynomial fit was performed at each pump power step for beam radii ranging from 0.1–1.5 mm. When combined, a thermal lens map is obtained. In Fig. 3.8 the focal
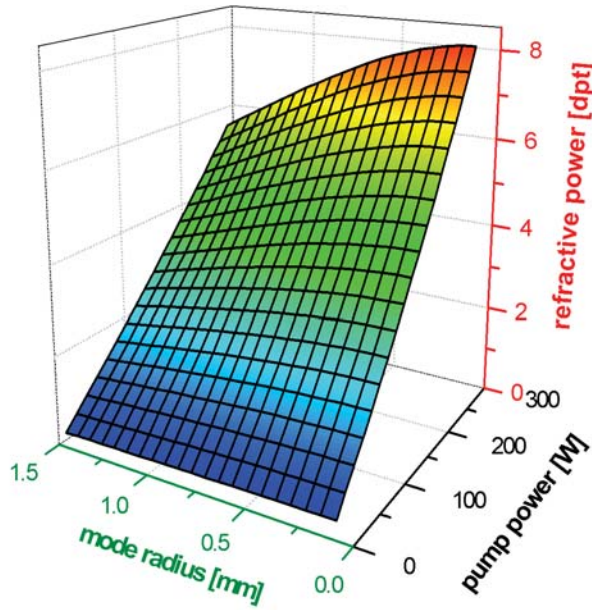
Figure 3.8: Area plot of the refractive power derived by a numerical simulation of the thermal lens depending on beam radius and incident pump power.

length of the thermal lens as a function of the mode field radius and the pump power is plotted. The spanned area can be expressed as a higher-order polynomial function depending on the radius r of the beam and the pump power P. The resulting function that defines the focal length of the thermal lens $f(r, P)$ can then be included in a matrix for the calculation of the resonator's internal beam radii and finally its stability.

Combining Eq. (3.24) with Eq. (3.30), the analysis of a resonator cavity by a periodic sequence of matrices can be extended to higher-order modes as well. A calculation for the beam radii of a few higher-order modes at the position of the first laser crystal of the developed high power laser is given in Fig. 3.9. In the presented diagram two regions can be identified where the solution for the beam radii inside the cavity resulted in real numbers. These types of resonators, in which the stability depends on the focal length of the thermal lens and hence on the pump power are described as dynamically stable resonators in literature [Lör75, Mag86]. Compared with standard fundamental mode cavity designs with limiting internal apertures, dynamically stable resonators offer the following advantages:

- Large mode volumes inside the laser active media are possible, which leads to good pump light to laser beam overlap

- Reduced sensitivity for output power variations induced by pump power fluc- tuations, because the variation of the mode size due to the fluctuation of the

thermal lens inside the laser crystal is at a minimum for the recommended working point.

In Section 4.1.1, guidelines for the realization of a dynamically stable resonator design for a fundamental mode laser are derived and verified in an experiment. The goal of these experiments was to verify that the position of the two stability regions can be controlled by the resonator geometry. It will be shown that the guidelines provided can be adopted to both standing wave and ring resonator configurations in general.
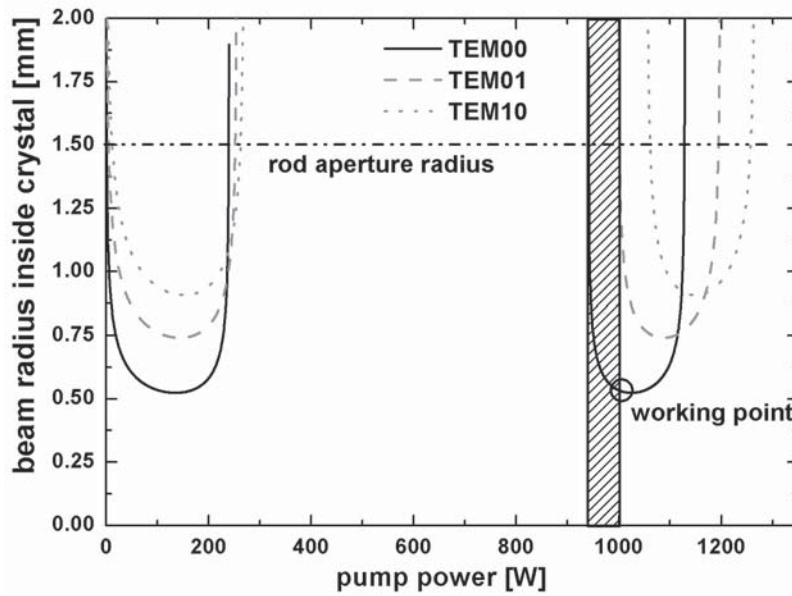

Figure 3.9: Mode size at the position of the thermal lens inside the first of four laser crystals with respect to the summarized incident pump power for different transversal modes.

Due to their greater beam radii compared to the fundamental mode, a lower thermal lens acts on the higher-order modes at the same pump power level. Thus, the region for stable operation of these modes is shifted to higher pump power levels. Consequently, a pump power range, in which only the fundamental mode oscillates, is obtained in the second stability region (shaded region in Fig. 3.9).

3.4   Injection locking

The number of longitudinal modes oscillating in a laser cavity is proportional to the length of the laser active resonator and increases with it. Unfortunately, most concepts for the scaling of output power of solid-state lasers go along with an increase of resonator length. This is mainly influenced by the need for longer and/or additional

active media in a high power laser cavity. One method to attenuate the oscillation
of multiple longitudinal modes and hence to achieve a single-frequency operation is
to insert a frequency-selective optical element (etalon) into the resonator. In many
cases this causes high resonator internal loss and limits the output power of the laser
system. In contrast to that, injection-locking offers a technique to imprint the fre-
quency characteristics of a low power master laser on a high power slave oscillator.
Consequently, it is possible to develop single-frequency laser systems with a high
output power level.

3.4.1 Single-frequency operation

Injection-locking can be described as a frequency synchronization of a free-running
oscillator with a low power, single-frequency signal, which is tuned close to the res-
onance of the oscillator. With this method it is possible to control the frequency
output characteristics of a high power oscillator with a low power seed. This tech-
nique is not limited to laser applications only. It can be applied to mechanical or
electrical setups as well. One of the first theoretical models of a locking phenomena
in an electronic oscillator circuit was described by Adler in 1946 [Adl46]. To develop
stable high power single-frequency solid state lasers for high-precision metrology
various groups investigated the behavior of Nd:YAG lasers under injection-locked
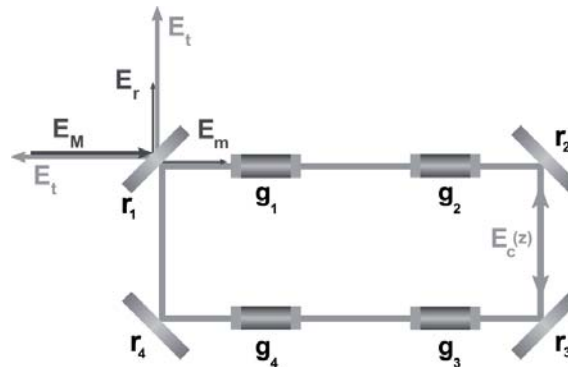conditions [Nab89, Yan96, Zaw02, Fre04, Fre05b] to name but a few.

Figure 3.10: Corresponding field components of an injection locked high power ring oscil-
lator.

In Fig. 3.10 a schematic of an injection locked ring laser with multiple active media
is presented. The incident electromagnetic field of the master laser E_M is partially
reflected at the output coupling mirror r_1 of the cavity resulting in E_r. A fraction of
the light E_m with the amplitude $E_M - E_r$ is transmitted through mirror r_1 into the
high power resonator. In free-running operation, the field of the high power oscillator

$E_c(z)$ is propagating in both directions inside the cavity. In this bidirectional mode of operation light is coupled out at mirror r_1 in two directions with the amplitude E_t for each field.

To simplify the presented model, a combined gain g_{total} for the active media located at different positions g_1–g_4 inside the slave oscillator is assumed. With this assumption, the effect of the localized intensity increase by the different gain media and saturation, which increases over one round trip, are neglected.

To couple both lasers efficiently, the beam width, the waist position and the divergence angle of the seed laser has to be mode matched to the high power slave beam. Therefore, perfect mode-matching is assumed for the following treatment. For large frequency differences between the master laser and the slaves's cavity resonance the injection of the master laser into the slave oscillator cavity has little influence. The injected seed laser is amplified inside the resonator cavity, but no resonance condition of the slave laser internal field is observed for large frequency differences between master laser and slave cavity resonance. Matching the resonator length, and thus the resonance frequency of the high power slave cavity to that of the injected seed, a resonant coupling of both systems can be achieved. The frequency difference between master and slave field, for which a resonant coupling of the high power oscillator to the low power seed is observed, is defined by half the *locking range* $\Delta\omega/2$

$$\Delta\omega = \frac{2\omega_0}{Q_S}\sqrt{\frac{P_M}{P_S}}, \tag{3.33}$$

where ω_0 is the master laser frequency, P_M and P_S are the master laser and the high power slave oscillator output power and Q_S is the quality factor of the slave oscillator cavity. When the slave resonator is near resonance, the round trip gain of the slave oscillator field is transferred to the injected master laser field until the original oscillation inside the slave cavity ceases.

For a description of the injection-locked system characteristics, a treatment of the dynamics of the different laser fields is given below, according to the publications of Siegman and Zawischa et al. [Sie86, Zaw02]. In this brief summary the physics involved during injection-locking will be describe to the extent, which is needed to operate and optimize the laser system presented in this work.

In Fig. 3.11 the amplitude of the different electromagnetic fields, which are involved in the injection-locking process, are shown with respect to the difference between the slave resonance frequency and the frequency of the seed beam. In this diagram the component E_c represents the free running field of the oscillator. Starting with a
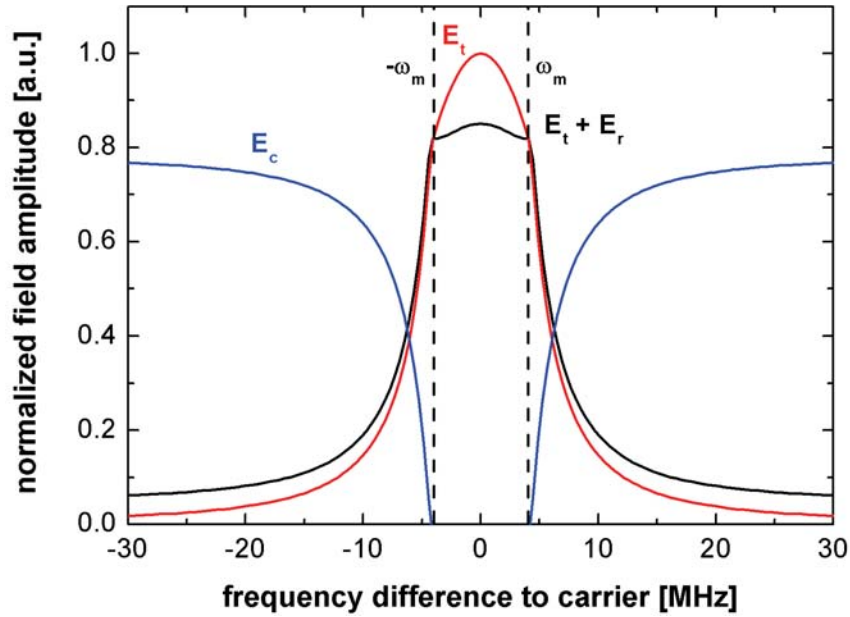
Figure 3.11: Calculated amplitude of the different laser fields when the slave resonator length is tuned [Zaw02].

frequency separation larger than the locking range it can be seen that the power of the slave laser field E_c starts to decrease. As described above, the laser oscillations inside the high power slave stop when the frequency difference is within the locking range. At the same time, when E_c starts to decrease, the field component E_t in transmission of the output coupling mirror in forward direction increases. As the phase properties of the electromagnetic field amplitudes are neglected in this approach the resulting transmitted component E_t is significantly larger than the one of the resulting output field. In fact, the reflected field of the master laser E_r has a phase difference of 180° relative to the field emitted from the cavity when being in resonance. Thus, both fields E_t and E_r interfere destructively, which results in the combined field amplitude given by $E_t + E_r$ in Fig. 3.11.

3.4.2   Pound-Drever-Hall injection locking

For a continuous single-frequency operation of the laser system, an error signal, which measures the frequency difference of the master laser frequency to the slave resonance frequency, has to be generated. An overview of possible frequency stabilization schemes can be found in Ref. [Kno98]. In recent years the Pound-Drever-Hall stabilization technique Ref. [Dre83] was established as the standard for injection-locked single-frequency lasers and passive cavity locking. A recent overview of the Pound-Drever-Hall (PDH) laser injection-locking technique can be found in [Bla01].
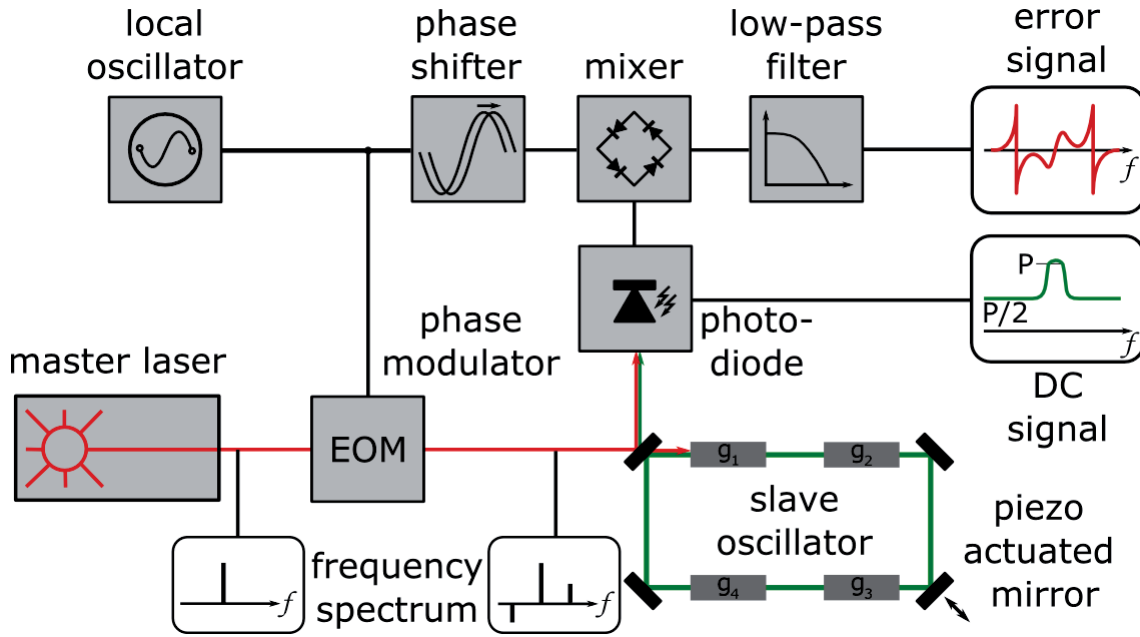
Figure 3.12: Schematic of the control loop for the generation of the Pound-Drever-Hall error signal and the DC signal.

To generate this error signal, which is needed to control the length of the slave laser cavity, frequency sidebands are imprinted on the injected master laser beam by phase modulation. As shown in Fig. 3.12, these sidebands are generated within an electro-optical modulator (EOM) installed in the master laser beam path. Both sidebands are inversely phased and have a relative phase difference of π and a frequency difference from the carrier corresponding to the modulation frequency of the EOM Ω. The electric field of the master laser after the EOM is then described by

$$E_i = E_m \exp\left(i\left(\omega t + \beta \sin \Omega t\right)\right), \tag{3.34}$$

where β is the modulation index, which defines the amplitude in the carrier and sidebands. An approximate expression using Bessel functions J_n of the order n is then given by [Zaw02]

$$
\begin{aligned}
E_i &\approx \left[J_0(\beta) + 2iJ_1(\beta)\sin\Omega t\right]\exp\left(i\omega t\right), \tag{3.35}\\
&= E_m\left[J_0(\beta)\exp\left(i\omega t\right) + iJ_1(\beta)\exp\left(i(\omega+\Omega)t\right)\right.\\
&\quad\left. -iJ_1(\beta)\exp\left(i(\omega-\Omega)t\right)\right]. \tag{3.36}
\end{aligned}
$$

From this equation one can see that there is a master laser beam incident on the slave cavity oscillating with three different frequencies: a carrier with the angular

frequency ω and the two sidebands with $\omega \pm \Omega$. When the resonance frequency of the slave oscillator is near the locking range the sidebands are non-resonant inside the cavity. As a consequence, the sidebands are reflected at the output coupler. At the same time, a fraction of the carrier beam can enter the resonator, picking up phase with each round trip with respect to the reflected part of the incident seed beam. This phase shift per round trip of $\theta = \omega \cdot L/c$ depends on the length L of the slave resonator, which is controlled by a piezo actuator.

A fraction of the high power beam transmitted by the output coupler is focused on a fast photodetector (corner frequency >60 MHz). With this so-called *locking photodiode* the interference of the phase shifted carrier coupled out from the slave resonator with the reflected fraction of the seed beam is detected. Together with the reflected, non-resonant sidebands an amplitude modulated signal is generated. The phase of this electrical signal is proportional to the frequency difference of seed beam carrier and resonance frequency of the slave cavity.
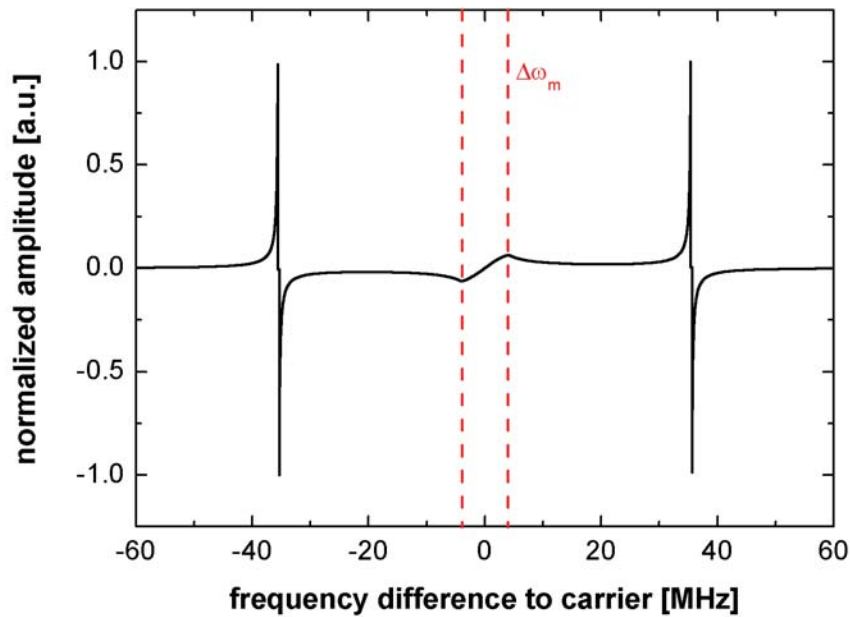

Figure 3.13: Calculated error signal for a master laser with 35 W incident on the output coupler of the high power slave. The slave laser has a free-running total output power of 175 W in bidirectional operation, the modulation depth of the EOM was set to $\beta = 0.03$, and the modulation frequency for the sidebands was 35.5 MHz.

The signal coming from the photodetector is then mixed with the frequency reference of the local oscillator driving the EOM. To compensate for the time delay between detected signal and the local oscillator reference a variable phase shifter is introduced

between local oscillator output and the electrical ring mixer input. With a low-pass-filter the fast fluctuations at twice the modulation frequency are suppressed.

The resulting signal obtained by the PDH technique is a frequency dependent dispersive control signal, called PDH error signal in the following text, which has an asymmetric signal sequence (the slope of the sideband resonance is inverse to carrier resonance). A calculated error signal for the laser system presented in this work is given in Fig. 3.13.

The center part of the PDH error signal defines the region, in which the slave oscillator field has ceased and only light with the seed laser's frequency is emitted. In fact, the maximum and minimum of the central slope define the beginning and end of the locking bandwidth, in which the free oscillation of the high power slave extinguishes. The two additional peaks of the PDH error signal appear at a frequency difference to the carrier, for which the slave cavity is resonant for the sidebands. As the slopes of these sideband resonances have an inverse sign in respect to the signal within the locking range they can be electronically excluded for the locking process.

For an active resonator length control, the error signal is processed by a PID controller element to stabilize the PDH signal at the zero-crossing. For a faster detection of the position of the central error signal, the output power of the laser system in transmission is analyzed. As it increases within the locking range (Fig. 3.11), a power threshold can be set to activate the control loop. The generated signal from the active proportional, integral and differential controller (PID) is then sent to a high-voltage driver, which is connected with the piezo actuated mirror of the slave oscillator resonator. With this scheme an automated lock acquisition can be achieved.

Chapter 4

High power oscillator development

The focus of this chapter is the description of the design and development process that led to the design of the injection-locked high power laser. In particular, the development of the four head Nd:YAG ring oscillator, whose optical resonator concept and mechanical design was established during this work, is presented. This ring oscillator consists of four modular units, called *laser heads* in the following text. These modules, which can be preassembled separately, combine pump light source, imaging optics and laser crystal on one optical bench. As the laser heads are the key parts of the four head ring oscillator, an extensive description of the development and validation process of these components will be given in this chapter.

However, before the mechanical construction for the final design of the high power oscillator could start, a stable resonator configuration to suppress higher-order mode oscillations had to be found. To eliminate the influence of rather complicated alignment procedures for ring resonators, a standing wave testbed laser was built. With this laser system, consisting of two adjacent laser head modules, different resonator configurations were studied.

4.1 Mode discrimination by resonator geometry

As described in Section 2.3 the high power ring oscillator will be coupled to a 35 W MOPA system with a Gaussian intensity distribution to obtain a single-frequency output beam. To achieve the best overlap of the injected seed with the high power slave beam, and thus the best mode-matching of the beam inside the oscillator's cavity, the high power ring oscillator has to have a Gaussian output beam profile as well. In the following section a method for the discrimination of higher-order modes by choice of resonator geometry is presented. Instead of intracavity apertures to increase the losses for the higher-order modes, the presented technique relies on the

limiting apertures of the optical elements and the shape of the thermal lens inside the pumped Nd:YAG crystals.

4.1.1 The two head laser

The aim of the following experiments was to find an optimum resonator configuration in which the output power, the beam profile and the misalignment sensitivity were improved compared to the previous laboratory prototype laser developed by Frede [Fre07a]. In general, the optimization of laser ring resonators is more difficult compared to standing wave cavities. To change the parameters, such as resonator lengths, lens positions, mirror alignment and reflectivity, a more flexible testbed laser based on a U-shaped standing wave cavity was used for the following experiments. It is less critical to align than a comparable ring laser setup and hence allows one to test various resonator configurations with adequate alignment repeatability. On the other hand, the results gained with this simplified laser setup are transferable to the high power oscillator's resonator design with good agreement as will be shown in Section 4.1.3.
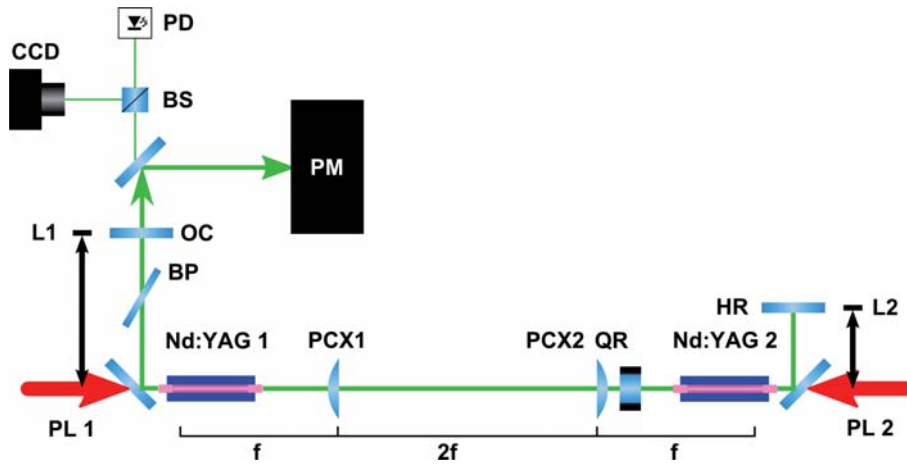

Figure 4.1: Optical setup of the two head standing wave laser: The output coupler (OC) mounted on an optical rail, the highly reflective mirror on a linear stage (HR), the depolarization compensation consisting of two lenses (PCX1,PCX2) and a quartz rotator (QR), the Brewster plate (BP) and the two significant lengths of the cavities L1 and L2 measured from the dichroic 45° mirror to the associated mirror at the end of the resonator arm. The incident pump light (PL1,PL2) is injected through the dichroic turning mirror into the end facet of laser crystal 1 and 2 (Nd:YAG1,NdYAG2).

As shown in Fig. 4.1 the two end-pumped Nd:YAG laser crystals were oriented opposite of each other with a distance of 400 mm in between. Using a flat highly reflective mirror (HR) and a flat output coupling mirror (OC) a U-shaped standing

wave cavity was formed. On the left hand side of the setup in Fig. 4.1 an optical rail with an adjustable mirror mount at a distance L1 to the dichroic turning mirror was placed orthogonally to the laser head. The position of this rail was matched to the optical axis of the laser beam deflected by the dichroic 45° mirror. On the right hand side a linear stage with a translation range of 300 mm was installed. Mounted on this linear stage was an adjustable mirror mount with a high reflection coated flat mirror inside. The position of the mirror in respect to the dichroic turning mirror is given by the distance L2. The reflectivity of the output coupler was chosen to be R=75%.

The linear output polarization of the laser beam was achieved by a glass window inserted in Brewster angle inside the resonator. This Brewster plate (BP) causes a loss of $\approx 25\%$ for the vertical polarization of the resonator internal beam, because of reflection. The horizontally polarized beam is not affected by the Brewster plate. Because the field inside the resonator tends to operate in a configuration with the lowest possible losses the horizontally polarized field is favoured for oscillation.

As described in Section 3.1, the birefringence of the doped Nd:YAG crystal strongly depends on the incident pump power. This thermally induced birefringence limits the output power, which can be extracted from a single rod in the fundamental mode to approximately 40 W [Mur96]. This limitation, which is caused by bifocussing and depolarization can be compensated for by a standard depolarization compensation scheme [Sco72, Lü95a, Lü96, Kug97, Cla99, Fre04].

The simplest setup to compensate for the thermally induced depolarization of the laser beam in multi-rod Nd:YAG lasers is to insert an optical element between the crystals, which rotates the polarization by 90°. Standard setups rely on a 90° quartz rotator, which is insensitive to high laser beam intensities and thus is commonly used in high power applications. Passing through the first crystal, the linear polarization of the intracavity laser beam gets distorted. When the beam, whose polarization is rotated by 90° by the quartz rotator, enters the second crystal, its tangential and radial depolarization components are interchanged. For equally pumped crystals, the propagation through the second laser rod then rotates the tangential and radial polarization components back to their original state.

This scheme only works to a specific extent and does not allow for compensation of the complete depolarization losses inside the resonator cavity [Lü96], because the beam propagates through both active elements on a different path due to the strong thermal lenses inside. For an improved depolarization compensation an imaging system consisting of additional two identical lenses has to be inserted between the laser crystals. The distances between these two lenses is set to twice the focal length

of one lens (2f) acting as a one-to-one telescope (4f imaging system). If the distance from one lens to the principal plane of the thermal lens inside the Nd:YAG crystal is equal to its focal length f, the laser beam is imaged from one crystal to the other. For the lasers in this work, the depolarization losses determined by the amount of light reflected at the resonator internal Brewster window could be reduced to less than 1% of the laser's output power. Approximately a quarter of the depolarized light inside the cavity is reflected at the rear and front surface of this Brewster plate. The reflected light can be used as an indicator for the alignment quality of the depolarization compensation. A further reduction of the depolarization losses is limited by the positioning accuracy of the 4f-lenses and thus the remaining misalignment of the optical imaging system [Kug97] and by a slight mismatch of the laser beam paths inside the opposing laser crystals.

For the two head laser, two fused silica plano-convex lenses (PCX1 and PCX2) with a focal length of 112 mm were used for the 4f-imaging setup. The distance between both lenses was set to 224 mm as required. The quartz rotator (QR), which is made of a 14 mm long crystalline quartz with a refractive index of 1.53 at 1064 nm is positioned between PCX2 and the second laser head (Fig. 4.1). To image the principal planes of both crystals onto each other the optical path length differences resulting from the higher refractive indices of QR and the Nd:YAG crystals in respect to air were taken into account.

For diagnostics, the output beam of the two head standing wave laser is deflected by a high reflection coated 45° mirror and sent to a 300 W Ophir FL300-A thermopile power meter (PM in Fig. 4.1). Furthermore, the beam transmitted through the turning mirror in front of the power meter is split by a 50/50 beam splitter (BS) cube. One of these two beams, with a low power of approximately 8 mW each, was monitored by a CCD camera for visual feedback of its spacial intensity distribution (CCD). The other was analyzed with a fast InGaAs photodetector (PD) with a bandwidth of 3.5 GHz (EOT-3500) for a beat signal measurement of the oscillating higher-order modes [Sie86]. In Fig. 4.2 beat signals are shown, which were taken at different working points of the laser. It can be seen that above a specific pump threshold, higher-order modes start to oscillate inside the cavity (b). As higher-order modes have oscillation frequencies different from that of the fundamental mode, beat signals of these frequency components can be detected. These beat notes, represented by spikes in the spectrum of the detected signal, can be distinguished from the beat signals of the longitudinal modes of the TEM_{00} mode (a) by their height and position. An increase of pump power leads to a multi-mode operation, which is then indicated by a train of different beat notes in the signal (c). Actually, this measurement is an

adequate tool to determine a working point with high output power and negligible amount of higher-order modes (no, or only temporarily, visible beat notes with low relative height compared to the fundamental mode).
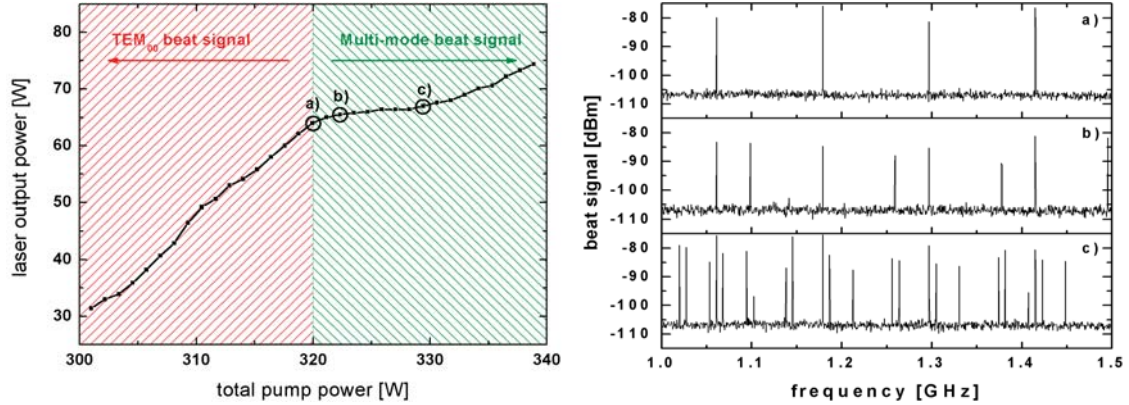

Figure 4.2: **a)** Beat signals taken at normal operation point, **b)** slightly (+4 W more pump power) above the operation point, and **c)** in multi-mode operation of the standing wave two head laser system.

As described in Section 3.3 the thermal lenses inside the laser gain media led to a stability range strongly depending on the incident pump power and resonator geometry. Furthermore, higher-order modes experience a lower thermal lens by which their stable operation point is shifted to higher pump power levels. A calculation of the mode radii inside the first laser crystal for different arm length setups, based on the ABCD matrix method described in Section 3.3, is given in Fig. 4.3. From these diagrams it can be seen that there is no gap in the stability range for a symmetric resonator (a). Increasing both arm lengths symmetrically shortens the stability range in terms of applicable pump power and increases the beam diameter (b), which limits the maximum extractable output power of the laser. Using a slightly asymmetric arm length setup for the laser resonator, the stability range splits into two different regions (c). Unfortunately, the gap between both regions is not large enough, so that higher-order modes, whose point of stable operation is shifted to higher pump power levels, can couple from the first stability region into the second. The fourth and most interesting option is to increase the asymmetry of the resonator arms further and enlarge the gap between both stability regions (d).
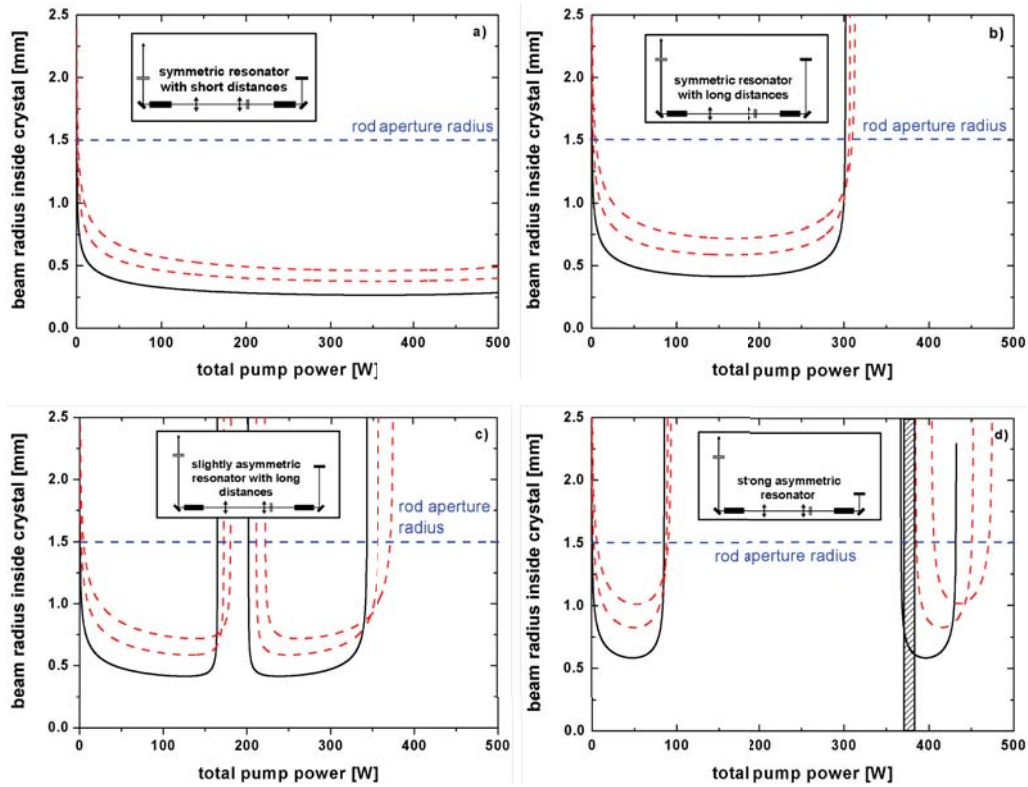
Figure 4.3: Beam diameter inside the Nd:YAG crystals for different two head standing wave laser configurations depending on the incident pump power. **a)** Symmetric short resonator configuration L1 = 100 mm and L2 = 100 mm, **b)** symmetric long arm resonator configuration L1 = 250 mm and L2 = 250 mm, **c)** slightly asymmetric resonator configuration L1 = 250 mm and L2 = 200 mm, and **d)** strongly asymmetric resonator configuration L1 = 500 mm and L 2= 100 mm

4.1.2 Power-scaling

With the two head standing wave setup a mapping of different resonator configurations was performed. For this mapping process the laser resonator lengths were set up to provide the initial TEM$_{00}$ operation point at a combined pump power of 320 W as a reference. This point of operation was chosen, to have enough safety margin not to exceed the maximum available pump power level of 400 W for this setup from the beginning. The corresponding resonator arm lengths for this operation point were 480 mm for the OC-mirror side (L1) and 135 mm for the HR-mirror side (L2). The distance between the deflecting mirror and the laser crystal was 17.5 mm, which has to be added to the resonator arm lengths L1 and L2 in the numerical calculations. With this configuration an output power of approximately 65 W was obtained.
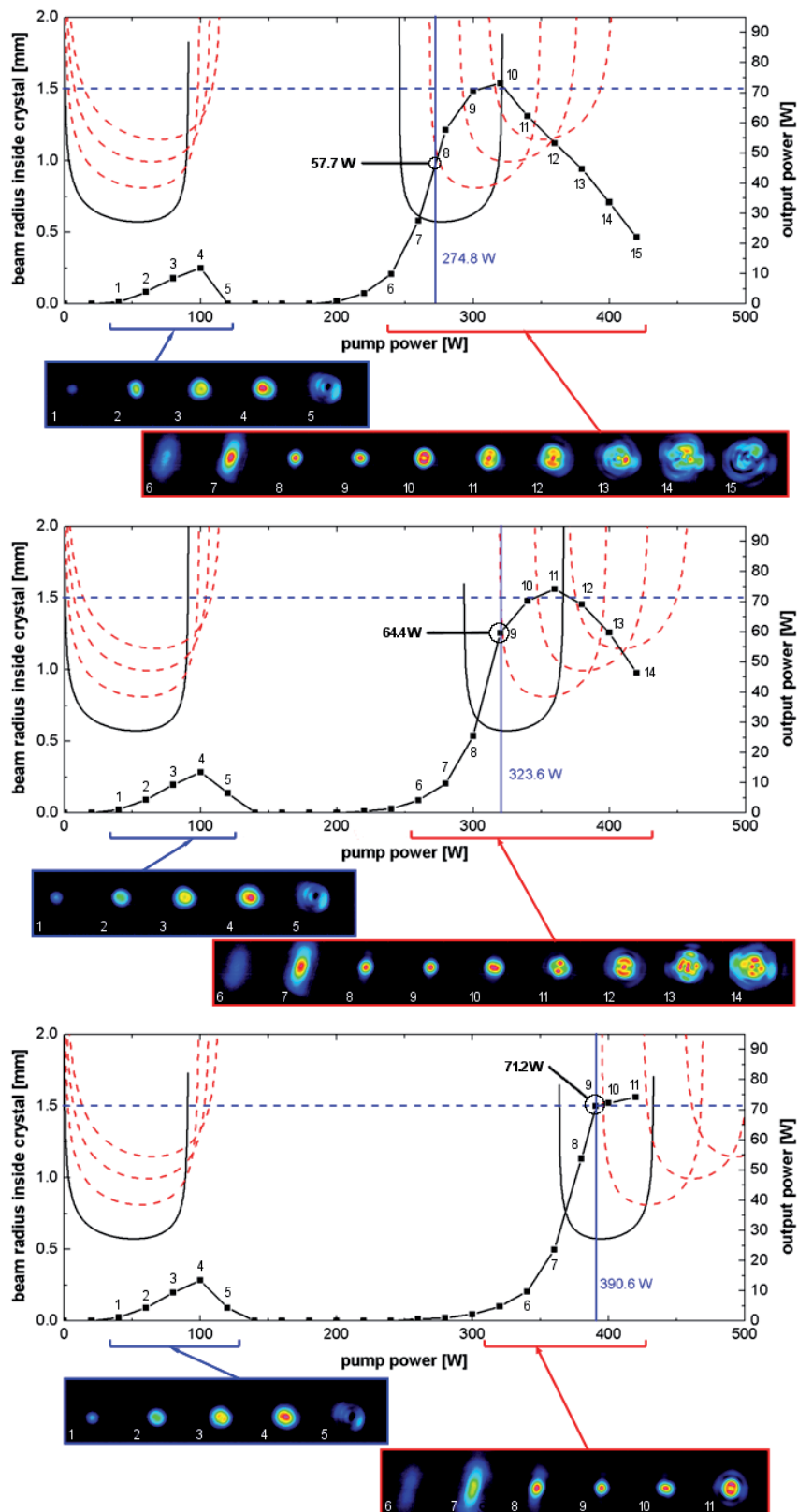
Figure 4.4: Variation of the short arm length distance L2 to the 45° mirror of the standing wave cavity from 165 mm (**Top**) over 135 mm (**Middle**) to 105 mm (**Bottom**). The solid blue line indicates the power, for which the TEM$_{00}$ operation was verified by a beat signal measurement.

In Fig. 4.4 the output characteristic of the two head laser system for different lengths of the short arm L2 are displayed. At each of the three presented resonator configurations the output power with respect to the incident total pump power is given. For each measurement point, indicated by a square symbol, a beam profile was taken with the CCD camera. Brackets below the graphs indicate the first and second region of stability and refer to the corresponding images. A vertical line specifies the point of operation for which no indication of higher-order transversal modes could be found in the beat signal measurement. The output power in a fundamental mode is given and indicated with a circle in the diagram. A dashed horizontal line gives the rod aperture as reference for the smallest aperture present in the laser resonator. For a more precise determination of the TEM_{00} working point the pump power was varied in small increments below the measurement point, for which higher-order modes were observed in the beat signal for the first time. To compare the theoretical model of a dynamically stable laser resonator given in Section 3.3 with the measured data, the calculated beam radius inside the laser crystals for various transversal modes with respect to the pump power level is plotted in the corresponding graphs. It can be seen that the point, where the first higher-order mode is getting theoretically stable, coincides with the measurement represented by the vertical line with good agreement.
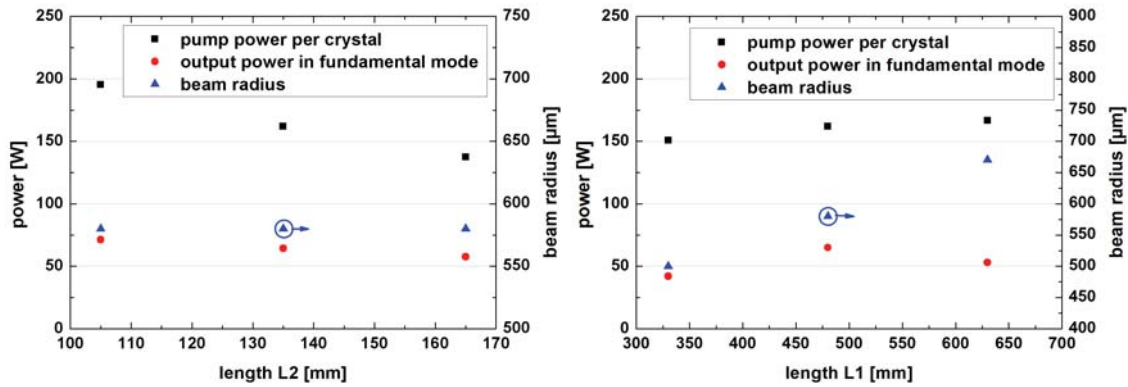

Figure 4.5: Applied pump power per laser crystal (black squares) of the two head standing wave laser and their corresponding output power (red circles) for different resonator lengths of L1 and L2, respectively. For each point of operation the calculated beam radii (blue triangles) are given. **a)** Resonator length variation of L2 with L1 = 480 mm. **b)** Resonator length variation of L1 with L2 = 135 mm.

From Fig. 4.5a it can be seen that the applicable pump power level for a fundamental mode operation is linked to the short arm length L2 of the standing wave resonator. In detail, an arm length L2 of 165 mm results in a fundamental mode working point at a pump power level of approximately 275 W. With this resonator configuration

an output power of 57.7 W in the fundamental mode was obtained. The second and third graphs in Fig. 4.4 show that a decrease of the short arm length increases the applicable pump power for the fundamental mode working point, resulting in a higher overall output power level. For an arm length of L2 of 135 mm an output power of 64.4 W was obtained. An even shorter arm length L2 of 105 mm results in an output power in the fundamental mode of 71.2 W. In addition, the numerical calculations of the mode size radius indicate a constant TEM_{00} radius inside the laser crystals of 580 μm for all three resonator configurations, as seen Fig. 4.5a.

In a second experiment, the influence of the variation of the length L1 on the laser's fundamental mode working point and performance was investigated. For this purpose, the short arm length L2 was set to 135 mm. In Fig. 4.5b and Fig. 4.6, which comprises the same formatting scheme as Fig. 4.4, the obtained results are presented. The measurement was started with an arm length for L1 of 480 mm. For this resonator configuration the output power level and fundamental mode working point obtained during the L2 variation measurements (pump power 320 W in total) could be reproduced within the measuring accuracy, as seen in Fig. 4.5b. The achieved fundamental mode output power was 65 W.

In a first step, the arm length L1 was shortened by 150 mm to a length of L1 of 330 mm. In the numerical calculations it can be seen that the minimum achievable mode field diameter inside the laser crystal is reduced. As described in Section 3.3 the effective thermal lens for a laser beam propagating through an end-pumped laser crystal rod strongly depends on its mode field diameter. An overall reduction of the mode size inside the laser crystal leads to a reduction of the refractive power difference amongst the resonator internal Laguerre modes, as the deviation of the aspherical thermal lens profile from an ideal lens increases with radial distance from the crystal center. This leads to a convergence of the higher-order modes stability zones in direction of the one of the TEM_{00} mode. As a consequence, for this resonator configuration the applicable pump power for the fundamental mode operation point is lower. Furthermore, the overall beam radius of the TEM_{00} inside the crystal is 80 μm less than for the L1 = 480 mm case. This reduces the overlap between the pump light and the laser beam, which negatively affects the output power level even further. The measured output power level for this configuration was 42 W.
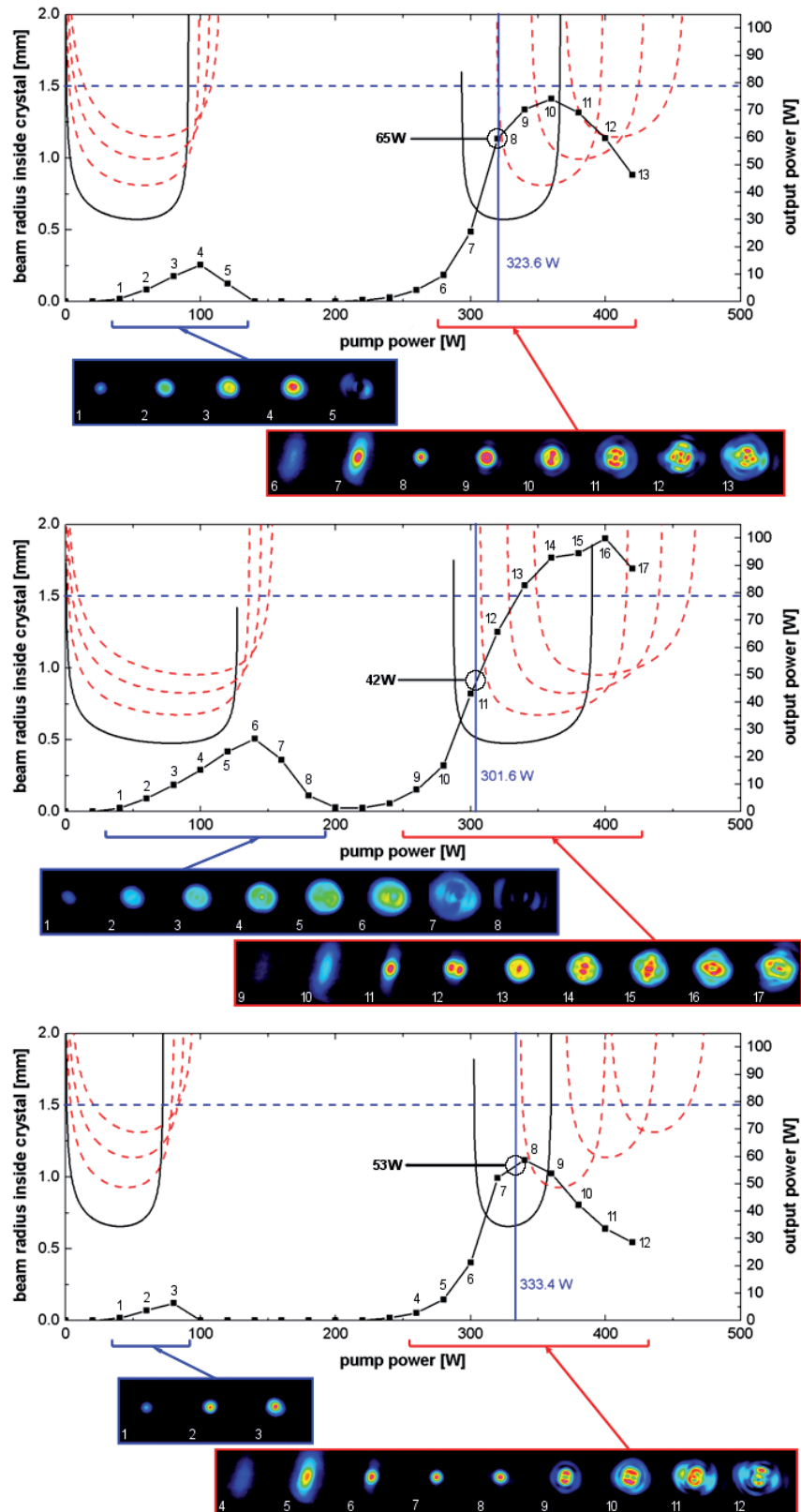
Figure 4.6: Variation of the long arm length distance L1 to the 45° mirror of the standing wave cavity from 480 mm (**Top**) over 330 mm (**Middle**) to 630 mm (**Bottom**). The solid blue line indicates the power, where the TEM_{00} operation was verified by a beat signal measurement.

By comparison, the calculated fundamental mode field diameter for an increased arm length L1 of 630 mm indicates that the minimum achievable beam diameter inside the laser crystal is larger. Consequently, the difference in refractive power of the thermal lens for the higher-order modes significantly differs from the one of the fundamental mode. This increases the pump power gap between the stability regions of the resonator internal modes. In this laser configuration, the fundamental mode is diffracted at the aperture of the laser crystal due to its larger beam radius of 670 μm. In fact, the beam radius of the fundamental mode is limited by the laser crystal aperture to a maximum of 650 μm (for a beam with less than 1 % of power in diffraction, the diameter of the aperture has to be less then $d_A = 4.6 \cdot \omega_0$ [Sie86]). Thus, the side-lobes of the given Gaussian intensity distributions are slightly diffracted at the rod aperture with a diameter of 3 mm (the optimum laser crystal design was determined in experiments performed by Frede and Puncken [Fre07a, Pun11]). By contrast to the setup with the shortened length of L1 = 330 mm, only a slight output power drop (53 W instead of the optimum at 65 W) by the resonator internal diffraction was observed. In conclusion, it was shown that an asymmetric resonator configuration can be utilized to control the fundamental mode operation point. In fact, the two zones of stability, generated by a dynamically stable asymmetric resonator, enables one to use the aspherical thermal lens as a higher-order mode discriminating optical element. Moreover, the control of both resonator arm lengths gives control of the applicable pump power at a fundamental mode output and the mode size volume, respectively.

Varying the short arm length of the cavity, the second zone of stability is shifted with respect to the applied pump power levels, thus power-scaling is possible by decreasing this length. Vice versa, the laser resonator can be easily adapted to any desired pump power by changing this length L2. Carefully setting the long arm length L1 of the cavity, the mode field diameter in the crystal is optimized. This enables one to optimize the overlap of the pump light distribution and laser light inside the active media. Even though an impact on the laser's efficiency can be seen with the large variations tested, the long arm length L1 is less sensitive to length variations than the short arm length L2. Furthermore, the beam quality can be slightly enhanced by the appropriate choice of the resonator length L2, as the laser beam radius has to stay below the critical value in order not to be diffracted at the crystal's aperture.

In addition, it will be shown in the following chapter that the basic fundamentals for higher-order mode discrimination by an asymmetric resonator geometry can be easily adapted to a ring laser structure.

4.1.3   Four head resonator setup

In the previous section optimization guidelines for a fundamental mode standing wave resonator with the best higher-order mode discrimination have been presented. Following these guidelines, a high power ring laser was built, which was optimized to form an asymmetric cavity. As mentioned previously, it is crucial for output power-scaling of this laser concept to support a mechanical setup with an asymmetric resonator arm that can be shortened to adapt the laser's working point to a desirable pump power level.

To scale the output power of the testbed two head laser into the 200 W region, the standing wave setup was duplicated to form a four head ring resonator laser. This scaling concept is advantageous because all thermal effects studied in the two head laser experiments are applicable to the four head laser in the same manner. Additionally, the numerical resonator simulation software can be easily adapted to the ring resonator structure of the four head laser.
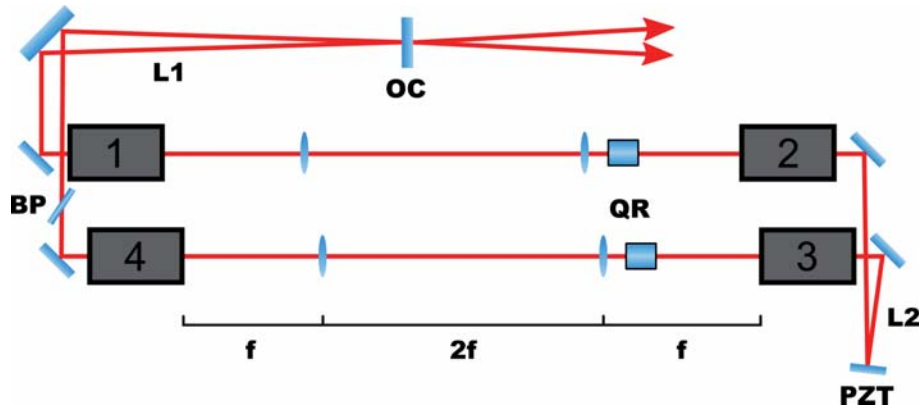

Figure 4.7: Schematic of the asymmetric resonator with laser crystals (No. 1 – 4), 90° polarization rotating quartz crystal (QR), output coupling mirror (OC), uncoated Brewster plate (BP), piezo actuated mirror (PZT), long arm length (L1) and short arm length (L2).

As shown in Fig. 4.7, two pairs of laser head modules (LH 1–4) are positioned opposing each other. Between these laser heads a birefringence compensation identical to the one described in Section 4.1.1 was installed. As the resonator requires a length actuator for injection-locking, the HR mirror of the short arm (L2) was glued on top of a piezo actuator (PZT). In contrast to the two head setup, the long arm length L1 was folded by a 45° turning mirror to reduce the form factor of the high power ring laser. The reflectivity of the output coupler was adapted to R = 50 %, following the guidlines for the selection of output coupling ratios for injection-locked high power lasers given in Ref.[Fre07a].
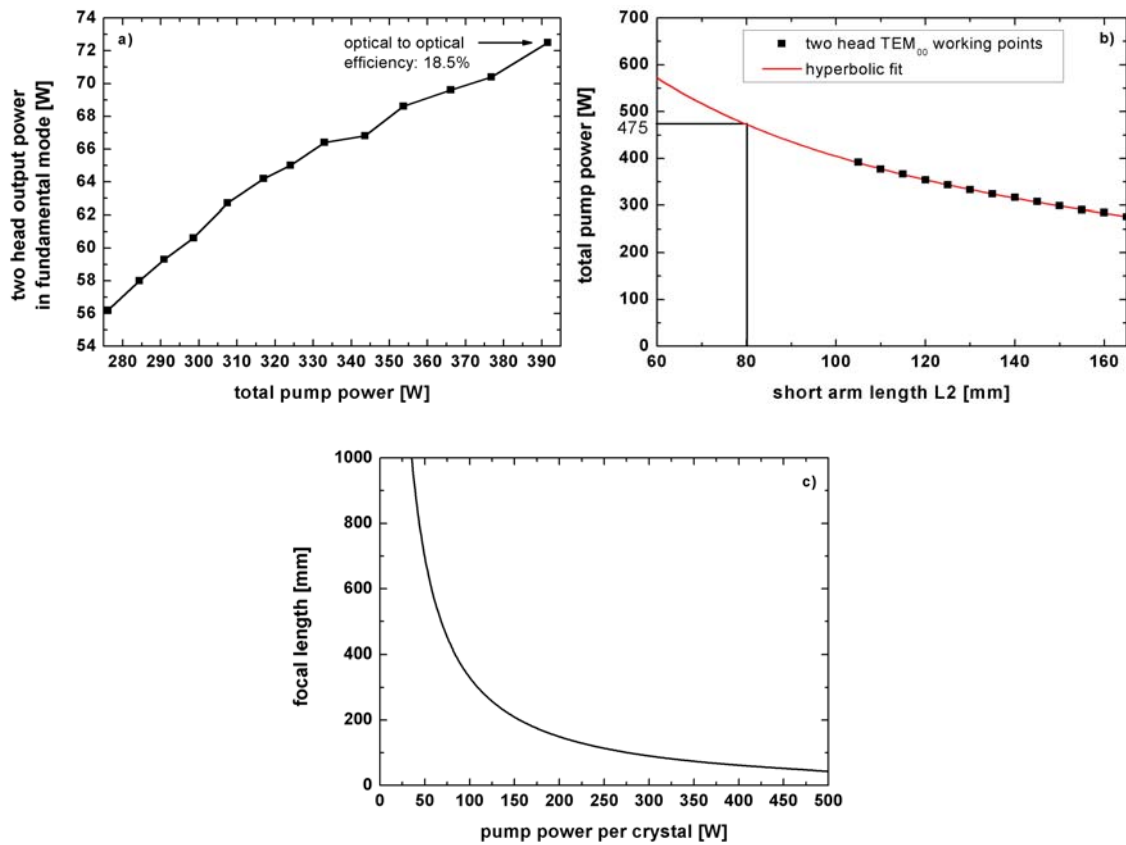
Figure 4.8: **a)** Output power at the fundamental mode operation point in respect to the adapted short arm length L2 of the two head standing wave laser. **b)** Fundamental mode output power levels for different total pump powers of length adapted two head resonator configurations. **c)** Calculated focal length of the pump power dependent thermal lens inside the laser crystal.

To fulfill the final design requirements regarding the output power specification of the injection-locked free-running laser system ($>$ 200 W, see Table 2.1) an output power level of 175 W in bidirectional operation was desired for this ring laser. To achieve such a high output power in the fundamental mode, the pump power level had to be adjusted. The results obtained with the two head experiments indicated that an increase in pump power requires a further shortening of the short arm length. Furthermore, the data obtained during these experiments was used to assume starting point parameters for the optimization of the four head resonator configuration.

In Fig. 4.8a the output power slope for fundamental mode operation points of the two head system is plotted. Each data point was taken at a different short arm length L2, starting from 105 mm with an incremental step of 5 mm. The maximum achieved output power was 72.5 W, which corresponds to an optical to optical efficiency of approximately 18.5%. Projecting the required output power level for the four head

system onto the two head laser, half the power in fundamental mode, 87.5 W, is desired. Taking the optical to optical efficiency value given above into account, the fundamental mode output power of 87.5 W can be converted into an estimate of the required pump power of 475 W.

To determine the corresponding short arm length for this fundamental mode operation point, pump power levels used within the two head experiment in relation to the length L2 are plotted in Fig. 4.8b. From the previous experiments one can deduce that changing the short arm length L2 leads to higher applicable pump power at the fundamental mode operation point and thus a decreased focal length of the thermal lens inside each crystal. In fact, this focal length changes hyperbolically (see Fig. 4.8c) as it is proportional to the pump power. This hyperbolic curve progression is also visible in the data points of Fig. 4.8b. Applying a hyperbolic fit function to the given data in Fig. 4.8b, a prediction for the required short arm length L2 for an pump power level of 475 W was performed.

The determined values were then projected on the high power ring oscillator, which resulted in the following set of start parameters for first testing:

- Short arm length of L2 = 2×80 mm = 160 mm from turning mirror in front of crystal No. 2 to turning mirror at crystal No. 3.

- Combined pump power of 950 W, which corresponds to an incident pump power of 237.5 W per laser crystal.

- Desired output power of 175 W in bidirectional operation of the ring laser.

- Long arm length L1 set to a starting length of two times L1 from the two head experiments, resulting in L1 = 960 mm.

In the first experimental run of the high power ring laser, an optimized configuration for the laser was found for an adapted length L2 = 880 mm and a slightly higher combined pump power of 960 W. All other parameters were kept unchanged. For this laser setup an output power over pump power slope was measured. In addition, the pump power dependent regions of stability for different higher-order modes were calculated for the actual resonator configuration. For both types of data, measured and calculated, a first region of stability can be seen at low pump power levels in Fig. 4.9. Furthermore, the point for optimal fundamental mode operation predicted by the resonator calculations coincides with the actual working point of the laser within an accuracy of ±2 W of pump power. After a short warm up period of less than one minute an output power of 172 W was achieved. The corresponding
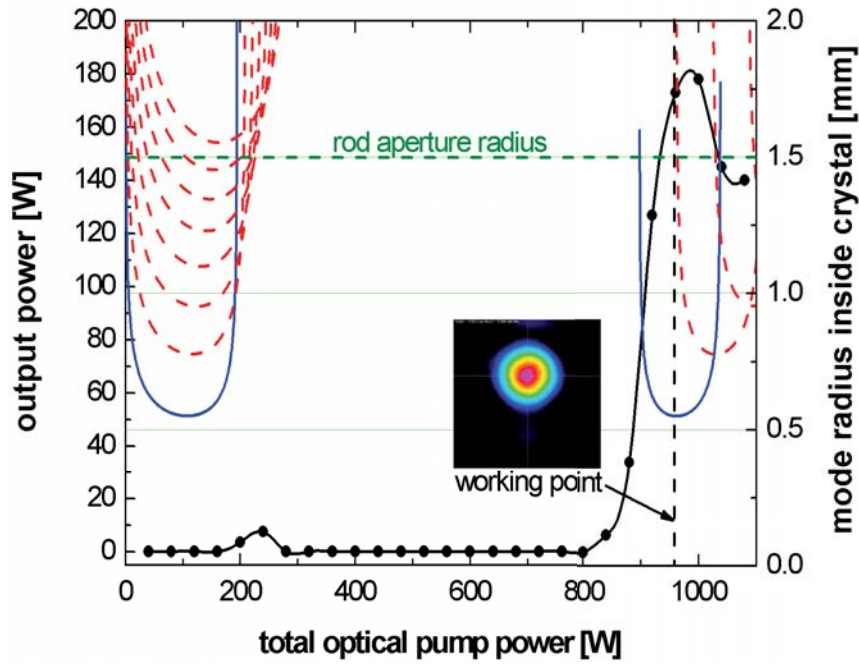
Figure 4.9: **Black**: Output power over pump power of the high power ring laser. **Blue and red**: Numerical ABCD calculations of the mode field radii of the TEM_{00} (blue) and higher-order modes (red) inside the laser crystals of the four head ring oscillator.

fundamental mode beam profile is plotted inside the output power slope diagram in Fig. 4.9 as a reference.

The evaluated configuration of the four head ring laser was then taken as a reference for the mechanical implementation of all needed laser components forming the final design of the high power oscillator. As three laser systems had to be produced, the experimentally determined lengths of the resonator might slightly change with varying quality of the optical components. To be able to compensate for different resonator lengths the design of the ring laser structure had to be kept as modular as possible. For this purpose and to be able to assemble all subcomponents in one production step a uniform structure for each laser head was developed. A detailed overview of this main components of the high power oscillator setup will be given in the following section.

4.2   Laser head module

In this section the mechanical and optical assembly of a laser head module is presented. In the previous Section 4.1 it became obvious that a the crucial part for scaling the output power of the high power ring oscillator was to reduce the short

arm length L2. For this purpose the mechanical design of the laser head structure was optimized for a narrow width to decrease the space between the optical axes of the two adjacent modules to a minimum. A picture of one laser head module can be seen in Fig. 4.10.
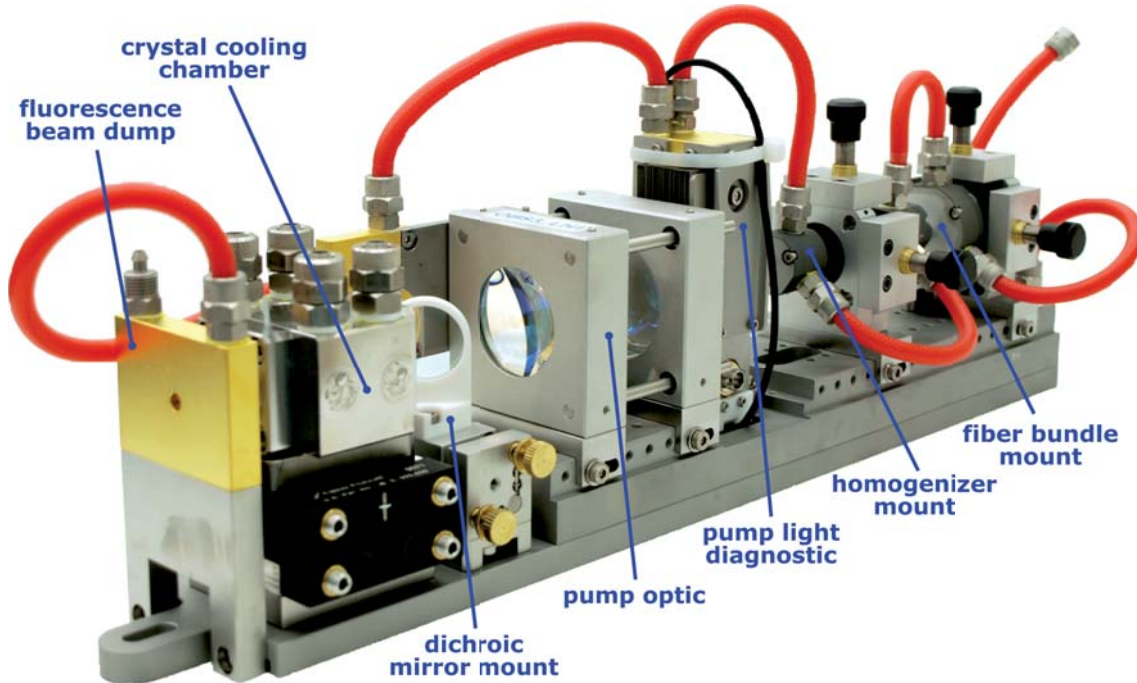

Figure 4.10: Picture of a fully assembled laser head.

In Fig. 4.11 the schematic layout of a laser head is presented. The main functionality of the laser head module is to incorporate all optical and mechanical components needed for pumping of one Nd:YAG laser crystal on an optical bench (g). As mentioned above, the laser crystal is longitudinally pumped by fiber coupled semiconductor lasers. Seven 400 μm multi-mode fibers are used to guide the pump light from the source to each laser head. The bare end tips of these fibers are bundled and glued into an aluminum ferrule for mounting (a). Directly imaging the polished fiber end tips into the laser crystal would result in a non-uniform pump light distribution. To avoid beam distortions induced by this so called *hot spot pattern*, a glass rod with 100 mm length and 2 mm diameter was placed with a very thin air gap downstream of the fiber bundle (b). By total internal reflection, the pump light distribution gets homogenized. At the end of this *homogenizer* the pump light profile can be approximated as a Gaussian distribution with an intensity plateau (background). Passing a diagnostic unit for wavelength and power monitoring (c) the light is imaged by two lenses with a focal length of 50 mm into the laser crystal (d). The pump spot

generated by the *pump light imaging optic* is located at the beginning of the doped region of the laser crystal rod (f). Before the pump light enters the laser rod through its undoped end-caps, it passes a deflecting mirror (e), which is coated with a high transmission coating for the pump wavelength at 808 nm on one side. On the other side of the mirror, a dichroic coating with low losses for the incident pump light and high reflectivity for the laser wavelength at 1064 nm is applied. The laser crystal itself has a length of 54 mm. It has two undoped end-caps, each of 7 mm in length to prevent bulging of the end facets and to be able to fix the rod with PTFE o-rings on the crystal cylinder, which are needed to seal the water cooling chamber. To generate a more uniform absorption over the crystal length and hence a more uniform axial temperature distribution, a low Nd^{3+} doping concentration of 0.1 at% was chosen. Combined with a pump light double-pass, these crystals allow for a higher pump power level before thermal fracture and guarantee a reduction of beam distortions compared with a 0.2 at.% doped crystal in a single-pass configuration. In this setup, the heat generated inside the laser rod under pumping conditions is dissipated by direct water cooling of the cylindrical surface of the crystal.
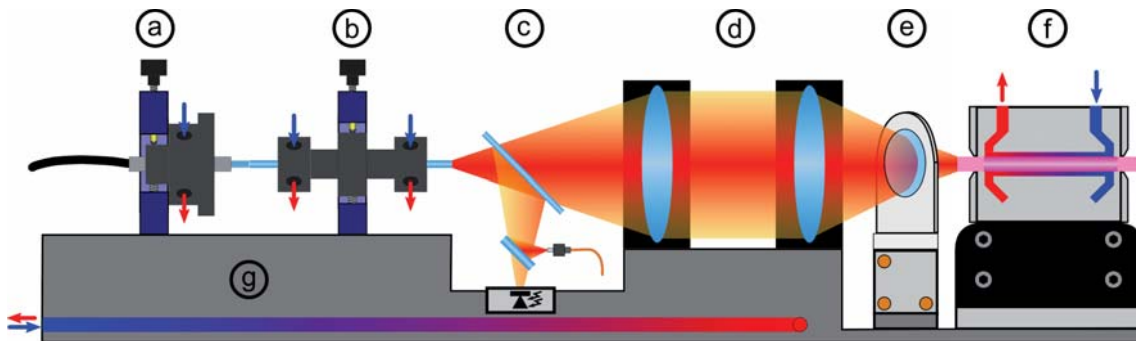

Figure 4.11: Optical setup of the laser head components: **a)** fiber bundle holder, **b)** homogenizer holder, **c)** pump light diagnostics for power and wavelength monitoring, **d)** pump light imaging optic, **e)** adjustable dichroic mirror, **f)** pump chamber with Nd:YAG crystal, and **g)** optical bench.

In fact, the pump light double pass configuration has its benefits for the thermal distribution within the laser crystal, but it is accompanied by a higher heat load on the mechanical structure of the laser head module. For the chosen laser crystal design specified in the *Conceptual Design Document* [Fre05a], 90% of the incident pump light can be absorbed in the Nd:YAG crystal for the given pump light distribution. As described in Section 3.1, the absorption efficiency is mainly influenced by the overlap of the pump light spectrum with the absorption spectrum of Nd:YAG. All non-absorbed pump power will exit the laser crystal through the entrance aperture and thus propagates in backward direction through the pump light optics again. As

the divergence of the pump light is altered during the propagation within the crystal rod, the light propagating backwards will not follow exactly the same optical path as in the forward direction. As a consequence, a major portion of the approximately 10% of the incident pump light will illuminate the mechanical components within the laser heads structure. In addition to the thermal loading of the opto-mechanical components by the non-absorbed pump light, losses at coated surfaces, resulting mainly in scattered stray beams, have to be taken into account. As heating of opto-mechanical mounts is one of the major causes for misalignment, a FEM analysis of the effects of the expected heat loads on the mechanical structure of the laser head was performed.

4.2.1   FEM heat load analysis

For the numerical FEM analysis with ANSYS the following heat loads for the mechanical and optical components of the laser head assembly were assumed:

Position at laser head	power losses	remaining power
Forward propagation of pump light		
Pump power at working point from fiber bundle tip (a)	0 W	250 W
Coupling losses at homogenizer illuminating the mounts tip (b)	5 W	245 W
Light deflected into pump light diagnostics by 45° AR window (R ≈ 1.2%) (c)	3 W	242 W
Dichroic mirror, 2.5% of power deflected + vignetting at mirror mount (e)	7 W	235 W
Vignetting of the pump light background at the pump chamber surface, PTFE o-ring and rod aperture, estimated with a beam propagation calculation (f)	10 W	225 W

Backward propagation of the non-absorbed pump light		
Dichroic mirror and mount	0.5 W	22.5 W
Vignetting at the pump light imaging optics mounts, estimated with a beam propagation calculation (d)	1 W	22 W
Light deflected upwards by 45° AR window	1 W	21 W
Homogenizer and mount front face (rest of pump light – light coupled into homogenizer, estimated with a beam propagation calculation)	15 W	20 W
Fiber bundle tip and mount (the portion of light coupled into the fibers is neglected)	5 W	0 W

Table 4.1: Estimated pump power losses and their corresponding components of the laser head assembly given in Fig. 4.11.

Consequently, an optical power of 47.5 W has to be discharged by the mechanical structure of one laser head during normal operation. In principle, this amount of power could be dumped into the mechanical structure of one laser head without causing damage to the components. However, as a consequence, all opto-mechanical mounts would be deformed and misaligned with changing pump power (especially during the powering up phase of the laser system). Additionally, the thermal load at the laser heads would heat up other components inside the high power oscillator housing. The most critical of these components is the base-plate of the high power slave, because it defines the absolute position of each internal optical mount. Furthermore, if the base-plate is expanded by the heating process, the length of the resonator will change as well.

To compensate for the heat loads at the laser head assembly, a water cooling circuit was included into the mechanical structure of all critical components. A detailed description of these sub-assemblies and their functionality within the laser head module will be given in the following sections. All water cooled components of a laser head are connected in series by reinforced silicone hoses with an inner diameter of 4 mm, whereas all four laser heads are connected in parallel to the designated water circuit. The water flow of each laser head cooling circuit is measured by a turbine flow sensor,

which is constantly monitored for leak detection. In Fig. 4.12 the results obtained by the FEM simulation of a laser head module with and without water cooling are given for comparison. During the simulation the water temperature was kept at a constant value of 18 °C for simplification of the thermal model. This assumption could be made, because the estimated temperature increase of the cooling water is only approximately 1 K. All optical power levels given in Table 4.1 were applied as heat loads to the designated surfaces of the mechanical model. Furthermore, a convective heat transfer to the laminar flowing air of the clean room (V = 0.5 m/s, see Appendix A) was taken into account. The environmental temperature was set to 24.5 °C to simulate the actual temperature inside a laser housing, which was determined in an experiment with a previous prototype laser. In addition, no indication for a heat accumulation inside the housing during normal operation was found. All interconnecting surfaces were treated to be joined (ANSYS standard configuration) and the corresponding material properties of the mechanical parts were set to the values given in Appendix A. No heat transfer into the base-plate of the high power oscillator could be incorporated into the simulation, as the maximum number of finite elements for the mechanical model was reached. However, due to the actively water cooled optical bench of the laser head an uncritical temperature near the coolant temperature is expected at the interconnecting surface to the laser's base-plate. For all following thermal FEM analysis of the laser head and its components the environmental parameters of the simulation were retained.
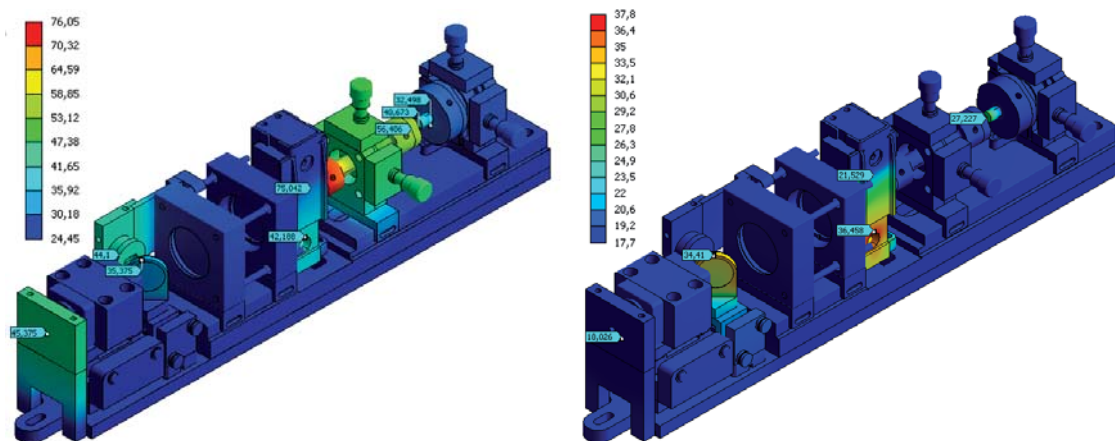

Figure 4.12: **Left:** Steady-state thermal FEM analysis of the laser head structure without active water cooling (maximum temperature ≈75°C). **Right:** Thermal FEM analysis of the laser head assembly with water cooling of all components (maximum temperature ≈75°C). The applied heat loads and their position at the laser head structure correspond to the ones given in Table 4.1.

The temperature values determined by the simulation where then taken and compared with thermal images of the laser structure at normal operational conditions. For this purpose, pictures with a thermal camera, type FLIR i60, of all critical components of the laser head were taken. During these measurements the laser was operated and the housing was opened on the side only. The flow rate for each laser head was set to 0.5 l/min and the cooling liquid temperature was chosen to be 18 °C. As most of the materials of the laser head assembly are sand blasted, the emission coefficient for the calibration of the thermal camera was set to 0.98, which is the camera internal parameter for rough surface metals. A comparison of the thermo optical pictures with the simulated data will be given in the following sections for the corresponding opto-mechanical components.

4.2.2 Pump source

The use of a semiconductor lasers working in an output power regime of several tens of watts always goes along with the need for high current power supplies. In this case, a total number of seven fiber coupled diode lasers with a maximum optical output power of 45 W each were chosen to pump a single laser head. The use of seven fiber coupled diode laser as pump source offers the following advantages:

- The seven attached multi-mode fibers can be incorporated in a bundle, which overall diameter (for a commercial 400 μm multi-mode fiber) stays below 2 mm,

- A maximum optical pump power of 315 W is achieved, which offers a safety margin to the required 250 W per laser crystal during normal operation. This pump power reserve can be either used for a derated operation of the diode lasers, which should increase their life-time, or to be able to compensate for faulty diode lasers by increasing the output power of the remaining operational ones.

As the high power oscillator comprises four Nd:YAG crystals, a total number of 28 diode lasers fabricated by the JENOPTIK AG (Model JOLD-45-CPXF-1L) are needed. These diodes have a minimum electrical to optical efficiency of approximately 40% and require currents up to 65 A at a maximum voltage of 2 V [Jen10]. Based on these numbers a total electrical power of 130 W per diode laser and a maximum of 3640 W for all diodes can be estimated. These numbers exclude the power consumption for the active temperature stabilization of the diode lasers.

The required pump currents can only be supplied by switching power supplies that have the major disadvantage of coupling frequency distortions into the line voltage.

In fact, four Delta Electronika power supplies (model SM 52–60) provide the power for each set of seven diode lasers connected in series. The line voltage distortions, produced by these power supplies, would then couple into all electronic measurement equipment used inside the GWD and hence into the detection signal. Thus, the use of switching power supplies at high power levels is strictly forbidden near the interferometer components.

At all LIGO sites the area containing the interferometer and thus the laser system is electrically shielded from the support building. To maintain this shield, all electronic equipment of the laser system, such as diode lasers and the necessary controllers, are located outside, approximately 100 m away from the laser table. From this point, the generated pump light is delivered via multi-mode fibers with a 400 μm core diameter to the high power oscillator. Seven of these are combined to a bundle protected by a flexible metal tube. At one end, the fibers are attached with SMA connectors to the diode laser modules and at the other end, the bare fibers are glued in a aluminum ferrule and polished to optical grade. A polished end-surface of one of these fiber bundles with a diameter of 1.4 mm can be seen in Fig. 4.13a.
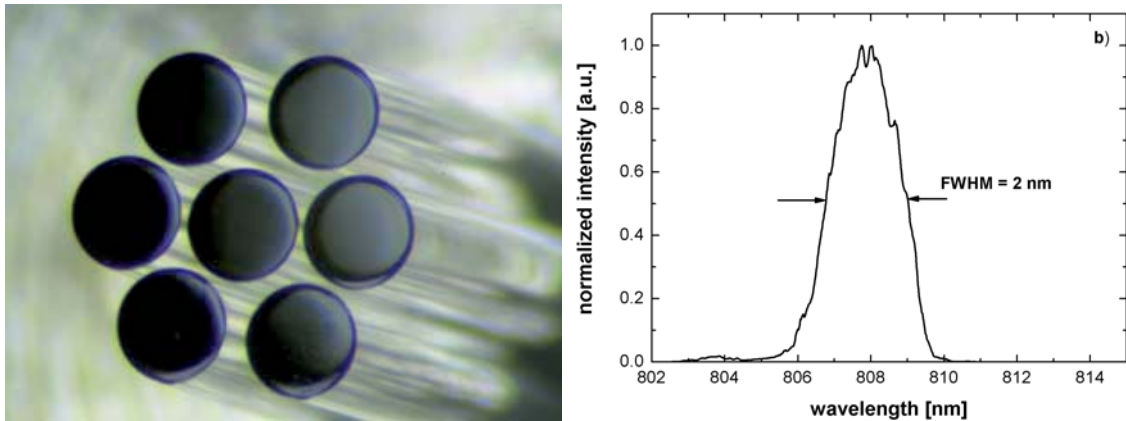

Figure 4.13: **a)**: Picture of the end tip of a polished fiber bundle taken with an overhead microscope. **b)**: Measured pump light spectrum after optimization of the spectral overlap of the emission of seven diode lasers.

On the SMA end of the fiber bundle, all laser diodes designated for the optical pumping of one laser head are assembled in a *laser diode box* (LDB). To use seven diode lasers as a pump source for one Nd:YAG crystal, the individual spectral power distributions of all seven diode lasers have to be tuned to form a combined pump light spectrum. As the central wavelength of each diode laser changes with a factor of approximately 0.3 nm/K it is possible to overlap the output spectrum of all seven diode lasers by temperature tuning (specified central wavelength: 807 nm -1 nm/+2 nm). For this purpose all the diode lasers are each equipped with two ther-

moelectric coolers (TEC) that actively transfer the heat generated during operation to a copper base-plate, which is an integral part of the semiconductor laser diode assembly. For heat removal out of the LDB, sets of 4 and 3 lasers diode are mounted onto water cooled copper heat sinks (see Fig. 4.14). The TECs are then connected to a temperature controller circuit board. The current needed to supply all circuit boards (one circuit board is connected to a maximum of four diodes) is provided by two separate Delta Electronika power supplies (model SM 52–60). The current for each diode laser's TEC pair is controlled by an input voltage signal ranging from 0–10 V. With this control setup the internal temperature at the laser diode bar, which is measured with a PT1000 sensor with a resolution of 0.01 K, can be set to a desired value.
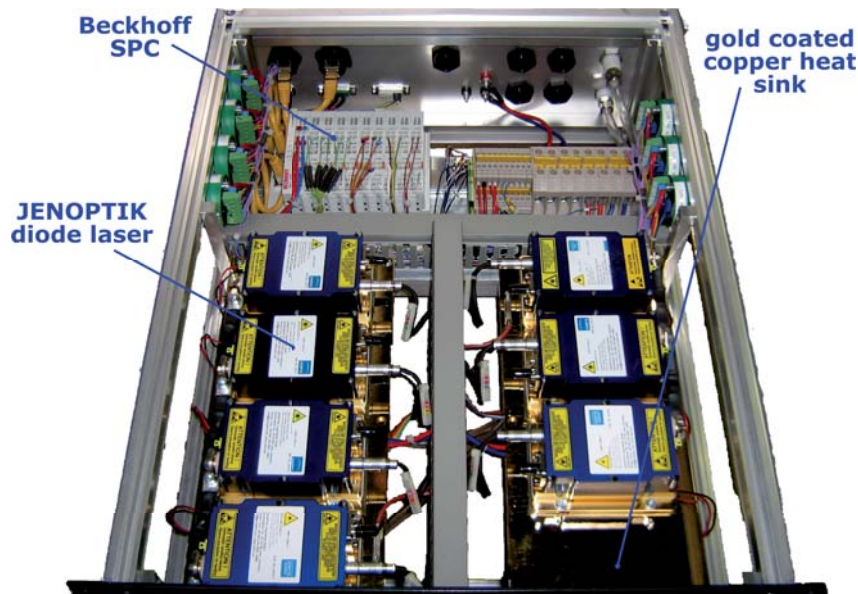

Figure 4.14: Picture of an assembled LDB. Top left: Beckhoff bus coupler plus attached Fieldbus cards. Bottom: JENOPTIK diode lasers attached to water cooled heat sinks.

For an automated active temperature stabilization of each single diode laser, a software controlled modular Stored Program Control (SPC) distributed by Beckhoff is used [Bec11]. These systems stand out from hardware SPC systems due to their very modular structure, based on an Ethernet ring topology for communication with all attached subsystems, and an easy programming interface. The communication between the subsystems over the Ethernet bus is established by bus couplers to which a broad variety of input and output terminals can be attached. In our case, a 12 bit D/A-output converter, providing 0–10 V per channel, is used to control the TEC current. The temperature of each diode is read out with a 16 bit A/D-converter,

which is calibrated for the attached PT1000 sensor. A software based PID controller processes the input/output variables to achieve a relative temperature stability of 30 mK [Gau03]. Manually setting the temperature of each diode laser in one LDB, it was possible to achieve a combined spectrum with a FWHM of 2–2.5 nm at a center wavelength of 808 nm. The installed diode lasers were specified to have a spectral width less than 3 nm. Typically, this type of diode lasers feature a FWHM below 2 nm. In Fig. 4.13b a typical pump light spectral distribution is shown.

When the laser is operated, approximately 5 W of pump light propagating in backward direction illuminate the tip of the aluminum ferrule (see Table 4.1). In addition, a second, more significant, source of heating, is located at the inside of the fiber bundle ferrule. Over the long propagation distance of 100 m, some fraction of the pump light leaks from the core of the fiber into the cladding. This effect, which converts the regular core modes into cladding modes, appears, when the fiber is coiled with a small bending radius. Thus, a small amount of modes can leak into the cladding and the protection coating of the fiber. At the fiber tip, the outer protective cladding is stripped off, which makes it possible for modes guided in this acrylate cladding to leave the fiber structure. For safety and cooling reasons, the point, where the outer cladding is removed is located within the aluminum ferrule. Additionally, the adhesive used to secure the seven fibers in their position is applied at the back of the the aluminum ferrule, because it would start to burn when illuminated by the backward propagating pump light.

No exact number for the optical power level absorbed inside the aluminum ferrule core could be derived, because these numbers strongly depend on the fabrication quality of the fiber bundle and the position and bending radii of the fibers. In experiments with previous prototypes, temperature levels for an uncooled fiber bundle above 80°C could be measured. These fiber bundle ferrules were made from polytetrafluorethylene (PTFE) or a machinable ceramic to withstand high temperatures. For these versions of the fiber bundle ferrules the high temperature levels had a negative effect on the glue fixing the fibers on the back, which started to outgas and soften. Both processes significantly shortened the life-time of the fiber bundle. If damage of the fiber bundle would occur, the 100 m long fibers would have to be pulled back to the laser diode boxes and be replaced by a spare. This is a time consuming process requiring a lot of manpower, which causes an unwanted downtime of the interferometer for several hours. Hence, methods to avoid a failure because of high temperature loads inside the ferrule had to be found.
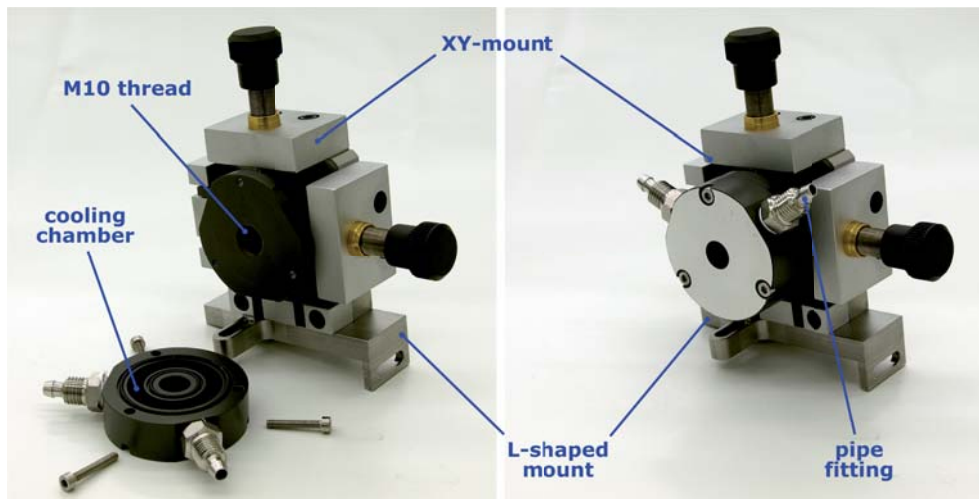
Figure 4.15: Opened and closed version of the fiber bundle mount built in a XY-positioning stage. The aluminum fiber bundle ferrule is screwed in from the back during laser head installation.

To remove the heat from the aluminum ferrule of the fiber bundle a water cooled fiber bundle mount was constructed. As shown in Fig. 4.15 a mount for the ferrule placed into an optical XY-positioning stage was designed. Within this mount, an M10 thread is used to screw in the fiber bundle for ease of replacement and to increase the area of contact. In a turning process a cooling chamber was machined into the cover plate of the fiber bundle mount, whose interconnecting surface holds two rubber o-rings for sealing. This top cover is then screwed tightly to the mount and water connectors were installed on top.

To reduce the weight and load for the springs inside the XY-positioning mount, aluminum was chosen as the preferred material for the fiber bundle mount. All aluminum parts directly in contact with the deionized cooling water were finished with a thin layer of hard-coating. More information on the appropriate choice of materials being in contact with cooling water will be given in Section 4.3.1.3. Underneath the XY-positioning mount an L-shaped adapter plate made of stainless steel was attached. This design, which is used to mount all optical components of the assembly to the optical bench, is fixed by one screw at the top and one screw on the side to the optical bench. Furthermore, the L-shaped mount together with the optical bench acts as a translation stage in the z-direction of the laser head for easier positioning along the optical axis. As seen from Fig. 4.16 the maximum simulated and measured temperatures at the fiber bundle tip stayed within a safe range below 30 °C.
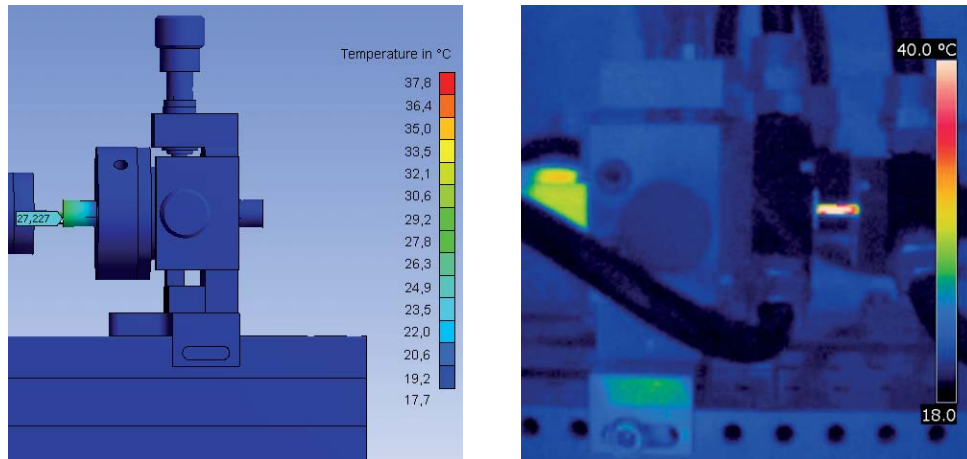
Figure 4.16: Highest simulated temperature at fiber bundle tip: 27.2 °C. Highest tempera-
ture determined with the thermal measurement at the fiber bundle tip: 26 °C.

4.2.3   Pump light delivery

As shown in the previous section the pump light is delivered by seven 400 μm
fibers directly to each laser head. A characteristic intensity pattern emerging from
the fiber bundle can be seen in Fig. 4.17 on the left. If this intensity distribution
would be directly used for longitudinal pumping of the laser crystal, a non-uniform
temperature distribution would be generated [Fre07a]. To compensate for these *hot
spots*, which are areas of higher pump light intensity and hence higher thermal load
inside the laser crystal, a 100 mm long glass rod with a diameter of 2 mm was placed
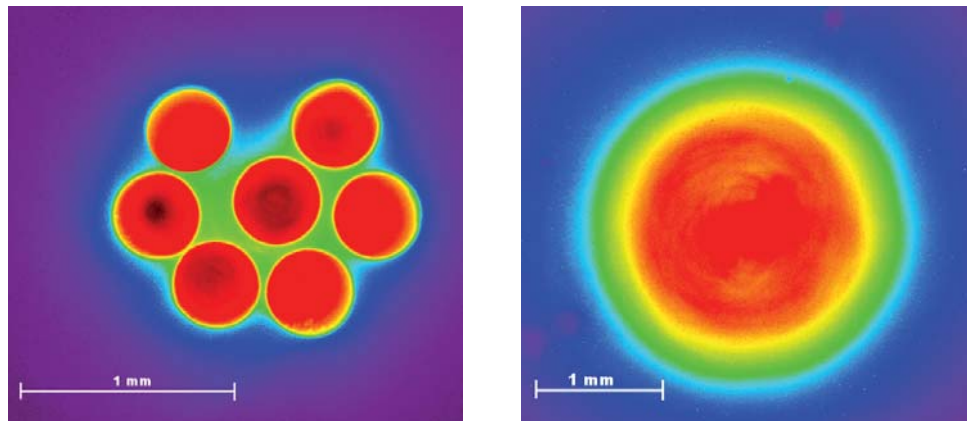behind the fiber bundle tip.

Figure 4.17: **Left:** Intensity distribution behind the fiber bundle. **Right:** Image of the
intensity profile after chaotic mode mixing with the homogenizer.

Total internal reflection inside the glass rod spatially mixes the overall pump light
distribution and results in a homogeneous distribution when it emerges from the rod.
The homogenized pump light pattern, which can be seen in Fig. 4.17 on the right
can be described by a Gaussian intensity distribution with a background. Because

of the spatial mixing effect on the pump light the glass rod is called a *homogenizer*. The use of a homogenizer for spatial pump light mixing does not only prevent *hot spots* inside the laser crystal, it increases the reliability of the high power oscillator. In fact, the mixing is not restricted to the use of seven laser diodes for pumping. It is also possible to homogenize the intensity distribution generated by only six active laser diodes attached to the fiber bundle [Gau03, Pun11]. Hence, if one diode laser fails during operation one can increase the output power of the remaining laser diodes in operation. With this scheme it is possible to keep the system operating until the laser can be taken offline for maintenance.

Similar to the fiber bundle assembly, the homogenizer is held in a dumb-bell shaped assembly and fixed within a XY-positioning stage. Two lathed, concentric cooling chambers are machined into the front face of the homogenizer mount, which are sealed with o-rings and a cover. The homogenizer itself is held into place by two PTFE o-rings at both ends. To keep the PTFE o-rings in their designated position (PTFE tends to flow plastically when heated) their axial position is well defined by the mechanical fit of the homogenizer mount and its cover. In Fig. 4.18 two pictures of the homogenizer structure are shown.
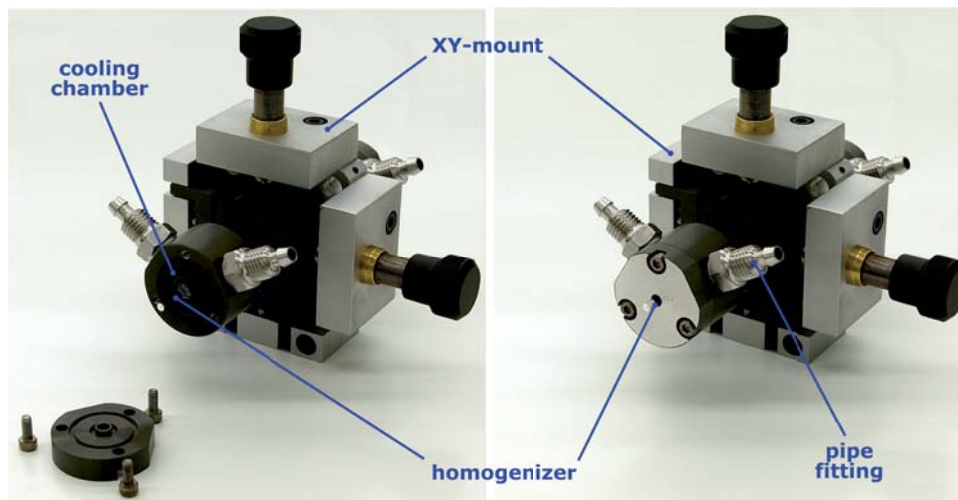

Figure 4.18: Homogenizer mount with frontal flow chamber opened and closed. The homogenizer rod is centered on the optical axis by 2×1 mm PTFE o-rings.

A light-weight, hard-coated aluminum was chosen as material for the homogenizer mount. To avoid contamination of the optical surfaces of the laser head internal optics by outgassed substances from the front and back face of the mount, it was covered during the coating process to provide a clean aluminum surface.
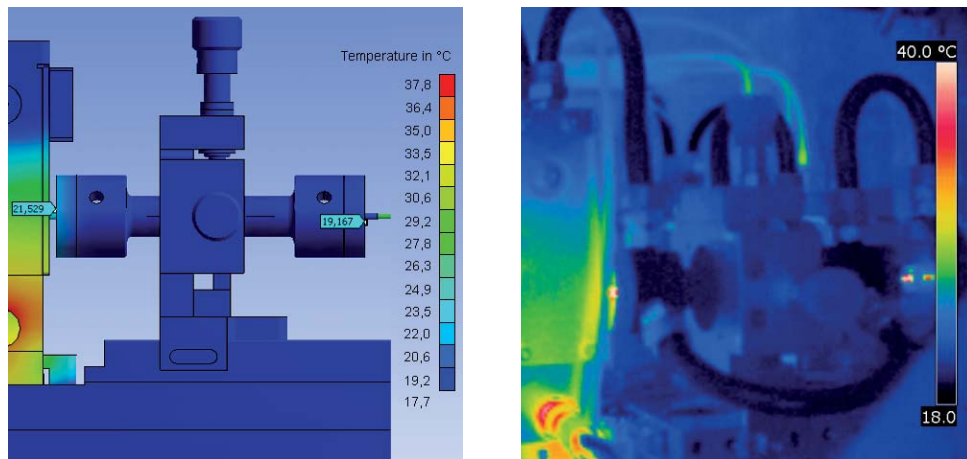
Figure 4.19: Highest simulated temperature at the homogenizer mount tip in direction of the pump chamber: 21.5 °C. Highest temperature determined with the thermal measurement at the homogenizer mount tip in direction of the pump chamber: 21.6 °C.

The given heat load values from Table 4.1 on page 75 indicate that most of the pump light propagating in backward direction is absorbed at the tip of the homogenizer mount (15 W). When not water cooled, the temperature of this mount would exceed 75°C (see Fig. 4.12). Images taken with a thermal camera, which are presented in Fig. 4.19, show a stable temperature level of 21.6°C in normal operation.

4.2.4 Pump light diagnostic

During constant long term operation of the diode lasers used for optical pumping of the laser system, a degradation of the semiconductor chip material is expected. A general indication for this process is a drop in output power for a given current. When this degenerative effect occurs, the difference in optical output power is directly transferred into heat inside the semiconductor lattice. The higher temperature of the laser diode chip material then alters the center wavelength, which is shifted by 0.3 nm per K. As a consequence, a constant monitoring of the pump light power and spectral distribution is necessary to be able to compensate for these aging processes.
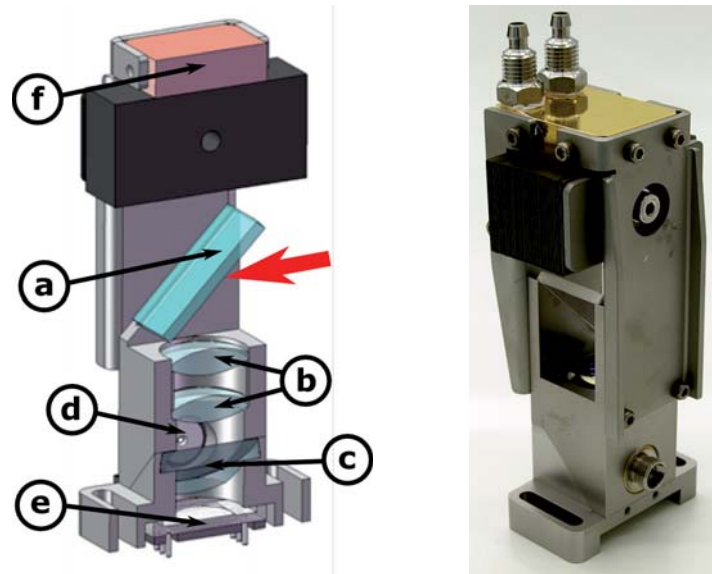
Figure 4.20: **Left:** 3D CAD section of the pump light diagnostic with AR coated window at 45° to the incident pump light (a), $f = 20$ mm lenses in a telescope configuration (b), 90% / 10% beam splitter for 45° angle of incidence (c), FC fiber connector (d), PSO FL-100 large area photodiode with coated glass substrate with R = 98% on top (e) and razor blade beam block mounted to a gold coated copper heat sink (f). **Right:** pump light diagnostic assembly.

For this purpose a pump light diagnostic assembly, shown in Fig. 4.20, is placed between homogenizer and pump light imaging optics. Inside this assembly a window (a) at 45°, which is coated with an anti-reflection coating with matched reflectivity values for the unpolarized 808 nm pump light, is included in the structure. A fraction, approximately 1 %, of the pump light is picked off by this window and imaged by two lenses in a telescope configuration (b) into the core of the assembly. This light is then split into a ratio of 90 % to 10 % by a 45° beam splitter (c). The high power beam is reflected from the beam splitter to a FC fiber connector (d), whereas the transmitted beam is imaged onto a Si-photodiode with an active area 10 mm in diameter (e), which is protected by a highly reflective coated glass substrate with a reflectivity of R=98 %. To block all backscattered light coming from the optical surfaces of the pump light diagnostic and to cool the assembly, a gold coated heat sink with a razor knife block was mounted on top of the mechanical structure. Actually, a stack of razor blades is a sufficient and cheap optical beam dump, because the light runs dead within the gap of two adjacent blade edges. In a typical configuration 120 razor blades with a thickness of 0.2 mm are stacked. The results of the thermal steady-state FEM analysis and the corresponding picture taken with the thermal camera of this laser head component can be found in Fig. 4.21.
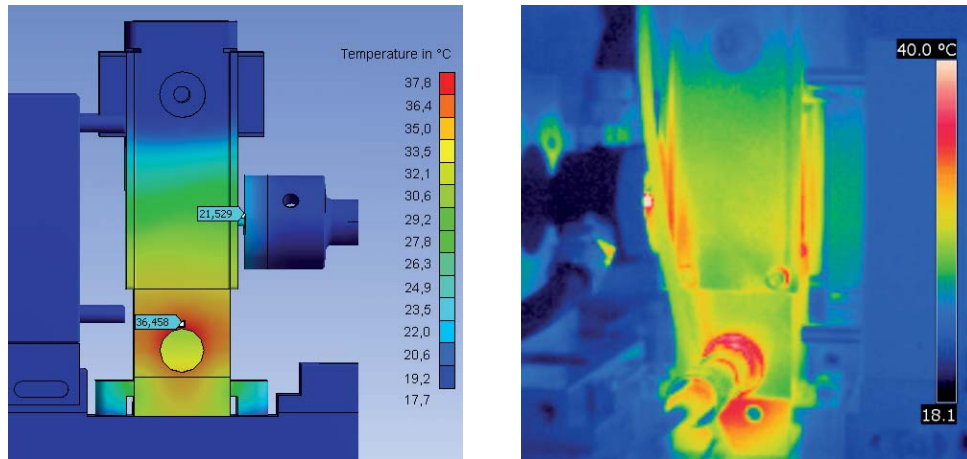
Figure 4.21: Highest simulated temperature at the fiber connector of the pump light diagnostics module: 36.5 °C. Highest temperature determined with the thermal measurement at the fiber connector of the pump light diagnostics module: 38.5 °C.

The current from the photodiode is converted into a voltage level by a transimpedance amplifier, whose output is amplified by an inverting operational amplifier circuit and sent to the SPC control for continuous monitoring. For a spectral analysis of the pump light, a 4×1 fiber optical switch is connected to all four FC connectors of the laser heads pump light diagnostics. When selected in the SPC program, the light of a specific pump light diagnostics port is transmitted through the output port of the fiber switch to a CCD grating spectrometer. With this spectrometer, fabricated by Ocean Optics (ype HR4000), online spectrum control and logging is possible. Triggered by an automated software, the switch periodically changes the diagnostic port under test and the FWHM and peak wavelength of the pump light is taken and stored every 10 minutes.

4.2.5   Imaging optics

In Fig. 4.22 the pump light radius with respect to the distance from the homogenizer tip is given. The values presented in this graph are derived by an ABCD matrix calculation for the pump light beam path, whose underlying principles were described in Section 3.2.2. Two assumptions were made for the calculation of the beam path of the divergent pump light. First, the numerical aperture (NA) of the homogenizer is identical with the one of the multi-mode fibers, which is NA = 0.22. With this value and the homogenizer rod radius of $w = 1$ mm the beam parameter product (bpp) can be calculated from $bpp = w \cdot \arcsin(\mathrm{NA})$. Inserting the derived value in following equation $M^2 = bpp \cdot \pi/808$ nm, the beam quality factor M^2 of the divergent pump

light beam was determined to be $M^2 = 862$. Secondly, even though the lenses have a thickness of 10 mm they were assumed as thin lenses for the calculation. In fact, this is only valid if the spacing between the principal planes of the lens is small compared with the propagation distance and the focal length is given for the pump light wavelength by the manufacturer.
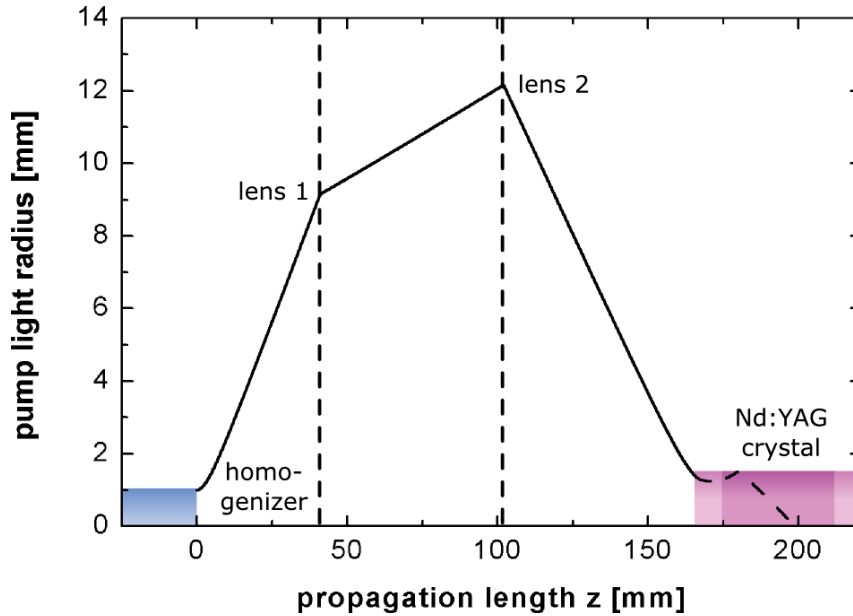

Figure 4.22: Estimated pump beam propagation through the two lens pump optics assembly. The lens positions were optimized for the highest output power of the oscillator setup. Solid line: radius of the pump light propagating in air. Dashed line: pump light propagation inside the Nd:YAG crystal.

The actual distances between homogenizer tip, lens No. 1, lens No. 2 and the Nd:YAG crystal were determined experimentally during tests with previous prototypes. A detailed investigation of the impact of the pump spot size on the output power and beam quality of a comparable laser setup is given in Ref. [Pun11].

For the pump light imaging optics biconvex lenses made of N-BK7 with a focal length of approximately 53 mm at a wavelength of 808 nm and a diameter of 40 mm were chosen. Both lenses are mounted in two static lens mounts, each with an edge length of 60 mm. In fact, this is the widest part of the optical setup mounted on the optical bench of the laser head. Thus, the width of the optical bench of a laser head was chosen to be 60 mm as well. Both lens mounts are connected by four stainless steel rods, which are used to fix the spacing. Additionally, the metal rods are used to attach the pump light beam block, which will be described in the following text.
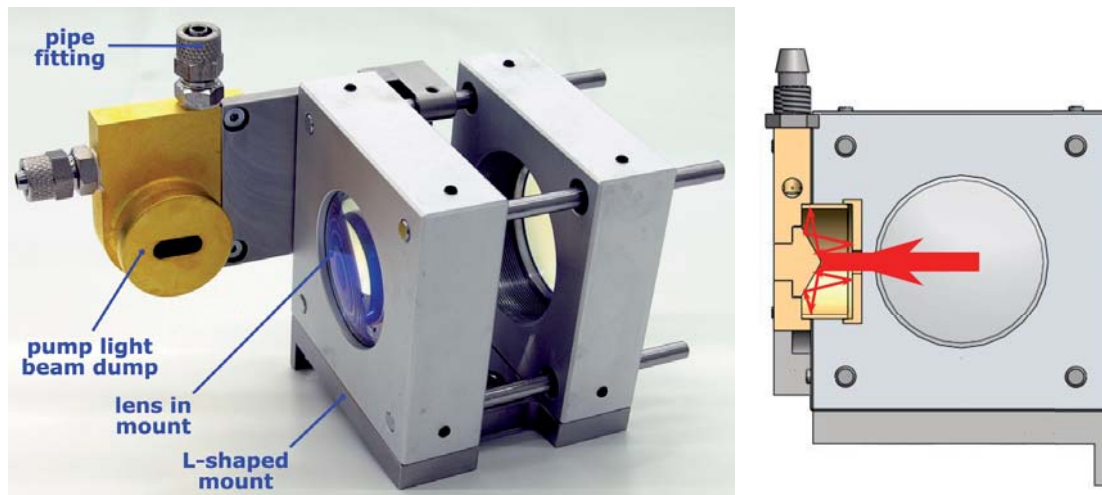
Figure 4.23: **Left:** Pump light imaging module with attached water cooled pump light beam block. The complete optical setup of the two lenses can be pre-aligned for all laser heads before assembly. **Right:** 3D CAD section of the pump light dump. The internal conical structure with an angle of 120° and the scattered rays of the pump light at the cone can be seen.

In Fig. 4.23 a picture of an assembled pump light imaging optics block can be seen. This block is used to dump the approximately 3 % of pump light, which is reflected by the coated surfaces of the dichroic mirror in front of the laser crystal, within a water cooled and gold coated copper heat sink. For horizontal alignment, the heat sink is mounted on an extension arm attached to the stainless steel rods between the lens mounts. To avoid back reflections coming from this beam dump, a conical structure as displayed in Fig. 4.23 on the right side was implemented into a surrounding housing with a slit as entrance aperture. The angle of the gold coated copper cone is set to 120° to eliminate backscattering through the housing aperture as be the result for a flat structure or a cone with 45°. The pump light, which is scattered at the gold coated cone, is directed into the housing of the dump, where the light is absorbed after several reflections at the beam blocks inner structure. When the laser crystal is pumped almost no scattered light from the aperture of the beam dump illuminates the mount of the dichroic mirror. In fact, this mechanical concept was used for all other high power beam dumps within the high power oscillator housing, because it offers sufficient supression of the backscattered light in combination with efficient heat removal.

4.2.6   Dichroic pump mirror

To separate the laser beam from the pump light incident on the rod's end facet, a dichroic mirror was placed at a 45° angle between pump light imaging optics and laser crystal. The full power of the pump light, which is focused down in front of the Nd:YAG rod, is transmitted through the 1 inch mirror. To keep the losses at the mirror's surfaces low, an anti-reflection coating for 808 nm and a dichroic coating, which is highly reflective for 1064 nm and highly transmissive for 808 nm, was applied.

During the development of the high power oscillator, specific requirements for the coating process and the thin film structure of the dichroic mirror turned out to be essential to achieve the required high output power levels. Optimizing the Ion Beam Sputtered (IBS) layer structure of the dichroic coating to the wavelength of the laser automatically increases the reflection losses for the unpolarized pump light. Estimates of and tests with various samples from various suppliers showed that the lowest achievable pump light reflection of the mirror was 2.4%. For an incident beam with a power of 250 W a total reflected power of 6 W had to be tolerated. To account for variations in the quality of the coating process, a maximum loss of 3 % in total for the pump wavelength around 808 nm was specified.

In addition to the tolerable loss specification for the pump light, requirements for the coating at the laser beam wavelength were specified as well. In fact, at non-normal angles of incidence, multi-layer coated mirrors have to be treated as two different mirrors, one for each polarization of the incident laser beam. The properties of each of this periodic reflectors are the one of a mirror at normal incidence, but with effective values of the refractive index for the corresponding polarization [Apf82]. As the phase thickness $\beta_i = 2\pi \cdot n_i \cdot d_i \cdot \cos\theta_i / \lambda$ depends on the effective refractive index of the corresponding i^{th} layer, the phase picked up by a vertically or horizontally polarized beam differs. Thus, a mirror with an unoptimized layer structure will act as a retarder plate for beams with a polarization deviating from the horizontal or vertical plane.

As described in Section 2.1, a linearly polarized output beam from the high power laser is required. The linear state of polarization of the high power oscillator is obtained by a window inserted at Brewster's angle into the cavity (see Section 4.1.1 for more details). If the orientation of the polarized light inside the cavity is not perfectly matched to the vertical or horizontal plane of the non-optimized dichroic mirror (e.g. because of non-compensated depolarization of the beam), the reflected beam from this mirror would encounter a phase retardation. A fraction of this light, which is not horizontally polarized, is reflected at the Brewster plate. The higher

the phase shift of the installed mirrors, the worse the depolarization is compensated, and the higher the resonator internal losses at the Brewster plate will occur.

To counter this loss mechanism, the multi-layer structure of the dichroic mirrors had to be optimized by the coating manufacturers to impart a phase shift of less than 4° (lowest value guaranteed by any coating manufacturer) between vertical and horizontal polarized light at an angle of incidence of 45°. However, the only reference for the phase shift of the final coated mirrors offered by the manufacturer was a backward calculation from the thickness of the layers applied to the mirror substrate.
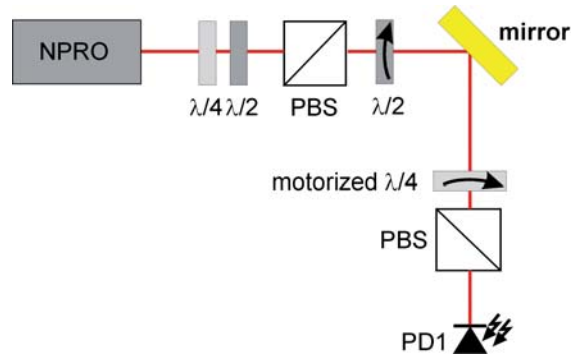

Figure 4.24: Polarimeter setup to analyze the effect of the dichroic coating on the laser beam polarization. The probe beam was linearly polarized using half- and quarter-wave-plate and polarizing beam splitter.

For the verification of the 4° retardance specification for all dichroic mirrors, a test setup shown in Fig. 4.24 was constructed. This setup consists of a linearly polarized NPRO beam, whose polarization angle with respect to the principal plane of the mirror under test can be rotated manually by a half-wave-plate. The beam is reflected by this dichroic mirror and then sent into an automated polarimeter. This polarimeter is based on a rotating quarter-wave-plate and a polarizing beam splitter cube. From the transmitted signal through the beam splitter cube, which is detected by an InGaAs photodetector, a characteristic signal for different incident states of polarization could be measured. For mirrors with a phase shift of 0° the measured signal at the photodetector does not depend on the incident polarization angle. For a mirror with phase shift, a deviation from the expected sinusoidal signal is obtained. Sample signals for two dichroic mirrors with a phase retardance of 0° (a) and 30° (b) are given in Fig. 4.25.
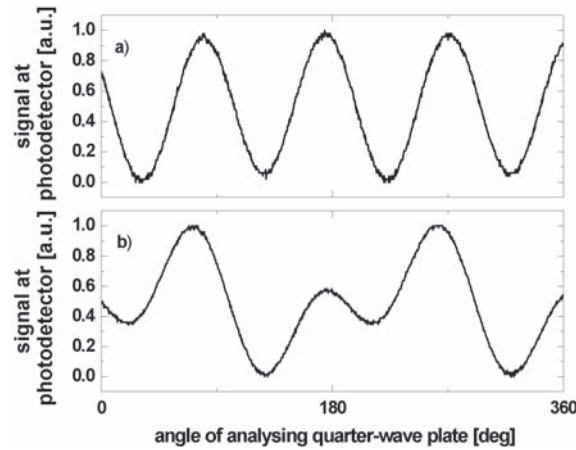
Figure 4.25: Normalized photodetector signal for different angular positions of the motorized quarter-wave plate. **a):** Mirror with 0° phase shift. **b):** Mirror with 30° phase shift.

Fitting the function $I(\omega t) = \frac{1}{2}[A - B\sin(2\omega t) + C\cos(4\omega t) + D\sin(4\omega t)]$ to the measured sinusoidal signal, the fit parameters A, B, C, and D are determined. With these parameters, the components S_0–S_3 of the Stokes vector defining the state of polarization of light can be calculated with [Gol03]:

$$
\begin{aligned}
S_0 &= A - C, \\
S_1 &= 2C, \\
S_2 &= 2D, \\
S_3 &= B,
\end{aligned}
$$

where S_0 defines the overall intensity of the detected beam, S_1 the intensity fraction in linear polarization (positive = horizontal, negative = vertical), S_2 the intensity fraction of the 45° polarized light (positive = +45°, negative = −45°), and S_3 the intensity fraction of the circularly polarized light (positive = left-hand circularly polarized, negative = right-hand circularly polarized). With the resulting Stokes vector, the deviation from the linearly polarized probe beam can be determined and compared with the results generated by a mirror with 4° phase shift as fulfillment criteria for the coating specification.

During the development of the Advanced LIGO laser system, it turned out that the dichroic mirror in front of the laser crystal cooling chamber is one of the parts, which is most sensitive for thermal misalignment. Small thermally induced angular shifts of this component cause a significant misalignment of the laser beam, resulting in a reduced output power of the high power oscillator. Unfortunately, it is not possible to directly cool the mirror frame and its tip-tilt mount with water, because the flowing

water would introduce mechanical vibrations into the assembly. The generated micro movements of the mirror mount would directly couple into the laser output noise, which is already a limiting factor of high power laser systems for GWDs.
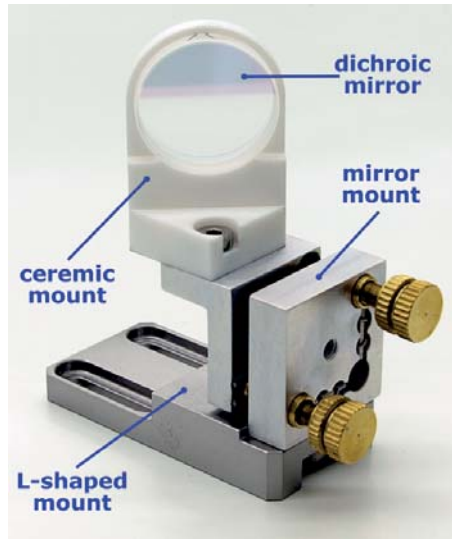

Figure 4.26: Dichroic mirror mounted in MACOR frame on tip-tilt mirror mount.

To keep the influence of the stray light – either from the spontaneous emission coming from the crystal end-facet (estimate: ≈ 2 W absorbed at the mirror mount's surface from the total 5 W of fluorescence) or from the pump light clipped at the mirrors aperture (estimate: ≈ 1 W) low, a ceramic mount was developed to hold the dichroic mirror in place. A machinable ceramic material with the trade name MACOR is used for this component, see Fig. 4.26. Not only is the coefficient of expansion of this material is fairly low, it is also semi-transparent for wavelengths in the near infrared regime. Thus, the absorption of this material, whose thickness is kept rather thin at points of incident light, is very low compared to stainless steel, aluminum and gold coated copper (a table of the mechanical and optical properties of MACOR can be found in Appendix A). A second advantage is that the ceramic material has a low heat conductivity. Consequently, the generated heat is not transferred from the mirror frame to the aluminum tip-tilt mount, but only removed by convection of the surrounding air. Thus, this mount is very stable and insensitive to temperature changes of the dichroic mirror (see Fig. 4.27).

The mirror is fixed to the ceramic by a viscous adhesive (Corning DC 93 500) inside the ceramic frame. This adhesive is sturdy enough to fix the mirror in position during transportation of the laser to the USA, but ensures that it can be easily removed to replace the optic in the case of a failure.
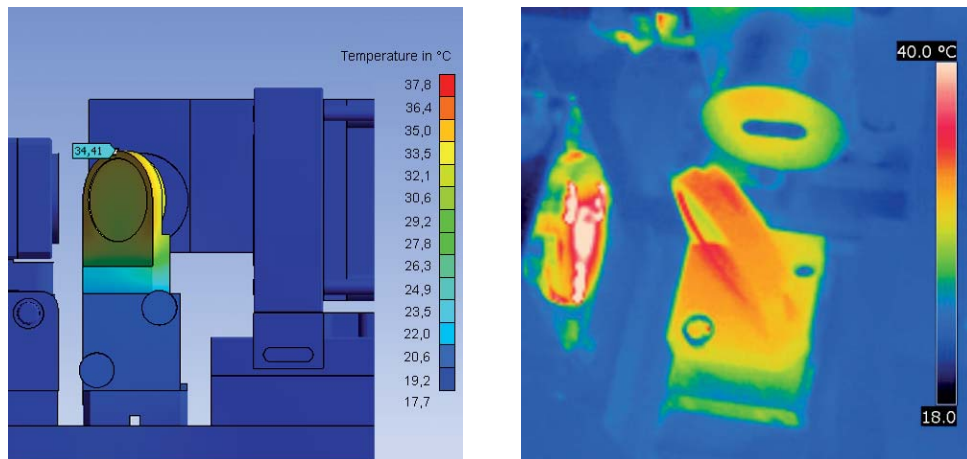
Figure 4.27: Highest simulated temperature at the top of the MACOR dichroic mirror frame: 34.4 °C. Highest temperature determined with the thermal measurement at the top of the MACOR dichroic mirror frame: 34 °C.

4.2.7 Laser crystal cooling chamber

The shape, dimension, and doping concentration of the Nd:YAG rod used inside the laser head setup has the most influence on the laser performance. In the experiments done by Frede et al. for the first prototype of the Advanced LIGO laser [Fre04, Fre05a, Fre07a], a 0.1 at.% doped Nd:YAG crystal in a pump light double passes configuration turned out to be the best available choice for a fundamental mode laser. Nevertheless, an ongoing optimization of the design of Nd:YAG crystal rods for end-pumped fundamental mode lasers was carried out by Puncken [Pun11]. Even though different crystal designs, e.g. multi-segmented crystal rods, core-doped ceramic Nd:YAG crystals, and laser crystals with a longitudinal parabolic doping concentration were tested [Wil08], the above mentioned original and simplest design still proved suitable for the type of laser presented in this work.

When being installed in the laser head structure, the crystal is mounted inside a water cooling chamber. In this cooling chamber the barrel of the laser crystal is cooled by a turbulent jet of water for efficient heat removal. Besides the good heat removal abilities of the direct water cooling, the refractive index difference between the water ($n_w = 1.33$) and the Nd:YAG material ($n_{\text{Nd:YAG}} = 1.82$) provides a pump light guidance inside the laser rod due to total internal reflection. In fact, the cooling chamber is the most complex mechanical part of the laser head assembly. Even though the mechanical design for the laser system presented in this work is finalized, the optimization and further development of the cooling chamber design is an ongoing process for various other laser applications and systems.

In general, the performance of a water cooled solid-state laser mainly relies on the thermal lens inside the crystal and thus on the performance of the laser crystal cooling. In Section 3.1, it was shown that the heat transfer coefficient, which mainly influences the amount of heat dissipated from the rod barrel into the cooling liquid, can be optimized by the appropriate choice of the water's velocity and hence turbulence. The higher the velocity inside the flow chamber the more turbulent the water flows and consequently the more heat is removed from the surface of the laser rod. To obtain an axial temperature distribution, which is more homogeneous, the amount of heat that is dissipated from the rod barrel into the water can be modeled. Usually, the design of the flow tube surrounding the crystal is optimized for a constant heat transfer coefficient over the full length of the rod. In in Fig. 4.28 on the left hand side a section of the original pump chamber design with a straight flow tube is presented. A computational fluid dynamics (CFD) simulation carried out with ANSYS showed that it was advantageous to increase the water's velocity from the rear to the front of the laser crystal rod. This leads to a changing heat transfer coefficient with laser crystal length. In this design, the highest heat transfer coefficient is reached near the position of the highest heat load, whereas the lowest heat transfer coefficient is located at the point of the lowest temperature of the laser crystal.

Figure 4.28: **Left:** Previous pump chamber design with straight flow tube. **Right:** Improved pump chamber design with conical flow tube and indirect flow chamber. In both cases the pump light is injected from the left and the water flows from blue to red.

As shown in Fig. 4.28 on the right hand side, a conical flow tube is used to increase the water's velocity along the crystal cylinder.In this concept, the cooling water was

injected in the opposite direction of the incident pump light. Entering the flow chamber from the side with the larger radius, the water is accelerated by the reduction in diameter of this flow tube and ejected from the crystal cooling chamber again. To reduce the mechanical coupling of noise into the laser crystal by the incoming jets of water, a so called flow chamber was grooved into the pump chamber in a turning process. Within this flow chamber, the water with a high flow rate is evenly dispersed before it enters the conical flow tube. For symmetry reasons, a second flow chamber is located at the end of the cooling chamber as well. The crystal itself is then fixed and sealed by two PTFE o-rings, which are pressed into a counter bore by a metal end cap. This method of sealing proved feasible for high flow rates up to 5 l/min and high pressures up to 8 bar.
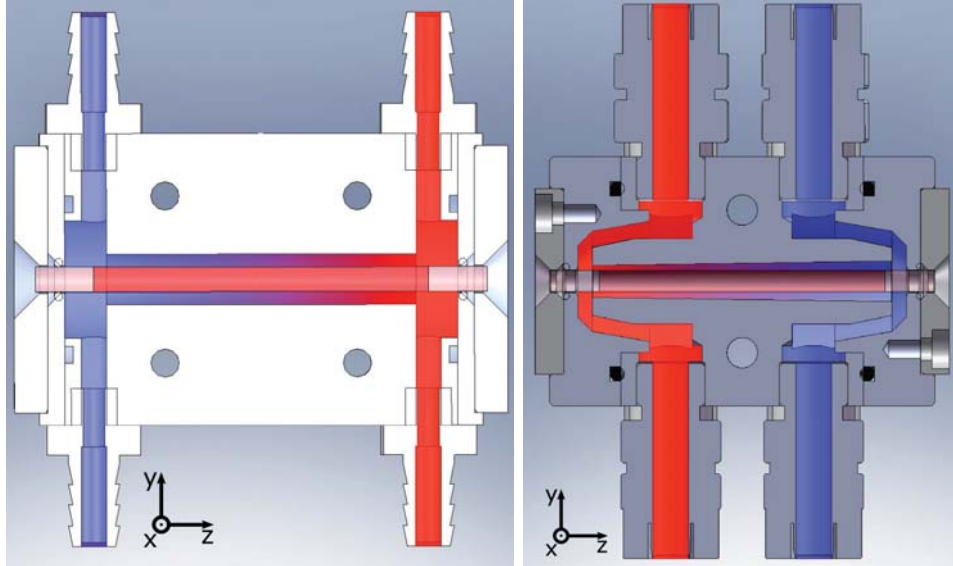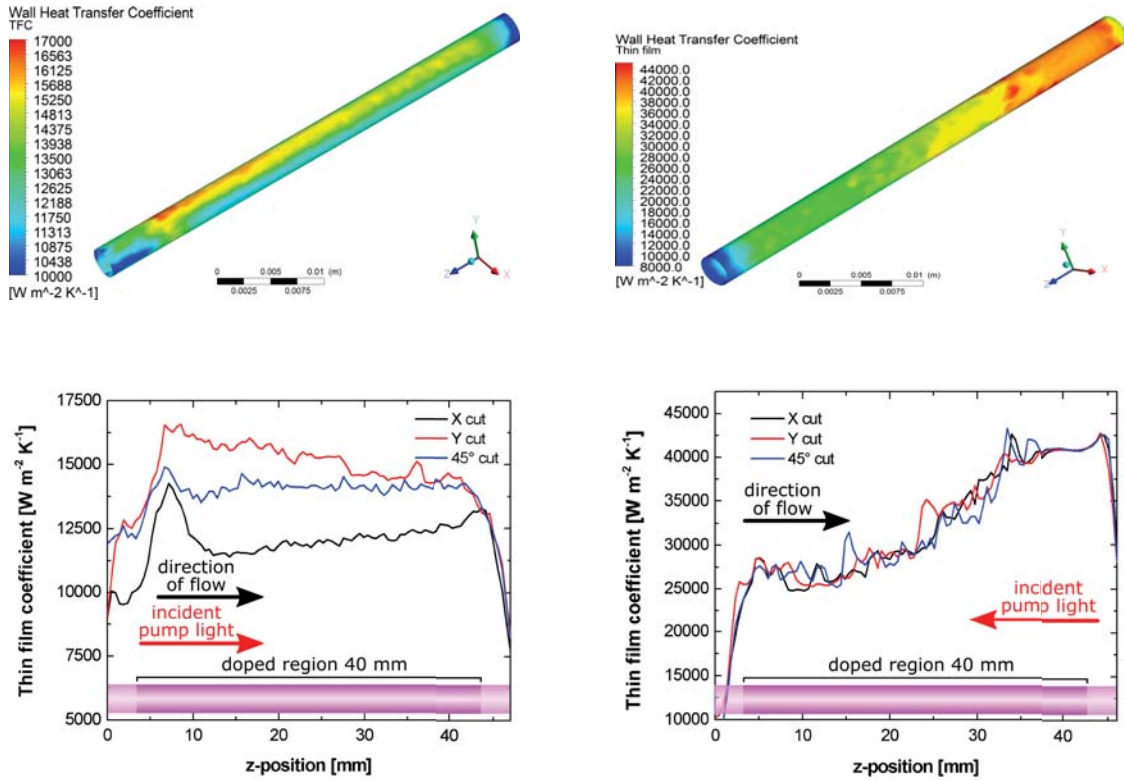

Figure 4.29: **Left:** Pump chamber design with straight flow tube. **Right:** Improved pump chamber design with conical flow tube and indirect flow chamber. The *x cut* illustrates the heat transfer coefficient along a line at the cylinder of the crystal located at the x-plane. The *y cut* and *45° cut* correspond to lines at positions on the cylinder surface in the y-plane and at a plane tilted by 45°, respectively. In Fig. 4.28 a coordinate cross is given, which defines the orientation of the mechanical models of the pump chamber.

In Fig. 4.29, a comparison of the results obtained by the CFD analysis of the previously used (Fig. 4.28 left) and the new pump chamber design (Fig. 4.28 right) are

presented. For this analysis the water inlet pressure at the pump chambers was set to 4 bar, the water temperature was 18 °C and a standard surface roughness given by ANSYS was assumed. It can be observed that the new pump chamber design increases the average heat transfer coefficient over the crystal cylinder by nearly a factor of 2.5, because of a higher velocity and thus a more turbulent flow of the cooling water. But, not only the overall heat transfer coefficient was optimized by the new design, the uniformity of the heat transfer coefficient around the crystal surface also benefits from the improved design.

The better uniformity of the distribution for the new chamber design is directly visible in the calculated colored thermal maps of the wall heat transfer coefficient in Fig. 4.29 on top. When mounted into the original cooling chamber, the heat of the pumped laser crystal is removed more efficiently on top of the barrel than at the sides. This effect could lead to an elliptical shape of the thermal lens inside the pumped laser crystal. By comparison, the slope of the heat transfer coefficient for the new pump chamber design is equal at different radial positions along the crystal barrel. Thus, a more uniform thermal lens profile is expected.

Equipped with the optimized pump chamber design, the four head ring oscillator setup showed a decreased focal length of the thermal lenses of approximately 5% compared to an identical laser setup with the originally used pump chambers. These values were also verified using the FEM and Rod Designer analysis methods. As described in Section 4.1.2, a lower thermal lens shifts the operation point to higher pump power levels per crystal. Thus, either the absorbed pump power at the working point and consequently also the output power of the high power oscillator is increased, or the resonator can be adapted to the new thermal lens. In this case, the reduced thermal lenses resulted in a necessary length increase of the short arm by 20 mm, which relaxed the requirements on the mechanical construction for the short arm distance range.

As published by Kugler et al. in Ref. [Kug97], the efficiency of an optical birefringence compensation is strongly affected by the alignment of the opposing laser crystals. To be able to align two adjacent laser cooling chambers of the high power oscillator to each other, a four axis tip-tilt mount was applied to the bottom of the pump chamber structure. Those four axis mounts, which can be seen on the picture of the complete assembly in Fig. 4.30, are held in place by four screws from the bottom of the laser head ground plate. With a low power seed beam as reference, it was possible to align both opposing laser crystals on the same optical axis.

At the end of the laser head structure, between pump chamber and the XY-mount for the first lens of the depolarization compensation, a water cooled aperture is

placed. This aperture is included into the setup to block the approximately 5 W of spontaneous emission (fluorescence) coming from the crystal tip. The structure, which can be seen at the left side in Fig. 4.10 is made of gold coated copper and is fixed by a mount to the end of the laser head base-plate (for more details on materials in contact with the cooling water see Section 4.3.1.3).
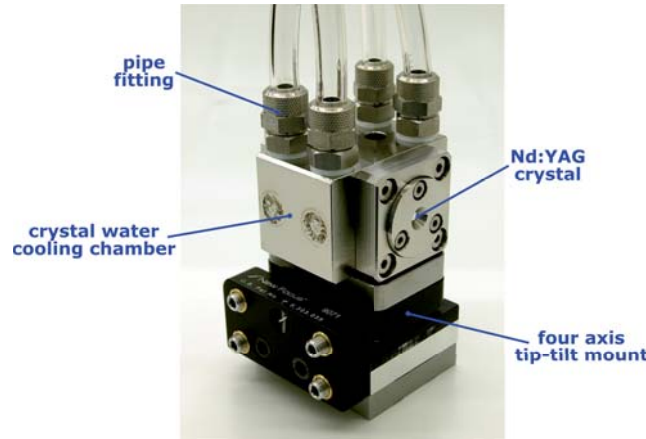

Figure 4.30: Pump chamber mounted on a four axis positioning table. The Nd:YAG crystal can be seen inside the counterbore of the cover plate for the pump chamber.

4.3   High power oscillator setup

For single frequency operation of the full laser system the 35 W amplifier beam will be seeded into the high power oscillator. As mentioned previously, a piezo actuated mirror (PZT) was already included as part of the cavity of the high power ring laser to provide a length control of the resonator needed for the Pound-Drever-Hall injection locking. In addition, the optical hardware of the 35 W MOPA had to be isolated from the backward propagating light of the free running high power oscillator when being not locked.

In Fig. 4.31, the complete optical setup of the Advanced LIGO high power oscillator is shown. It can be seen that the light emitted in direction of the 35 W amplifier is passing a high power Faraday isolator (HPFI). A picture of the fully assembled HPFI is presented in Fig. 4.32. When being locked, the laser power inside the optical elements of the Faraday isolator is decreased from approximately 120 W (backward propagating light plus 35 W amplifier) to the power of the amplifier only. Even though the absorption inside the optical elements of the Faraday isolator at a wavelength of 1064 nm is rather low, a changing thermal distribution, i.e. a changing thermal lens power, within these elements can be observed. As a result, the optical setup of the high power Faraday isolator contains a compensation for thermal
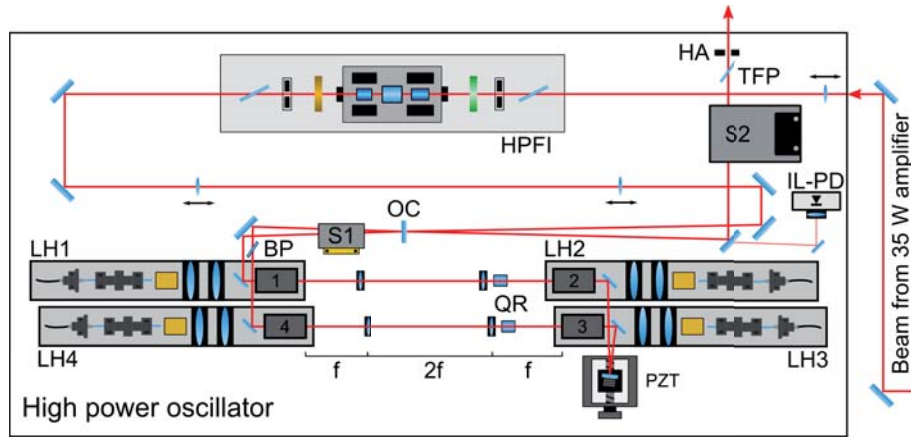
Figure 4.31: Schematic setup of the injection-locked high power laser system with: laser head 1 – 4 as described in Fig. 4.11 (LH1–4), output coupling mirror (OC), piezo actuated mirror with linear stage (PZT), 90° quartz rotator (QR), high power Faraday isolator (HPFI), injection-locking photo diode (IL-PD), shutter 1 and 2 (S1, S2), thin film polarizer (TFP), Brewster plate (BP), and halo aperture (HA).

lensing and depolarization invented by Khazanov et al. [Kha04]. For an increased attenuation ratio of the Faraday isolator, naturally birefringent calcite wedges were combined with high power thin film polarizers. With this setup, an attenuation of the backward propagating light of more than 35 dB was achieved for various power levels up to 120 W.
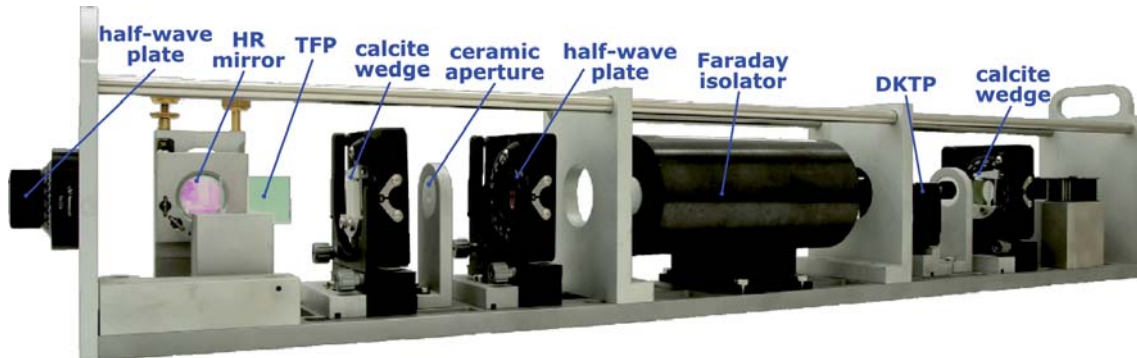
Figure 4.32: Picture of the fully assembled Faraday isolator module.

Additional optical elements, which are essential for the operation of the laser, are the photodetector for the heterodyne detection of the injection locking signals (IL-PD), a thin film polarizer (TFP) to filter the remaining portion of unpolarized light not reflected at the Brewster plate (BP) inside the resonator and a so called *halo aperture* (HA), which will be described in the experimental results Section 5 in greater detail.

4.3.1 Water cooling scheme

For the complete high power laser one has to distinguish between two different types of heat loads that occur at different locations. The first source for heat generation is the absorption of laser light (pump and solid-state laser light alike) inside the active media, at the mechanical structure or at the position of the power detectors and beam dumps. In fact, the amount of heat, which is generated within these elements, is fairly low and can be easily dissipated by water cooling. However, the combination of different metals with optical components, e.g. Nd:YAG rods, stainless steel cooling chambers etc., made the design of a practical cooling scheme more challenging. Furthermore, the laser performance of the high power oscillator strongly benefits from the quick removal of the heat generated inside the laser crystal rods, which determines the requirements for a minimum flow rate of the cooling loop.

The second heat source is located in the laser diode room. All the diode lasers for optical pumping of the 35 W amplifier and the high power oscillator transform only a fraction of the electrical energy into light. This fraction, which strongly depends on the diode lasers temperature, output power and age of the semiconductor chip material, is approximately 40%. As described in Section 4.2.2, the temperature of each diode laser is controlled by a set of thermoelectric coolers. The TECs add additional heat due to their limited energy transfer efficiency, which is proportional to their supply current, which has to be taken into account for sizing of the cooling circuit.

In the following sections the two different cooling circuits for the Advanced LIGO high power laser are described. Furthermore, guidelines for the selection of materials directly in contact with the cooling water to maintain its purity are presented.

4.3.1.1 Laser cooling circuit

Both stages of the high power laser system for Advanced LIGO, the 35 W amplifier and the high power oscillator, are connected to the same water cooling loop. The deionized cooling water, with a temperature of 18°C, is supplied by a water-to-air chiller (Termotek AG) with a maximum cooling capacity of 1.7 kW. Because of its high electric power consumption and its potentially vibration inducing cooling concept based on an internal compressor for temperature control, the chiller itself is located outside of the laser internal interferometer structure near the diode laser rack. The water is run from the diode enclosure to the optical table through LXT pipes with a total length of approximately 200 m for the supply and return pipe, which have an inner diameter of 1".
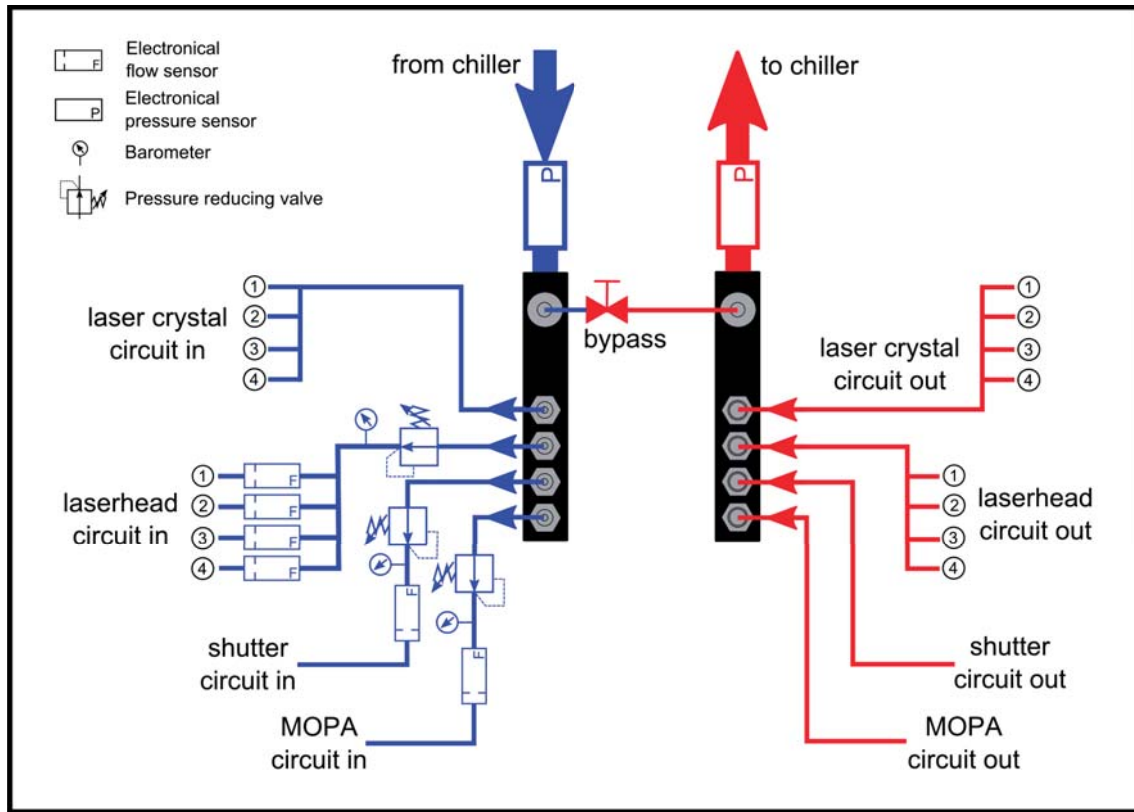
Figure 4.33: Water circuit diagram of the four parallel cooling loops connected to the crystal water manifold.

After the water is pumped through the 100 m long supply pipe to the optical table it is split up into four parallel water subcircuits. In Fig. 4.33, a schematic of the different water loops is presented. Three of these water circuits are equipped with a constant pressure regulator to control the flow rate. The fourth circuit, which is connected to the Nd:YAG crystals inside the high power oscillator, is designed to support the remaining water flow without a significant pressure drop. The left hand side of Fig. 4.34 shows the water manifold for the laser cooling circuit.

All four pump chambers inside the high power oscillator are connected in parallel to the high flow rate loop of the water manifold. When operated at the working point, each laser crystal of the high power oscillator is optically pumped with approximately 250 W. The pump power loss in front of the pump chamber after a pass through all optical elements of the laser head setup was 10 %. Inside the laser crystal 90 % of the incident pump light is absorbed in a double pass. Only a small fraction, approximately 45 W, of the remaining $\approx$ 190 W is converted into laser output power. The rest, approximately 145 W, is converted into spontaneous emission and heat inside the laser crystal rod. With these values, a maximum total heat load of approximately 700 W coming from the Nd:YAG crystals, which has to be dissipated by the cooling water, was estimated for the worst case scenario.
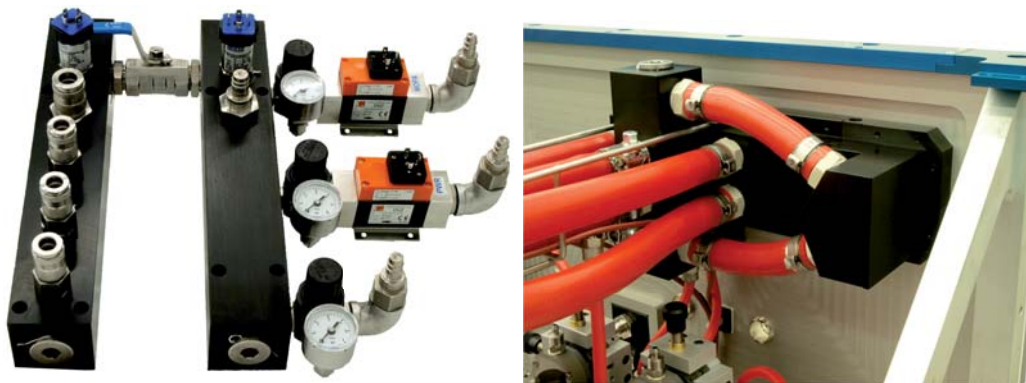
Figure 4.34: **Left:** Water manifold to supply and regulate the parallel water circuits of the high power laser. **Right:** High power oscillator internal water distributor for crystal and laser head cooling water.

To reduce the temperature of the Nd:YAG crystals to the desired level and preserve the rod from thermally induced fracture, the flow rate through the pump chambers had to be kept above 2.5 l/min per crystal. Additionally, the thermal lens can be reduced by a higher water flow rate, which increases the applicable pump power level at the operation point.

In addition to the cooling circuit for the laser crystals, the four laser head modules are connected to a water distribution unit, whose picture can be seen in Fig. 4.34 on the right. This distributor is mounted inside the laser housing and has an interface to the main water manifold located outside of the laser box. The laser head and the laser crystal cooling circuits are connected to this internal distribution unit by keyed stainless steel connectors with different sizes. All hoses running from this point to the cooling chambers and the laser heads are located on top of the laser structure to keep the space surrounding the laser resonator unblocked for easy access to the adjustments of all optical mounts. As described earlier in Section 4.2.1, the flow through the cooled subcomponents of each laser head, which are connected in series, are monitored by turbine flow sensors for each individual laser head. The four laser head circuits are then connected in parallel to the internal water manifold and the flow is set to 0.5 l/min for each loop.

The third water loop is connected to the power meters and beam dumps inside the laser housing. The flow rate for this circuit is set to approximately 1.5 l/min for all the components, which are connected in series. At the interface from the laser interior to the outside of the high power oscillator box, a water interface box made of polyoxymethylene (POM) was mounted to the structure. Stainless steel connectors

with matching sizes to the corresponding pairs at the water manifold were attached to this box. To prevent the accidental connection of the high flow / high pressure laser crystal cooling circuit to one of the other cooling loops, connectors with a larger diameter were used.

Finally, the fourth loop is connected to the 35 W MOPA system. The requirements for this system specify a flow rate above 1 l/min. To compensate for minor flow variations of the cooling liquid, the water throughput for this circuit was set to approximately 1.5 l/min. During operation of the MOPA system in the Enhanced LIGO science phase, this flow rate proved to be suitable for long-term operation.

The total heat load dissipated during operation by the four water cooling circuits for the high power laser system was estimated to be a maximum value of 1300 W. Due to a maximum cooling capacity of 1.7 kW of the water-to-air chiller, a safety margin of 400 W was kept to compensate for a degradation in performance of the chiller's internal compressor and pump. The minimum required flow rate to operate the laser is 15 l/min (4 x 2.5 l/min + 4 x 0.5 l/min + 2 x 1.5 l/min) for the complete cooling circuit. To have enough safety margin for the long term operation, the flow rate was specified to be more than 16 l/min during first installation of each laser system. One has to keep in mind that the fairly long 1 inch pipes of 200 m add an additional pressure drop of approximately 1.5 bar to the one of the Advanced LIGO laser. Thus, the pump of the chiller was specified to produce sufficient pressure and flow at the needed supply pipe pressure of approximately 5.5 bar. To control the chiller from the laser area, a RS232 communication interface was implemented into the SPC control electronics.

4.3.1.2   Diode laser cooling circuit

The water coming from the diode laser chiller is split up at a manifold connected to the four LDBs and the amplifier diode box in parallel. Additionally, a small portion of the cooling water is picked up in parallel directly after the chiller and is sent through 2 x 100 m long pipes with a diameter of 3/4" to the optical table but not the laser system itself. The flow rate of this additional water line is set to approximately 3 – 5 l/min by a constant pressure regulator. It will be used for cooling of thermopile power meters and beam dumps, which are integrated in various optical setups on top of the optical table.

Inside each LDB the water is pumped through two gold coated copper heat sinks that are connected in series, which dissipate the heat from the actively temperature controlled laser diodes. In total, the thermal heat load of a single diode laser operated with maximum output power and low set temperatures for the stabilization

is approximately 150 W. Thus, the maximum heat load of the complete setup is 4.8 kW for a worst case scenario. In fact, in normal operation, these power levels have never been reached. However, the cooling capacity of the chiller was chosen to be 5 kW, to provide a sufficient safety margin. The chiller, which is also fabricated by the Termotek AG and is based on a water-to-air cooling concept, comes with the same pump as the laser cooling chiller. Additionally, both chillers are built into one 19" rack, to consume less space within the laser diode room.

4.3.1.3 Materials in contact with water

In experiments with previous prototypes it turned out that the right choice and combination of materials within the water cooling circuits is essential for the lifetime of the laser system. Standard chillers for the cooling of laser systems require deionized (DI) water of high purity. In normal tap water the major impurities are dissolved salts, which are removed by specially-manufactured ion exchange resins to remove these mineral ions. This deionized water shows a similar purity for mineral contaminations as distilled water, but organic and virus particles are not removed by the filtering process.

The removal of salts from the water has the positive benefit that the cooling circuit is not contaminated by calcification. Unfortunately, specific metals inside the water cooling circuit will react with the DI-water by dissolving ions. One of the materials that cannot be used with direct contact to the water is copper. As soon as a component with copper or any other copper alloy is used, the water purity is drastically reduced. Additionally to this effect, which could be compensated by constantly deionizing the water, the copper corrodes and the water circuit will start leaking during long term operation.

Because of its high thermal conductivity of 385 $\frac{W}{m \cdot K}$, copper is the preferred material to dissipate heat quickly from a location with a high heat load. Thus, all heat sinks inside the high power laser and diode boxes are made of copper, but with a thin coating layer of gold applied to them. With this technique, the corroding effect of the DI-water was eliminated. During several years of operation of different laser systems it turned out that most of the forgeable alloys of aluminum contaminate DI-water as well. If no alternative material to replace aluminum can be implemented (e.g. if the weight is critical and heat has to be dissipated quickly from a surface illuminated by laser light), a special coating technique is used. During this coating process, the outer layer structure of the aluminum part is hardened by an anodic oxidation in a cooled acid electrolyte (commercial name is Hard-Coat). This thick and dense aluminum oxide layer has very good dielectric properties and does not react with the DI-water any more.

A third material group, whose compounds and alloys had to be evaluated during the development of the mechanical setup, included all stainless steel components. The major criteria for the selection of one specific type of stainless steel was the coefficient of expansion. It will be shown in Section 4.3.4 that a material with an expansion coefficient of $10.6 \times 10^{-6} \frac{1}{K}$ was desired. In addition to this criteria, the stainless steel has to be free of molybdenum, as it dissolves into the DI-water. Unfortunately, the dissolved molybdenum tends to coat the outer barrel of the laser crystal. This layer, when applied onto the interface between Nd:YAG and water, disturbs the pump light guiding effect and hence increases the losses for the pump light.

In general, materials that can be used inside all water cooling loops are plastics and silicones, which are specified for the use with purified water (e.g. POM = polyoxymethylene and soft PU = polyurethane). But, one has to keep in mind that these materials can not be used at points where they can be opposed to laser light, as they cannot tolerate high temperatures and burn.

4.3.2 Piezo actuated mirror

As described in Section 4.1.3, the resonance frequency of the high power oscillator is adjusted by a fast piezo actuator for the injection locking. This piezo has a dynamic range of approximately 5.5 μm at 375 V of driving voltage and a ring structure with a inner diameter of 8 mm, an outer diameter of 16 mm and a length of 10 mm (PI Ceramic model P–016.10H). As shown in Fig. 4.7 the piezo mirror is used to reflect the beam coming from laser head No. 2 in direction of laser head No. 3. For a good control of the resonator's alignment, the PZT was fixed on a tip-tilt mount. Even though a very heavy and rigid mirror mount was used, mechanical vibrations from the piezo's fast movement can couple into its structure, causing beam pointing and output power fluctuations. To reduce this coupling mechanism to a minimum, two different measures have been taken.

At first the mass of the coated mirror substrate, which is glued to the piezo ring actuator, was optimized to reduce the force applied to mirror mount when moving. From the equation $F(t) = m \cdot a(t) = m \cdot \ddot{s}(t)$ one can easily see that the force applied on the mechanical structure is directly proportional to the mass of the mirror's substrate. The best compromise between optical surface quality and light weight was found with a 0.5" diameter mirror with a thickness of two millimeters. A thinner substrates would further reduce the mass, but would be more sensitive to bulging during the optical coating process. Because of the piezo's dimensions, the diameter of the mirror itself could not be reduced further, otherwise it would not have been possible to glue the substrate to the ring piezo structure.

Secondly, an exact copy of the ring piezo including an uncoated substrate was fixed on the opposite side of the mount, as seen in Fig. 4.35. Both PZTs are connected in parallel with the high-voltage driver of the Pound-Drever-Hall locking electronics. If a change in position of the PZT mirror is required, the voltage of both piezos is altered. Hence, the other PZT is moving at the same time in the opposite direction. The forces applied by the moving piezo actuators on the mirror mount oppose each other and reduce the micro movement of the mechanical construction.
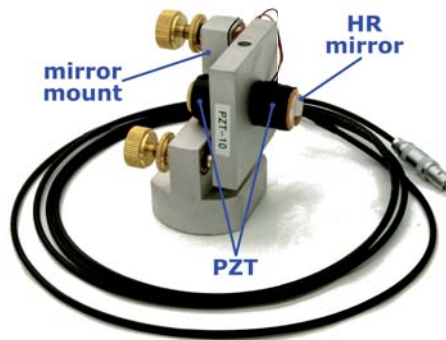

Figure 4.35: PZT mirror mount with ring piezos and substrates glued on opposite sites of the mirror mount base-plate.

To characterize the performance and damping of the fully assembled PZT mirror mount, the response to different excitation frequencies was analyzed. For a first bulk characterization and acceptance test of the hand made PZT mirror, an electronic impedance transfer function was measured. If the measured performance of the PZT mirror is acceptable, i.e. if the resonance frequencies of the piezo are in a good agreement with the manufacturer's value ($\approx$ 30kHz for the first resonance) and no additional features are visible in the characterization measurement, a second optical test is performed. Both test methods will be described in the following sections.

Impedance transfer function

For piezoelectric elements, the electrical impedance is a distinguishing characteristic. It differs substantially from the impedance of non-piezoelectric dielectric elements, when supply voltages with high-enough oscillation frequencies are applied. The difference stems from the coupling of electrical energy input into mechanical motion output. Recall that the electrical impedance is defined as the voltage drop across an element divided by the current through the element. By applying a sweeping sinusoidal voltage to the PZT assembly, the electrical impedance over a given frequency range can be derived. The magnitude of the impedance transfer function of the PZT mirror is shown in Fig. 4.36.
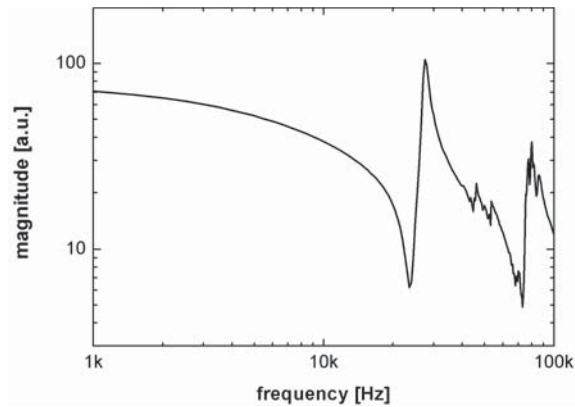
Figure 4.36: Impedance transfer function measured with a HP 4395A impedance analyzer.

A unique feature of the piezoelectric impedance is the existence of a Stokes/anti-Stokes response at specific resonance frequencies. The resonances result from the electrical input signal exciting a mechanical eigenfrequency of the piezo element. For each mechanical resonance of the PZT mirror, a resonance/anti-resonance pair does exist in the impedance transfer function.

To compensate for the mechanical and electrical resonances of the piezo, an electrical band-gap or so called notch filter is installed inside the Pound-Drever-Hall injection locking electronics. With the impedance transfer function in hand, it is possible to determine the eigenfrequencies of the piezo mirror directly after the assembly. In principal, a tuning of the notch filters inside the injection-locking electronics can be prepared before installation in the laser setup. Unfortunately, the HP 4395A with its attached impedance kit does not have a sufficient resolution at frequencies below 100 kHz. Thus, a second test to verify the exact frequency values of the resonance of the piezo mirror assembly had to be performed.

Optical transfer function

For this test, a simple and small Michelson interferometer was set up. A 2 W NPRO, which was attenuated to a few mW, was used as light source for the interferometer. The output power of the laser at a wavelength of 1064 nm was split by a beam splitter cube with a ratio of 50% to 50%. One of the high reflecting end mirrors in the perpendicular arms was replaced by the assembled PZT mirror. The interference of the two beams, after recombination at the beam splitter, was detected with a InGaAs photodetector. With a simplified locking scheme the interferometer was locked to mid-fringe.
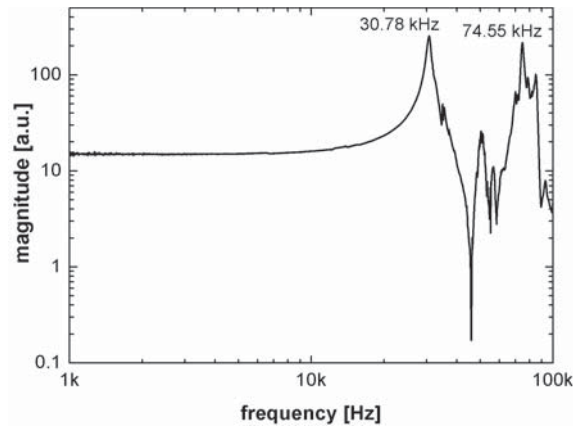
Figure 4.37: Optical transfer function of the same injection locking piezo in a Michelson interferometer test setup, measured with a Stanford SR785 network analyzer.

To derive the optical transfer function of the PZT mirror, a sweeping sinusoidal voltage was added to the HV-driver's output signal. The amplitude of the added voltage signal was set in a way that the interferometer stayed in lock over the full frequency range. For the specific PZT mirror, whose optical transfer function is presented in Fig. 4.37, the notch filters inside the injection locking electronic were adjusted to suppress oscillations of the high-voltage output at frequencies of 30.8 kHz and 74.5 kHz. With this measure, coupling of resonance frequencies into the injection-locked output beam of the laser system can be reduced.

4.3.3 Laser housing, base-plate and internal components

From the optical scheme of the high power oscillator presented in Section 4.3 (Fig. 4.31), it can be seen that various additional subcomponents beside the laser heads had to be integrated into one complete mechanical setup. To be able to transport the pre-assembled laser system to the location of the LIGO observatories, a rigid base-plate and a dust sealed housing with a footprint of 1.35 m to 0.75 m were developed. A picture with all necessary components of the high power laser installed can be seen in Fig. 4.38.

When injection-locked, the length of the resonator cavity will be adapted by a piezo actuator as describe above. The overall length variations of the high power oscillators cavity have to be kept within the actuator range at any time. If the range of the piezo actuator (approximately 5.5 μm) is exceeded, a loss of injection-lock can be observed. Even though this loss of injection-lock will be compensated within milliseconds by the locking electronics, the power inside the Fabry-Perot cavities of the LIGO interferometer will slightly drop, which causes a change of the radiation

pressure on the free falling mirror substrates that can not be compensated. As an outcome, the Michelson interferometer looses lock and has to be brought back into the locked state following a complicated and time consuming procedure.
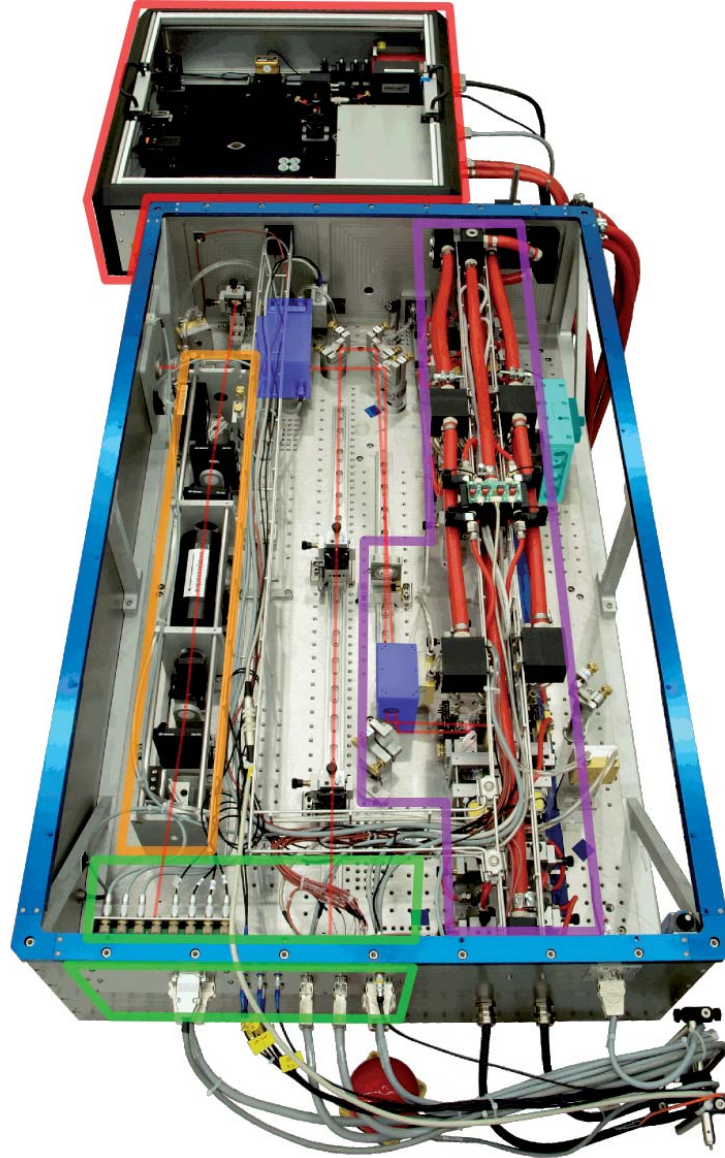
Figure 4.38: Fully assembled high power laser for Advanced LIGO (picture of the first observatory prototype) with, **purple**: four head oscillator ring cavity, **cyan**: element for active control of the resonator length (see next section for details), **orange**: high power Faraday isolator, **blue**: safety shutters, **green**: electrical interface, and **red**: 35 W amplifier. Additionally, the beam path on the baseplate is shown as a red line within the high power oscillator housing.

The fully assembled high power oscillator has a resonator length of approximately 1.85 m. In order to fulfill the requirements given in Section 2.1, two different measures were taken to stabilize the mechanical structure related to a thermally induced length

variation. To eliminate bulging of the mechanical structure due to materials with different thermal coefficients of expansion, all materials used during the construction of the laser heads, the base-plate, and all additional components were chosen to have the same expansion coefficient if possible. As a second measure, a slow actuator with a large dynamic range to compensate for the remaining expansion of the resonator structure was incorporated into the laser setup.

In a first step, three possible choices of materials for the high power oscillator base-plate were evaluated: aluminum, a low expansion steel called INVAR, and stainless steel. From these three materials, aluminum offers the best heat conductivity, can be easily processed, has a low weight, and is cost effective. Unfortunately, it has the highest expansion coefficient of $23.4 \times 10^{-6} 1/\mathrm{K}$ (high-tensile aluminum alloy given in Appendix A). For an environmental temperature change of 3 K, as specified for the high power laser during operation, an expansion of approximately 130 μm for the resonator length would occur. To compensate for this length variation of the resonator without impact on the internal beam alignment is almost impossible. Furthermore, the expansion of the aluminum base-plate is more than a factor of two higher than the optical table, whose expansion coefficient is $10.6 \times 10^{-6} 1/\mathrm{K}$ for 1.4016 stainless steel. To fix the position of the laser system with respect to the 35 W amplifier, the base-plate is fastened by several screws on the optical table. Thus, the difference in the coefficients of expansion would lead to a deformation of the material with the lower stiffness, which in this case is aluminum. A deformation of the base-plate would directly couple into the angular position of the mounts for optical alignment, which would then lead to a temperature dependent misalignment of the optical system. Hence, another material configuration had to be found.

As the second material combination, a nickel-iron low expansion alloy, called INVAR (see the Appendix A for more details), was evaluated. INVAR, which was used during the construction of the GEO600 laser system [Zaw02], has a very low thermal coefficient of expansion of $1.3 \times 10^{-6} 1/\mathrm{K}$ at room temperature. In principle, INVAR is the ideal material, because the resonator built on top of the base-plate would only expand by $\approx 7\mu$m for a total temperature change of 3 K. Unfortunately, INVAR has two drawbacks, which makes it unsuitable as base-plate material. First, INVAR is rarely produced in sizes required for the base-plate of the Advanced LIGO laser. Thus, several plates would have to be welded together, which introduces thermal stress into the structure. In fact, welding INVAR is a fairly complicated process. Second, the coefficient of expansion of the optical table is more than a factor of 8 higher than that of INVAR. As a consequence, a free floating support structure would have to be designed to allow the optical table to expand without deformation

by the stiff base-plate. The first development approaches of an isostatic mounting showed that it is infeasible to keep the position of the entrance window fixed to the 35 W amplifier beam in combination with an immovable position during alignment and an almost frictionless free floating bearing concept. Thus, the idea of using INVAR, which additionally would be very expensive, was abandoned.

The third and final solution involved a base-plate made of stainless steel, whose expansion coefficient is matched to that of the optical table. From various types of stainless steel, the alloys with the numbers 1.4021, 1.4313 and the one of the optical table itself 1.4016 were chosen (see the Appendix A for more details). All of these alloys have the same expansion coefficient as the optical table of $10.6 \times 10^{-6} 1/K$ and are available as large plate stock. Using expansion matched stainless steel for the base-plate, the resonator will expand by approximately 60 μm for an environmental temperature change of 3 K. Because the optical table and the laser system itself will expand by the same length, no bulging of the lasers base-plate and thus no misalignment of the internal optics is expected. As shown in the following section, the expansion of the stainless steel base-plate can be fully compensated with a slow actuator added to the optical resonator configuration.

4.3.4   Active resonator expansion compensation

Although the mechanical structure of the high power oscillator is water cooled, the equilibrium temperature of the complete laser box depends on the surrounding temperature level. Not only thermally induced length variations of the laser's base-plate and the optical components couple into the approximately 1.85 m long resonator. The refractive index of the air inside the laser box changes with both atmospheric pressure and humidity. This also leads to a change of resonator length. All effects are of the order of several tens of micrometers (linear expansion coefficient for air depending on temperature: 19 μm/°C, atmospheric pressure: 0.45 μm/hPa and temperature induced pressure change: -1.4 μm/°C [Edl66, Pec72, Bir93, Bir94]) that can not be compensated by the piezo actuator.

In order to compensate for the length variations induced by temperature and pressure changes the mirror mount carrying the piezo actuator was attached to a slowly moving linear stage with a DC motor (see Fig. 4.39). This stage is able to move with a maximum resolution of a few nm and has very smooth movement and high mechanical stiffness (Physical Instruments model M126-DG1).

This so called long range actuator (LRA) is controlled via the SPC system. When the piezo driving voltage exceeds a specific upper or lower limit, the LRA performs a predefined slow step to bring the piezo actuator in its neutral position at approximately
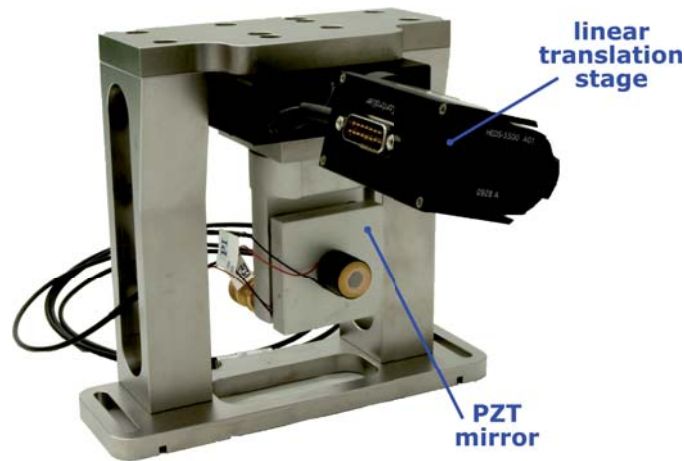
Figure 4.39: Long range actuator (LRA) stage with linear DC-stage and attached PZT mirror.

180 V. The length of one step can be set inside the software control and is determined experimentally and set to $\approx 2~\mu$m. The step duration is set to 2 seconds. This slow movement is then simultaneously compensated by an identical movement in the opposite direction of the piezo and does not interfere with the injection-locking (see Fig. 4.40 c) and d), as all contributing frequency components in the LRA movement are several orders of magnitude below the piezo control loop unity gain frequency. With this scheme not only the thermal expansion but also the atmospheric pressure induced distortions of the resonator length can be compensated by the combined action of the LRA and the piezo actuator. In Fig. 4.40a and Fig. 4.40b the actual room and laser internal temperature during a test run with a duration of 40 h is shown. During this long term temperature stress test, the laser was successfully operated without any loss of injection-lock despite a room temperature change of about 2.5 K.

4.3.5 Monitoring and safety

When operated to take scientific data, no personnel are allowed to enter the laser area enclosure inside the Advanced LIGO interferometer. Thus, all operational parameters of the running laser system have to be transmitted to a control room via the laser control computer. To be able to perform remote maintenance from the control room, various temperatures, voltages, currents, and environmental data regarding the operation of the laser system are transferred and stored by the SPC. More than 250 diagnostic channels were included into the control program of the high power laser, whose data is constantly saved to a hard disc drive and made available to authorized personnel.
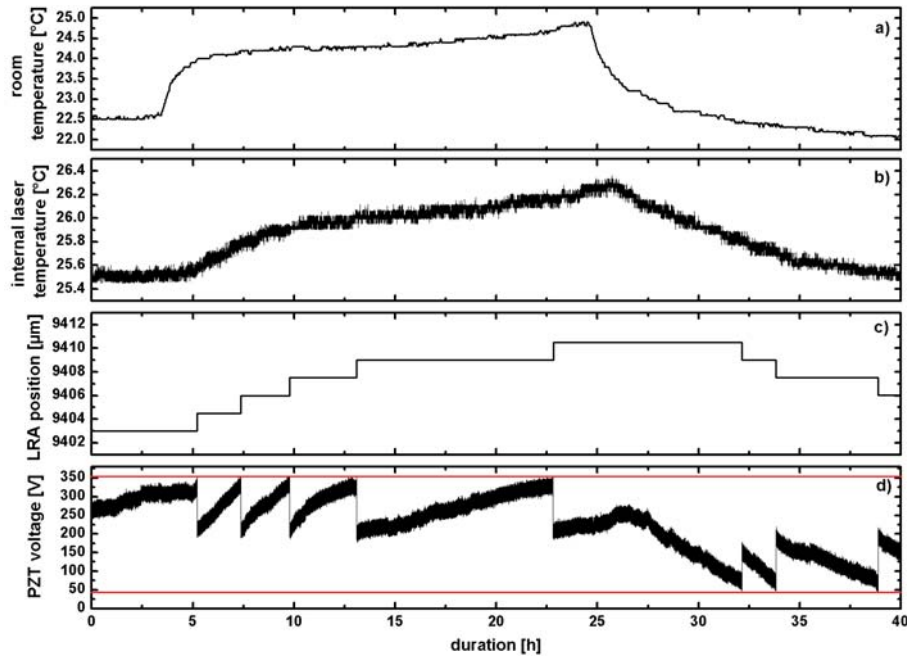
Figure 4.40: Induced room temperature change to test the LRA performance. **a)** room temperature measured above optical table, **b)** temperature inside laser housing with laser in thermal equilibrium, **c)** position of long range actuator and **d)** driving voltage for resonator internal piezo mirror.

For an emergency shut down and for convenience during the alignment process, two safety shutters were included into the optical setup of the high power oscillator. The first shutter S1, whose position is given in Fig. 4.31, is located inside the four head ring resonator beam path between the output coupler and the 45° turning mirror in front of laser head No. 1. When closed, a 45° high reflective mirror, which is mounted on a rotary solenoid, flips into the laser beam. The light coming from the 35 W amplifier is then reflected by the mirror into a water cooled beam dump. Additionally, the mirror entirely blocks the optical path within the asymmetric resonator of the high power oscillator, which instantly suppresses the laser oscillation. This shutter can be used to shut down the high power oscillator's laser output beam whilst keeping the thermal confinement unchanged, because the laser heads are still optically pumped. Furthermore, a so called *low power mode*, in which 50% of the beam of the 35 W amplifier are reflected at the output coupling mirror and which can be used for low power alignment purposes can be provided. The residual 50% of power in transmission of the output coupling mirror are dumped by the low power shutter.

Shutter S2 is identical in mechanical structure, but deflects the high power beam in front of the exit window to a 300 W water cooled thermopile power meter. A

concave lens with a focal length of -20 mm is placed in front of the power meter to increase the beam spot size in order not to exceed the intensity damage threshold of the meter. The shutter S2 acts both as a beam block for the high power beam of the laser system and as a power meter at the same time. A picture of the inside of the so called *high power shutter* is given in Fig. 4.41 below.
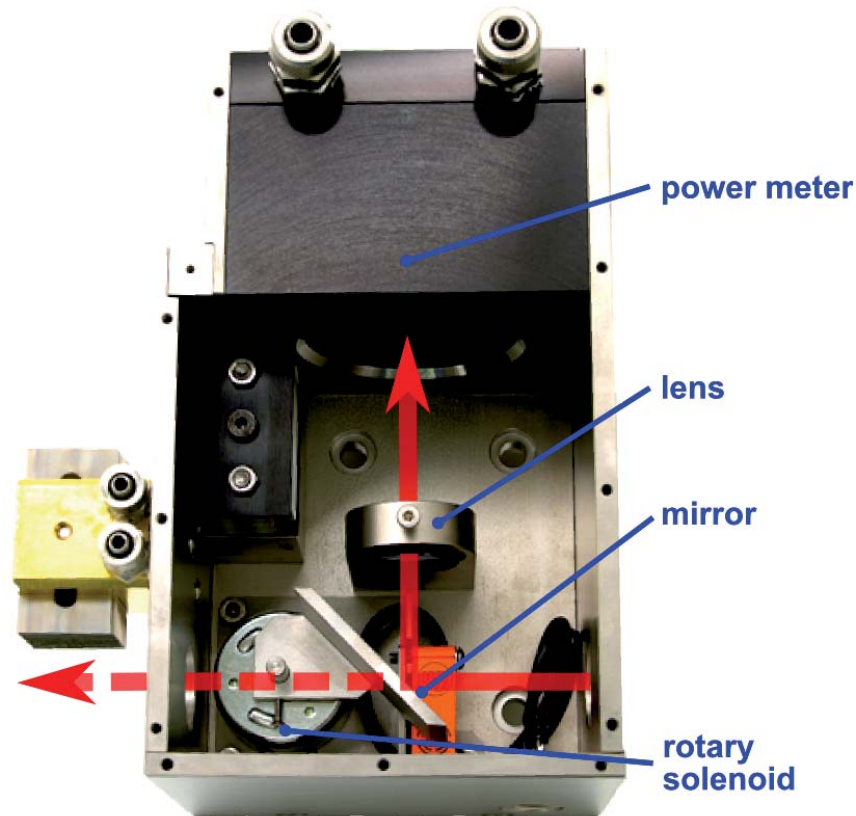

Figure 4.41: High power shutter with 45° mirror on flipper mounted to a rotary solenoid, f = -20 mm lens in front of the 300 W thermal power meter.

Chapter 5

Injection-locked laser performance

To provide a high power single-frequency laser output beam for the Advanced LIGO interferometer, the high power oscillator presented in the previous chapter was coupled to a 35 W amplifier system via the Pound-Drever-Hall injection-locking technique. As shown in Fig. 5.1, the low power seed beam is injected from the right hand side of the laser housing through the high power Faraday isolator into the four head ring cavity. To overlap the low power seed beam with the output beam of the high power slave oscillator two lenses (MM1 and MM2) are installed in front of the output coupling mirror. The size and divergence of both beams, i.e. the 35 W beam and the one from the high power oscillator, was then optimized for best overlap using two CCD cameras at different positions after the output window. Doing this, not only resulted in the best overlap outside the resonator, but also an optimized mode matching of the seed beam to the resonator internal beam path was obtained, which is required for optimized injection locking.

In a detailed characterization, the suitability of the laser system as a light source for the next generation of GWDs was verified. Besides the output power and beam profile of the injection-locked laser, the higher-order mode content and the noise characteristics of the laser beam are important parameters for a light source for GWDs. The experimental data obtained during the characterization and an outlook on the performance of the actively stabilized laser will be given in the following sections.

5.1 Output power and beam profile

When being injection-locked, the laser system delivers an output power of 220 W. Due to the highly aberrated thermal lenses inside the laser crystals, a deviation of the laser's fundamental mode from a perfect TEM_{00} mode is observed. In fact, a
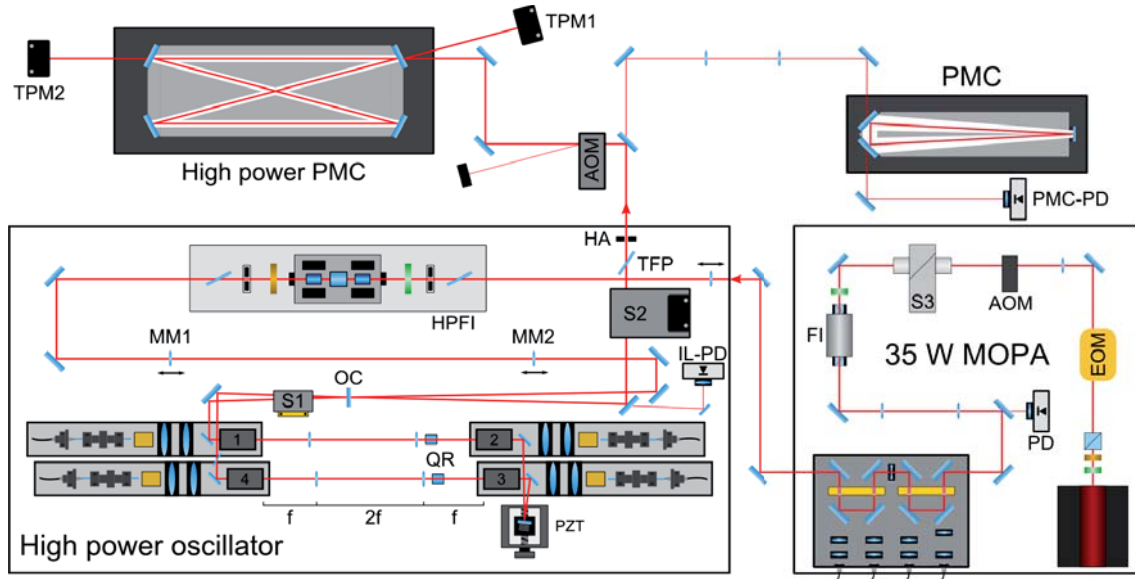
Figure 5.1: Optical layout of the fully assembled and injection-locked laser system, consisting of the high power oscillator and the 35 W amplifier. For diagnostics, a low power mode filtering resonator is installed behind the exit window of the high power laser. Additionally, the full power beam is sent through a second filter cavity to verify the available output power in the TEM_{00} mode for the GWD. Furthermore, a high power acousto-optical modulator was placed in the beam for control of the laser beam power. All hardware external to the laser was supplied by the Max-Planck Institute for Gravitational Physics in Hannover.

halo, which is clearly separated from the central TEM_{00} mode part of the beam, can be identified with a CCD camera. An image of the fundamental mode beam with the surrounding halo can be seen in Fig. 5.2 on the left. In a beat measurement of the injection-locked output beam no beat notes could be observed, which is typical for a single-frequency laser, where no longitudinal modes can beat with each other. Consequently, no evidence that this halo is related to any higher-order mode oscillating inside the laser cavity could be found.

Approximately 40 W of the laser output power is contained within the halo structure surrounding the TEM_{00} intensity distribution (output power without halo aperture – power with aperture in place). The optical power in this halo mainly depends on the alignment of the 35 W beam into the high power oscillator cavity and the alignment of the four head ring resonator itself. Improving the seed beam's overlap, in terms of waist position and divergence, with the laser output beam the power contained in the halo can be minimized. Thus, it was critical during alignment of the 35 W amplifier into the high power oscillator not only to optimize the output power, but also to take into account the live image of the laser's beam profile.
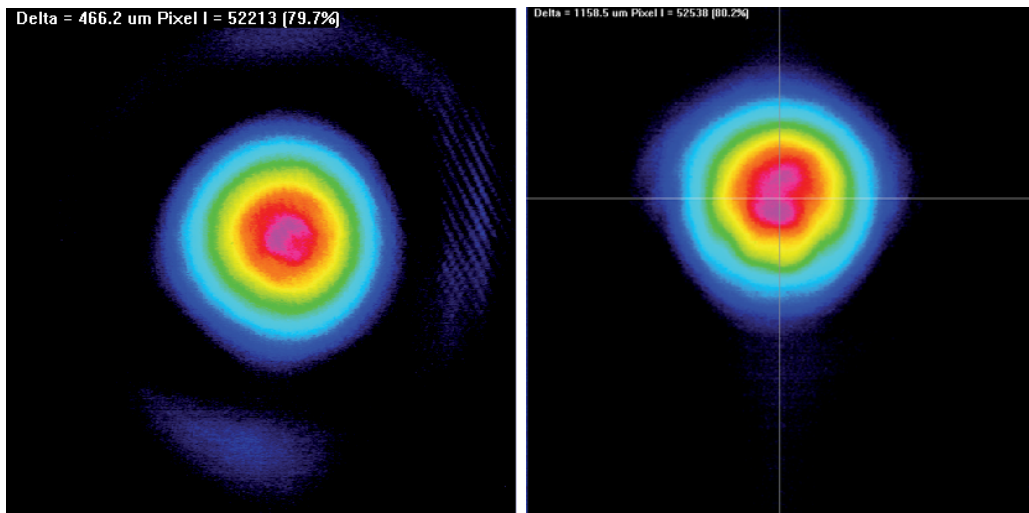
Figure 5.2: **Left**: Beam profile of the injection locked laser with an output power of 220 W. **Right**: Beam profile of the cleaned output beam with the halo aperture installed.

For active power stabilization (performed by the Max-Planck Institute of Gravitational Physics) of the laser's output beam, an acousto-optical modulator (AOM) was installed. In first experiments, it turned out that the power in the halo is absorbed at the entrance aperture of the AOM. To avoid temperature induced damages and misalignment of the AOM, the halo structure was removed before exiting the high power oscillator housing by a water cooled hard aperture. In fact, the diameter of this aperture, whose 3D CAD model can be seen in Fig. 5.3, is chosen to be sufficiently larger than the center beam in order not to cause diffraction of the output beam. For a pure Gaussian beam, the diameter of the aperture has to be larger

Figure 5.3: 3-dimensional model of the water cooled halo mount with screwed-in variable diameter aperture.

than $d_A = 4.6 \cdot \omega_0$ to have more than 99 % of the power in transmission without diffraction [Sie86]. As the output beam diameter for different lasers differ slightly at the position of the halo aperture, the size of the aperture inside the pin hole insert is adapted to each beam. Even though the diameter of the aperture is suitable for the Gaussian distribution, a residual diffraction of the beam is visible on the CCD camera image, as seen in Fig. 5.2 on 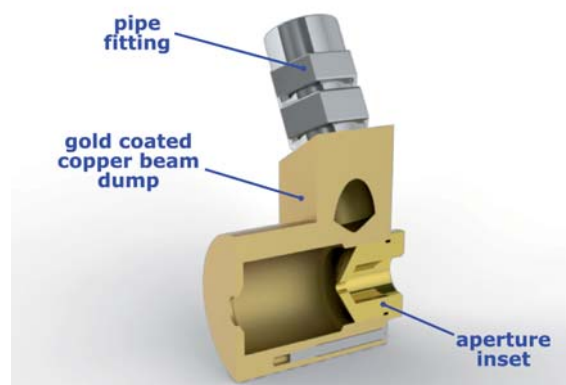the right. By measuring the actual higher-order mode content with and without the halo aperture in place, a significant beam quality increase could be verified. A representative set of data of these measurements is presented in Section 5.3.

5.2   Injection-locking characteristics

As described above, the 35 W MOPA beam's waist size and position is transformed to the one of the high power oscillator by a set of mode-matching lenses. During normal operation, the Pound-Drever-Hall locking electronics (developed and supplied by the Max-Planck Institute for Gravitational Physics) is operated in closed-loop with an automated lock acquisition to compensate for disturbance related losses of injection lock. In fact, an alignment of the master beam into the slave resonator in this state of operation is disadvantageous, because the only reference will be the output power of the injection-locked laser. An additional feedback signal for the angular alignment and hence for a better overlap of the seed and oscillator beam, the injection locking error signal can be used. For this purpose, the closed-loop operation of the injection locking electronics is switched off. Subsequently, a voltage ramp with a frequency of 10 Hz and a peak-to-peak voltage of 10 V is connected to the input port of the high-voltage driver of the slave resonator piezo actuator. The piezo actuated mirror of the high power oscillator is ramped back and forth by the applied voltage from the driver, altering the resonator length by approximately 8 free spectral ranges (FSR) over one period. The error signal generated by the Pound-Drever-Hall electronics is displayed on an oscilloscope to have direct feedback for the alignment of the laser system. A representative oscilloscope trace of the monitoring signals used during alignment is given in Fig. 5.4.
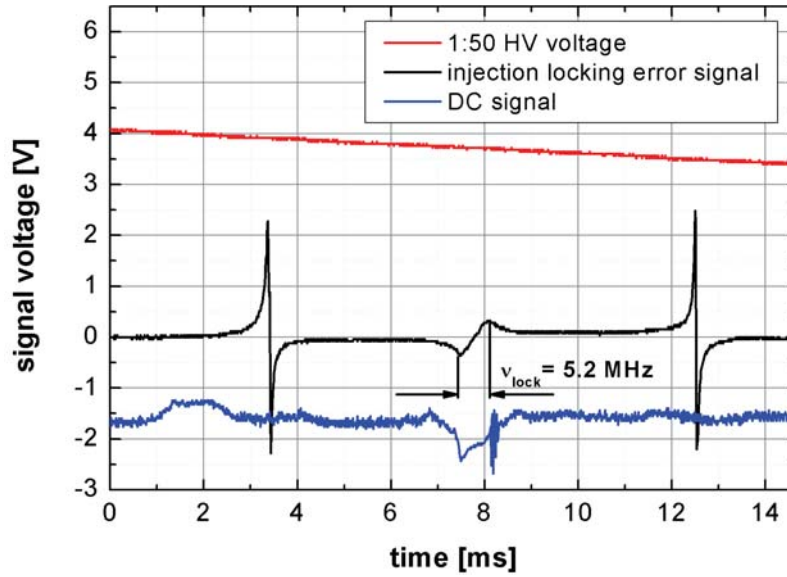
Figure 5.4: Oscilloscope trace taken during alignment operation of the PDH injection locking electronics.

Taking the large sideband resonances of the error signal (black) as a frequency reference, the locking range of the high power slave laser can be distinguished. For the given measurement, the broadband EOM type 4004 from New Focus was modulated at a frequency of 35.5 MHz and driven with a peak-to-peak voltage of 500 mV. Assuming that the piezo actuated mirror moves linearly within the displayed time span, a locking range of 5.2 MHz can be extracted from the measured data. As discussed in Section 3.4.2, the output beam characteristics of the oscillator change from bidirectional operation to unidirectional single-frequency operation within the locking range. At the same time, the output voltage (blue) of the photodetector for the heterodyne signal detection decreases. Please note that lower voltage values stand for higher intensities at the photodiode. The measured dip in the signal indicates an output power increase in forward direction under resonant conditions. When set to the automated lock acquisition, the PDH electronics would try to keep the error point signal at the zero-crossing, moving the PZT actuator to control the high power oscillator's resonance frequency. In the given case, the piezo actuated mirror moves on, causing the oscillator to fall out of frequency lock. At that point, the coupling of the injected 35 W MOPA beam and the high power slave ceases. As a consequence, the free-running laser field inside the four head ring oscillator is built up again. This process is indicated by a transient voltage signal, which will be discussed in the following text.

Spiking

As the pump power of the complete laser system is only altered on time scales of seconds for alignment purposes, the regime of operation can generally be considered to be in a steady-state. This assumption is not true for the time domain, in which the high power slave looses its frequency coupling with the injected seed. As presented in Fig. 3.11 the field intensity of the free-running laser within the high power oscillator is decreased until it vanishes when the difference between resonance frequency and carrier is within the locking range. When the slave resonator's length and hence frequency difference in respect to the carrier frequency exceeds the locking range, the oscillator will start to lase again. At this point, the stored energy of the inversion of the laser gain media of the oscillator is released, generating a single pulse. In fact, the inversion is dissipated faster than the pump light can supply new energy, so the oscillation stops. As soon as the inversion is enough to exceed the laser threshold again, a second pulse is sent out and so on. The result is a train of pulses with decaying amplitude, which settles down on the continuous wave output power level.
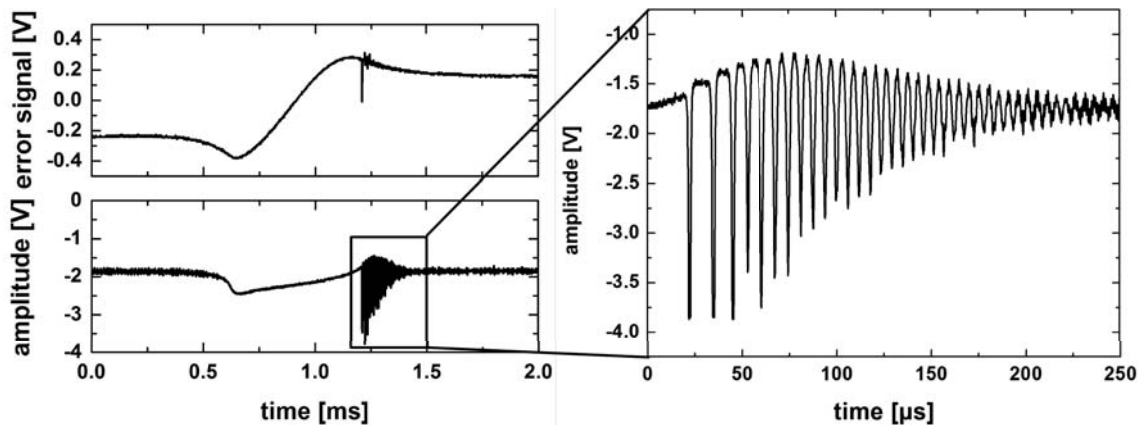
Figure 5.5: Spiking characteristic, when the high power oscillator looses injection lock with the 35 W MOPA seed.

This transient effect, which is shown in Fig. 5.5, is called the *relaxation oscillation* or *spiking*. It is noticeable in all solid-state lasers where the upper-state lifetime ($230\ \mu s$ for 0.1 at% doped Nd:YAG) is longer than the cavity damping time. Typical pulse trains generated when the high power oscillator falls out of lock have a peak power exceeding the average power of the locked laser system. Each pulse has a peak intensity which is significantly higher than the one of the locked laser system. As a consequence, all optical coatings inside the high power oscillator were specified to have a much higher intensity damage threshold than needed during continuous wave operation.

Automated relock

As described previously, the high power slave oscillator is kept in resonance with the 35 W MOPA beam by an analog control loop. In the presence of strong mechanical disturbances, e.g. hitting the optical table with a hammer, the injection-locking control loop is not able to compensate for the vibrations coupled into the opto-mechanical structure of the resonator. The same is true for a fast carrier frequency glitch of the master laser of the 35 W MOPA beam. For a fast recovery from such a loss of injection lock, an automated relock controller was included into the PDH electronics. When the controller detects a loss of injection lock (the voltage at the injection-locking photodiode drops below a set threshold value), it applies a ramped voltage to the PZT. As described earlier, an output power increase is detectable, when the frequency difference of the high power oscillator and the carrier is within the locking range. This signal triggers the electronics to switch off the ramp and activate the control loop to establish the injection lock anew.
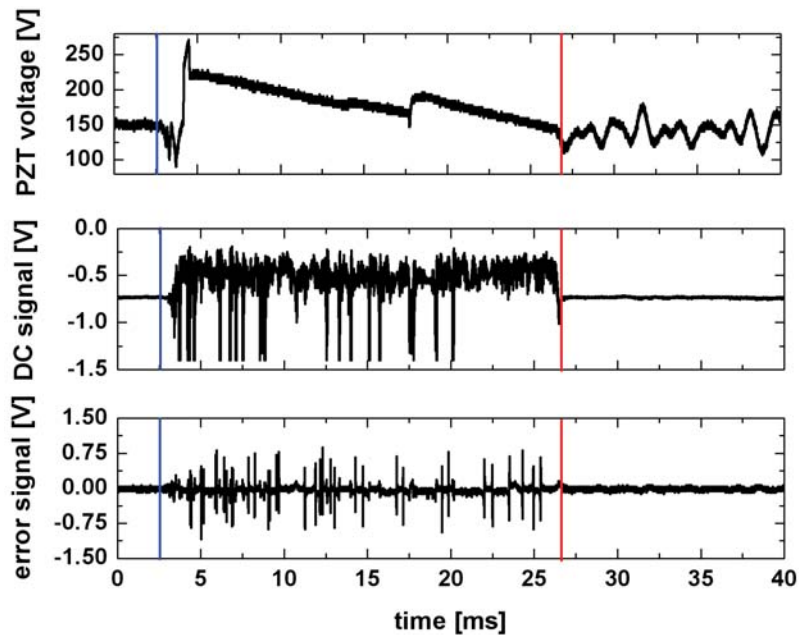
Figure 5.6: Relock event triggered by hitting the table with a hammer (indicated by the blue line). In this case the relock took about 20 ms. At 17.5 ms the control loop tried to relock, but the mechanical disturbance by the hammer hitting the table were still to big.

As shown in Fig. 5.6, the PDH electronics is capable of reacquiring stable lock in a few milliseconds. Typical relocks of the high power laser for Advanced LIGO are recovered within a time scale of under 100 ms.

Error signal disturbance coupling

In Fig. 4.2 of Section 4.1.1 it was shown that beat-frequencies of higher-order modes can be detected with a fast photodetector, when the free running laser system is not operated strictly at the fundamental mode operation point. Even though the resonator geometry discriminates higher-order modes during normal operation, some mode beat signal residuals are always present in the photodiode's heterodyne detection signal. The amplitude of these beat notes are almost not noticeable in the beat signal, as they are masked by the background noise of the photodetector.
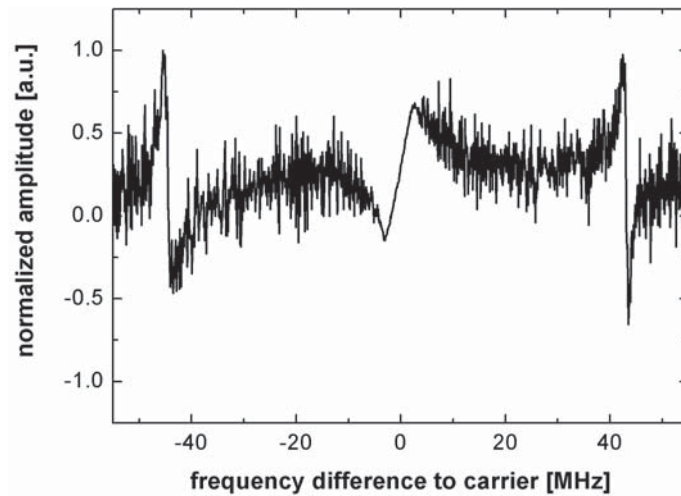
Figure 5.7: Measured error signal at a modulation frequency of 44.5 MHz for the generation of sidebands. The region for an instable error signal starts at 42.5 MHz and ends at 48 MHz.

For the given high power resonator configuration the first higher-order mode has a beat note at a frequency difference of approximately 45 MHz with respect to the fundamental mode beat of the free-running laser. When the modulation frequency of the seed's side bands approaches this frequency range, a disturbance of the error signal is detected. A typical distorted error signal is shown in Fig. 5.7. It can be seen that the injection-locking error signal is noisy, when the slave oscillator cavity is not in resonance with the sidebands or the carrier. Usually, a low-pass filter with a corner frequency of approximately 5 MHz will remove beat signals after the mixer inside the locking electronics. As soon as the sideband modulation frequency is near ($\pm$ 5 MHz) a higher-order mode beating frequency, the amplitude modulation caused by the higher-order mode is no longer filtered. Within the locking range, the higher-order modes of the slave oscillator are suppressed, resulting in a clean error signal.

In principle, the oscillator can still be locked with such a noisy injection locking error signal, as the oscillation of the higher-order mode ceases when the slave oscillator cavity is in resonance with the carrier or the sidebands. However, the time required for an automated relock is significantly increased, because the locking electronics is distracted by all glitches with a zero crossing and a slope with the same sign as that of the carrier resonance.

So far, this phenomenon was not studied further during this work, as it can be easily avoided by adjusting the modulation frequency to a region without disturbances coupling into the error signal. Furthermore, a decision was made to fix the sideband modulation frequency to 35.5 MHz, which was already used within laser related control loops during the Initial and Enhanced LIGO operation. At this modulation frequency no error signal distortions were detected for various laser resonator configurations and laser prototype setups during the development.

5.3 Higher-order mode content

In interferometric gravitational wave detectors, only the power in the TEM_{00} mode can be utilized. In order to analyze the fraction of the output power in this fundamental Gaussian mode, a scanning non-confocal ring cavity was used. This cavity is based on the design of a Pre-Mode Cleaner (PMC) developed for the LIGO detector [Wil98] and was supplied by the Max-Planck Institute for Gravitational Physics in Hannover. A small portion of laser light, approximately 130 mW, is sampled after a HR mirror behind the laser's output window to determine all laser output beam parameters (see Fig. 5.1). This laser beam is then aligned and mode-matched to the PMC cavity. As the PMC cavity is a non-confocal cavity, the different transversal modes have different eigenfrequencies. The input beam can be decomposed into the eigenmodes of the PMC by scanning the PMC cavity length over one free spectral range and monitoring the transmitted power signal.

Two different characteristic mode scans are shown in Fig. 5.8. To derive the fraction of power in higher-order modes, a numerical fit is performed. From this fit, the power and order of the individual higher-order modes are obtained. Unfortunately, a background, which is caused by the halo surrounding the TEM_{00} mode profile, is not taken into account by the numerical fitting algorithm. Hence, there is a deviation of the fitted (solid red) curve to the actual measured fractional power in higher-order modes (solid black) visible in Fig. 5.8a. From measurements of the laser power transmitted by the high power PMC, a higher-order mode content of more than 12% was confirmed.
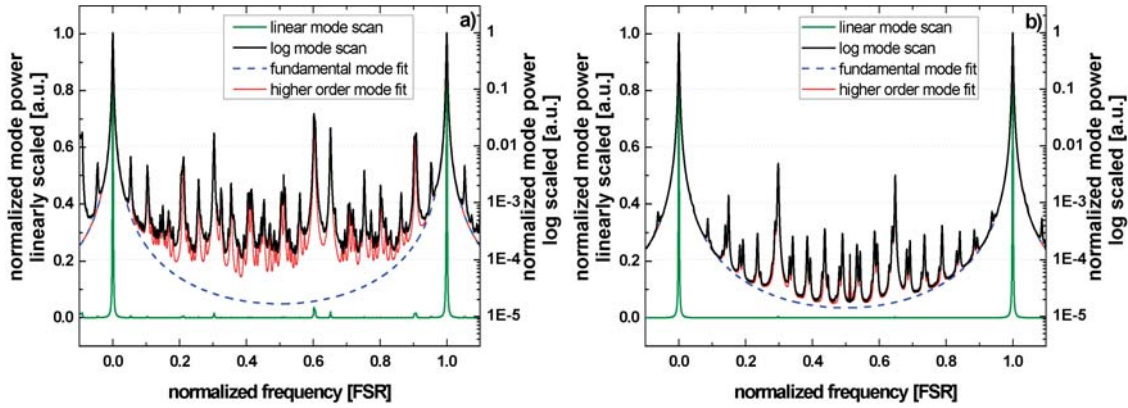
Figure 5.8: Transverse mode scan. **a)** Measured higher-order mode content of < 12 %
without halo aperture in output beam. **b)** Higher-order mode content < 7.5 %
with halo aperture.

For the second measurement (Fig. 5.8b) the halo structure was removed with an
external water cooled hard aperture, which was described in Section 5.1. Approx-
imately 40 W of output power was dumped into the halo aperture, resulting in a
remaining output power of 180 W. In this configuration, a mode scan without the
background present and a higher-order mode content of only 7.5 % was measured.
According to the Advanced LIGO requirements given in Section 2.1, the final laser
output power in the fundamental Gaussian mode has to be more than 165 W with
less than 5 W of power in higher-order modes. To filter out all higher-order modes,
a PMC optimized for high incident power levels is used. Unlike the low power PMC
described above, the high power version is based on a bow-tie resonator configuration
to increase the resonator length while keeping the overall size small (developed and
supplied by the Max-Planck Institute for Gravitational Physics [Pöl10]). Using a
second set of Pound-Drever-Hall electronics and recycling the phase modulation
side-bands reflected from the high power oscillator, the filter cavity was locked to
the high power beam of the laser. The maximum achieved transmitted power in the
TEM_{00} mode was 168 W, which is consistent with the mode scan after the halo
aperture.

5.4   Relative power and frequency noise

To reduce the influence of laser power and frequency noise on the gravitational wave
detection signal, an active stabilization of the laser system is required. In order to
minimize the loop gain requirements for the various stabilization stages, the output
beam power and frequency fluctuations have to be kept at the lowest level possible.
In Fig. 5.9a, the free-running frequency noise spectrum of the injection-locked laser

system at an output power of 220 W is shown. For comparison, the frequency noise spectrum of the NPRO used in the laser setup and the LIGO requirements are given in Fig. 5.9a as well. These measurements were taken with an optical diagnostic device developed by Kwee et al. [Kwe07] and fabricated at the Max-Planck Institute for Gravitational Physics. It can be seen that the NPRO dominates the frequency noise of the 220 W beam and that the amplifier and the high power oscillator add only approximately 5 dB of frequency noise at that frequencies. Hence, it is expected that a stabilization scheme similar to that used for initial LIGO [Wil10, Sav98] will be sufficient to reach the required frequency noise (dashed line in Fig. 5.9a).
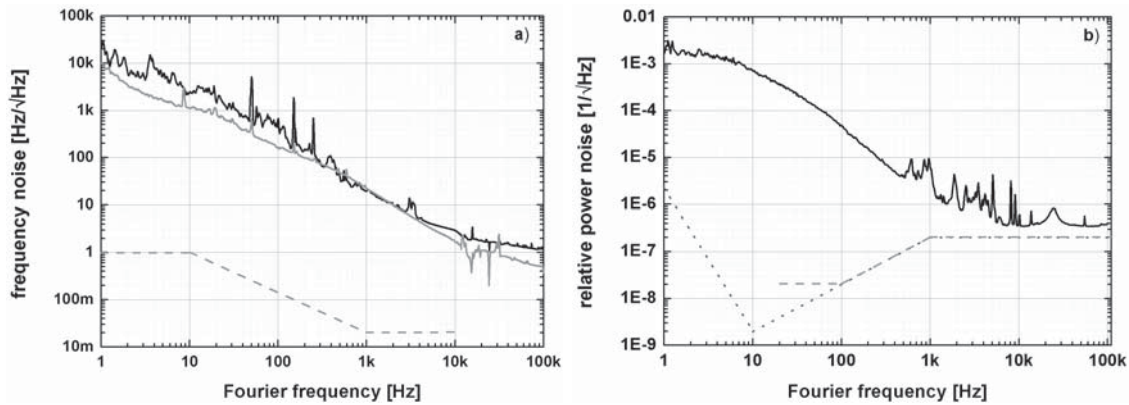
Figure 5.9: **a)** Frequency noise of the free-running laser. Gray solid line: typical frequency noise of a NPRO. Dashed line: Advanced LIGO requirements. **b)** Relative power noise spectrum of the free-running laser output beam. Dashed line: Advanced LIGO requirements at the interface to the interferometer. Dotted line: Advanced LIGO requirements inside the interferometer.

For characterization of the power noise of the laser system, two different measurements were performed. First of all, the peak-to-peak power fluctuations over 300 s of the output beam were determined. For this, the output of a photodiode was sampled either with an oscilloscope or a data acquisition (DAQ) system. The oscilloscope was set to the maximum sampling rate of approximately 26 kHz with the detector set to peak-detection while the DAQ system took samples at a rate of 125 kHz. In both cases, the relative peak-to-peak power noise of 7 % set the requirement on the dynamic range of the power actuator used for the active stabilization.

The second measurement reveals the RMS relative power fluctuations at different corresponding Fourier-frequencies (see Fig. 5.9b). To fulfill the requirements of the actively stabilized laser for the Advanced LIGO interferometer, the power variations at a frequency of 10 Hz have to be less than $2 \cdot 10^{-9}$ $Hz^{-1/2}$ at the interferometer core. Directly after the high power PMC the requirements on the relative power fluctuations for lower frequencies are more relaxed.

5.5 Long term stability

To fulfill the requirements for the Advanced LIGO detector's availability of 75 % with a continuous data stream of the locked interferometer of more than 40 h, the long term output power stability of the developed laser system had to be verified. In the first long term experiment, constant monitoring of the laser's output characterisitcs was installed after the first prototype was delivered to the Max-Planck Institute for Gravitational Physics in Hannover as a test bed for their stabilization scheme and electronics.

As shown in Fig. 5.10, the laser's output power was recorded for 256 days, whereas the laser itself was continuously operated for nearly one year at the Max Planck Institute and 3 months during assembly at the Laser Zentrum Hannover. During the entire time, a lot of optimization and maintenance was performed on the first delivered prototype laser system. These periods, in which most of the time the laser was shut down, can be seen as power glitches in the graph displayed in Fig. 5.10. Nevertheless, the laser was operated for 206.4 days with an output power of more than 185 W and 177.6 days with more than 200 W in total. This corresponds to an up-time for the 200 W output power operation of 69 %. Furthermore, it was verified that the power loss observed during continuous operation was caused by a degeneration of the pump diode lasers and not of the laser oscillator itself. As described in Section 4.2.4, the output spectrum and power of all diode lasers of one LDB are constantly monitored at the laser head module. With the stored data, the output power loss of the injection-locked laser can be easily compensated by a regular adjustment of the diode laser's currents and optimization of the spectral distribution.
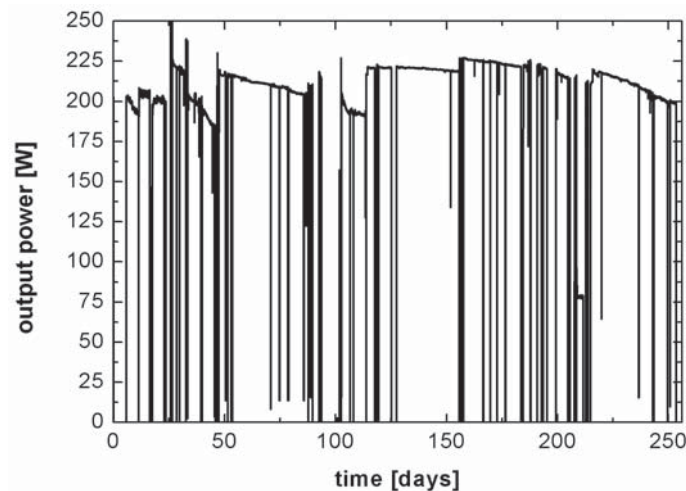
Figure 5.10: Long term power measurement of the first prototype delivered to the Max Planck Institute for Gravitational Physics in Hannover for first stabilization tests.

5.6   Actively stabilized output characteristics

All experimental results related to the Advanced LIGO laser presented in this work were measured for the free-running laser system only. For the use of such a laser inside a GWD, an active stabilization of the frequency and output power noise had to be applied to the complete laser system in order to fulfill the requirements defined in the *Final Design Document* [Kim10]. The necessary electronics, optical hardware and techniques for this active stabilization were developed and fabricated at the Max-Planck Institute for Gravitational Physics in Hannover. For the engineering development process and for further testing of the stabilization setup, two Advanced LIGO lasers were delivered and installed at the Max-Planck Institute for Gravitational Physics. The resulting frequency and intensity stabilization loops can be seen in the schematics in Fig. 5.11. The complete laser system including NPRO, 35 W MOPA, high power oscillator, high power pre-mode cleaner resonator, and equipment used for the stabilization is called the *pre-stabilized laser* or *PSL*. The preposition *pre* accounts for the various additional measures that will be taken by other groups participating in the Advanced LIGO installation to suppress the laser's output noise before it will enter the interferometer.

Figure 5.11: Schematic layout of the Advanced LIGO laser including the frequency and intensity stabilization scheme. AOM: acousto-optical modulator, EOM: electro-optical modulator, FI: Faraday isolator, PMC: pre-mode cleaner cavity, NE: NPRO internal noise eater (suppresses the relaxation oscillations), FSS: frequency stabilization electronics, and ISS: intensity stabilization electronics [Wil10].

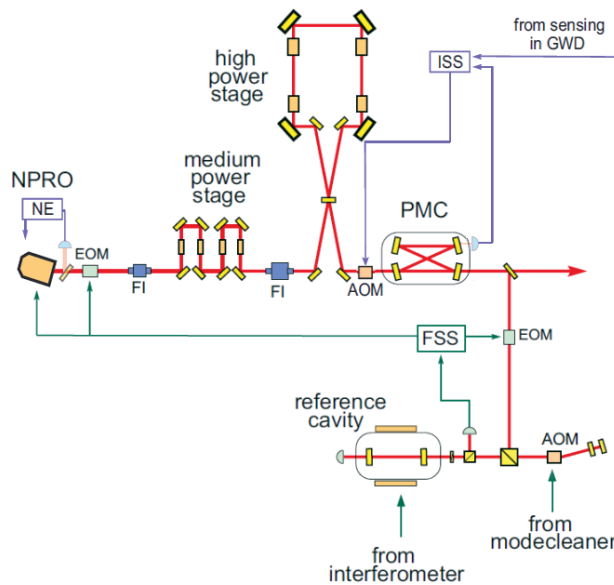In the following text, preliminary experimental results for the actively stabilized laser system are presented. The measurements were performed by the Max-Planck Institute of Gravitational Physics. They are presented here to give a well rounded overview of the Advanced LIGO laser's performance.

The goal for the frequency stabilization was to achieve an intermediate stability level and to supply an integrated high-bandwidth actuator, which use the GWDs long arm cavities as a reference for their control loops. As shown in Fig. 5.11 on the left, the laser frequency is stabilized to a rigid-spacer high-finesse reference cavity. This cavity is suspended in a vacuum chamber and thermally controlled, to keep its length and hence resonance frequency constant. Only a small portion of the high power output beam of the laser is picked off and sent through an EOM, which imprints control sidebands on the beam. Again, a Pound-Drever-Hall locking scheme is used to determine the deviation of the laser's frequency from that of the static resonance frequency of the reference cavity. The output control signal is then fed back to the NPRO's internal piezo actuator [Inn11], which changes the length of the crystal and thus the carrier frequency for the complete system. In addition, a second EOM is placed between the MOPA and the NPRO, which is used as a fast phase correction actuator. Before the low power beam enters the reference cavity, it is doubled-passed through an AOM. When the laser is injected into the mode cleaner, the AOM is used to adapt the stabilized laser frequency to the frequency resonance of the mode cleaner cavity.
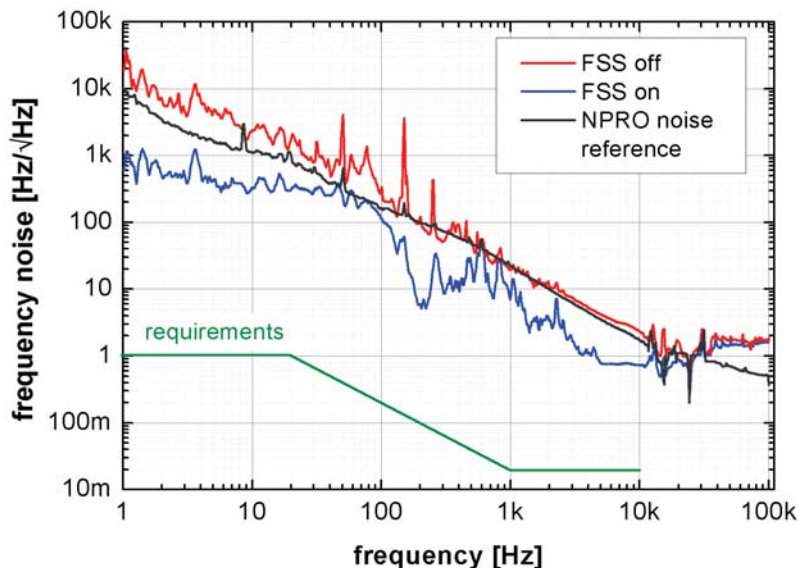
Figure 5.12: Frequency noise measured with the diagnostic breadboard, with: free-running laser (red), frequency stabilized laser (blue), NPRO reference noise with FSS off and requirements (green).

A comparison of the noise of the free-running laser, which is mainly dominated by the frequency fluctuations of the NPRO, and the stabilized system is presented in Fig. 5.12. In fact, the measurement of the frequency fluctuations of the actively stabilized laser is limited by the frequency noise of the PMC inside the diagnostic breadboard. Thus, no distinct statement, whether the requirements for the frequency stabilization are met, could be made so far.

For the power noise stabilization, an AOM was directly installed in the high power beam downstream of the high power PMC. A portion of light, approximately 13 %, is constantly diffracted from the beam to have sufficient actuator range to compensate for positive and negative power fluctuations. Even though the AOM is designated as a fast-power actuator it is possible to utilize it for a compensation of long term power drifts by controlling the average amount of diffracted power. Following this scheme it was shown in preliminary experiments of F. Seifert et al. [Sei06] and P. Kwee et al. [Kwe09] that an active power stabilization is capable of reducing the power noise of an NPRO down to the required values. As the power noise of the Advanced LIGO laser is significantly larger, more gain is needed for the control servo. At least 110 dB of actuator range are necessary for a sufficient stabilization of the power fluctuations at a frequency of 10 Hz.
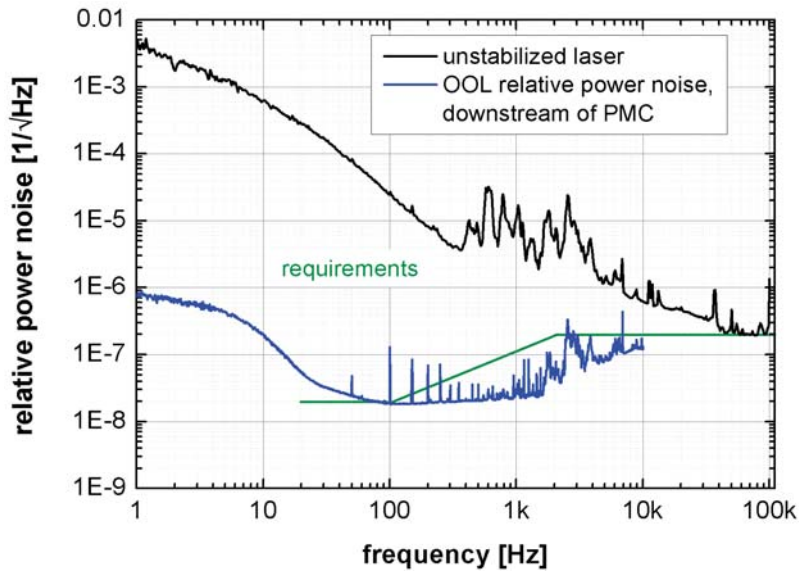
Figure 5.13: Relative power noise measured with the diagnostic breadboard and the out-of-loop (OOL) photodetector, with: free-running laser (black) and power stabilized laser (blue) and requirements (green).

Two identical photodetectors were used for the stabilization of the relative power fluctuations of the free-running laser. An in-loop (IL) photodetector generates the error signal for the stabilization loop, whereas the relative power fluctuations of

the stabilized laser are measured out-of-loop (OOL) with the second photodetector, simultaneously. Both photodetectors where installed in a housing to shield them from stray light coming from beam dumps and thermopile power meters on the optical table. In Fig. 5.13 the relative power noise of the free-running laser is compared with the noise at the OOL photodetector when the stabilization is activated. It can be seen that the stabilized laser performance does not completely fulfill the requirements defined in the *Final Design Document* at the moment [Kim10]. But one is confident to be able to reduce the relative power noise of the pre-stabilized laser to a desired level in the foreseeable future.

Chapter 6

Outlook

6.1 Production, delivery and on-site-support

In total, three Advanced LIGO laser systems are produced. So far, one laser system has been installed at the LIGO detector located in Livingston, LA. The second laser system was shipped to LIGO Hanford, WA, in July 2011 and was installed in October 2011. For the third laser system, destined for LIGO Hanford as well, the shipment and installation is scheduled for the second quarter of 2012. One has to keep in mind that the 35 W MOPA systems are already installed and were used at the LIGO GWDs. Therefore, only maintenance work of critical parts and installation of the new control electronics for integration into the full Advanced LIGO PSL will be performed. In addition to the three lasers, two sets of optical, mechanical and electrical spare components were manufactured. These components will be stored at each site and will guarantee short maintenance periods because of the obsolete shipment of needed replacements. Furthermore, the number of supplied parts was calculated to keep the system in operation for years in advance, which is necessary for the Advanced LIGO science run.

For an efficient production of the high power oscillator and its spare parts, all mechanical subassemblies were designed as modular units during the development process. This made it possible to manufacture similar subassemblies in a single production step. In fact, only two high power oscillators can be fully assembled simultaneously and only one can be optically aligned and tested because of limited table space inside the clean room laboratory. Some representative pictures for the assembly work are given in Fig. 6.1
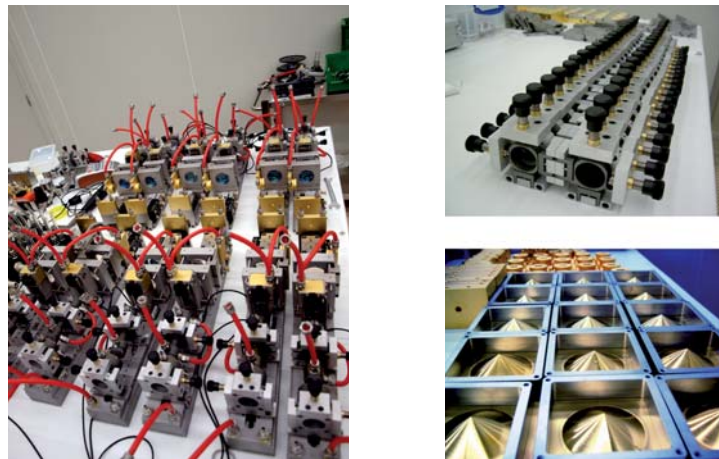
Figure 6.1: Production of subassembly components, left: laser head modules, top-right: XY-positioning mounts, and bottom-right: gold coated copper heat sinks.

During the development and qualification phase of the laser systems, a high number of dust related damage occurred during operation. The damage could be traced back to an insufficient level of cleanliness in the standard optical laboratories. Thus, the decision to move the development and finally the production of the Advanced LIGO laser into a clean room environment was made. This clean room, built in 2008 and first used for laser experiments in 2009 has an ISO6 specification, which corresponds to 1000 particles (0.5 μm) per cubic foot. With this measure, the dust related damages were reduced to almost zero.

The first installation of the Advanced LIGO laser system including the stabilization developed by the Max-Planck Institute for Gravitational Physics in Hannover was carried out from Spring to Summer 2011. To have a sufficient safety margin regarding the date of the on-site delivery of all components, the shipment to the United States was performed in December 2010. As a rehearsal for the shipment and procurement of the optical, mechanical and electronic hardware, two different prototypes were delivered to the Max Planck Institute for Gravitational Physics in Hannover. One of the delivered lasers, which is an exact copy of the Advanced LIGO laser will be operated there as a reference system and to develop and to test strategies to troubleshoot and solve unforeseen technical issues. Another aspect of these two test run deliveries was to test installation procedures and rule out problems during the installation phase in advance.

Special attention was paid to the durability of the laser system's mechanical structure to survive an ocean transportation. Most of the optical mounts inside the high power oscillator are lockable by backing nuts to keep their designated position even though vibrations are coupled into the structure. All screws of the mechanical as-

semblies are fixed with a non out-gassing epoxy, which is easily removable if a part has to be replaced by a spare. The springs of all optical mounts are reinforced, compared with the standard version, to withstand shock during the transport, and all optical components are fixed with a vibration absorbing adhesive, specially designed for optical systems. In addition, the housing of the high power oscillator is sealed against dust and all electrical wires inside the box are fixed by cable ties. Furthermore, the water of the various cooling circuits is completely drained and each water line was flushed with dry air to remove the remaining residuals of water vapor from the tube.

Figure 6.2: High power oscillator prior to shipment with installed lifting frame, top lid and hooks - the side is removed for illustrative purpose only.

To be able to lift the high power oscillator, a metal frame was designed, which is directly attached to the base-plate. As shown in Fig. 6.2, the top lid of the oscillator has openings to support hooks, which are attached to the lifting frame in the inside. With these hooks, the oscillator, which weights around 340 kg, can be lifted from the optical table and transported by a crane. After the on-site installation, the frame can be removed completely and is exchanged by a place holder to refit the dust sealed housing.

Besides all these design measures, two different methods of transportation had to be ruled out. The fastest way of shipping the hardware would have been air freight. A little bit slower, but much more comfortable to organize is the transport via a cargo ship. One has to keep in mind that the approximately net weight of all laser components including spares and electronics was estimated to be roughly 4 tons. Transportation via airplane would be doable, but only if the laser components would be shipped separately. From experience, the handling of delicate freight at airports involves a high potential risk for damage. Furthermore, the costs of this way of transportation are expansive.

When transported by a cargo ship, all subcomponents were packed in separate boxes and locked into a container at the production site. This cargo container is then de-

livered to the observatory, whereas the single components of the laser would have to be loaded on a truck again at the airport. Loading and unloading of such delicate components is said to be the most critical operation and causes the most severe damage in general. Because of these reasons, all the Advanced LIGO laser systems were or will be shipped by sea cargo. To protect the optical, mechanical, and electrical components against the aggressive salt water, all critical parts of the laser were packed in sealed and evacuated plastic bags. Silica gel packages were enclosed for a reduction of the humidity inside these bags.

After delivery to the LIGO Livingston observatory, the installation of all subcomponents was carried out by trained personnel from the Laser Zentrum Hannover, the Max Planck Institute for Gravitational Physics and neoLASE GmbH. The current data of the laser system installed at the LIGO Livingston observatory shows an equivalent performance compared with that before delivery. At the moment, further tests are on the way to prove the long term stability of the laser at the site.

After the first installation and extensive long term tests are finished, the laser has to be maintained by LIGO staff. Because the alignment of the high power oscillator is relatively complex, some selected crew members of the LIGO team were trained during assembly of the laser system in Hannover, Germany. In addition, a secure shell connection to the control computer of the Advanced LIGO laser gives online access to all functions for remote maintenance. Furthermore, all relevant monitoring channels are stored continuously and the long term data is remotely accessible via a TCP/IP connection.

6.2 Laser for the 3rd generation of gravitational wave detectors

In the overview of this thesis, the technological improvements from the first generation of Earth bound GWDs to the actual and advanced machine were described. With the advanced GWD configuration, a possible detection of a passing gravitational wave is thought to be almost guaranteed. However, even though the sensitivity of the advanced detectors will be improved by a factor of 10 compared to the initial setup, a detection of gravitational wave phenomena will only happen on a time scale of several days or weeks. In addition, the signal-to-noise ratio of these detections will be too low for a precise astronomical study of the astrophysical properties of gravitational wave sources.

Although the new technologies introduced and installed in upcoming advanced observatories will significantly increase the sensitivity, an additional sensitivity boost

by a factor of 10 will be needed to retrieve sophisticated data for the fields of astrophysics, general relativity, cosmology and astroparticle physics. For such an improved sensitivity of future GWDs, the fundamental noise sources, which currently limit the advanced detectors, have to be considered, which are:

- At low frequencies (below 4–5 Hz): Seismic and gravity gradient noise.

- In the 4–50 Hz regime: Thermal noise in the suspensions and radiation pressure noise on the optics.

- In the 40–300 Hz range: Thermal noise of the suspended optics (mainly the coatings).

- For higher frequencies: The shot noise.

To overcome these limitations, studies for a potential third generation GWD were conducted. These studies led to a conceptual design for a detector based on 'conventional' technology, which is called the *Einstein Telescope* or *ET* [Hil08]. The main technological improvements that have been suggested for this GWD were:

- Increased arm length to approximately 10 km, to enhance the sensitivity to the dimensionless space-time strain h.

- Underground site location for reduction of seismic noise.

- Long seismic filter chains to push the low frequency detection limit to lower frequencies <1 Hz.

- Cryogenically cooled test masses, to reduce the effects of mirror and suspension noise.

- Large and flat beams (higher-order modes or similar) to mitigate thermal lensing in the optics at high power levels and to suppress thermal noise couplings.

- Increased laser output power (1 kW for 1064nm or lower power for 1550 nm), to lower the shot noise limitations.

- Heavier test masses to compensate for the radiation pressure noise.

- Squeezed light injection to further reduce the quantum noise limitations.

Unfortunately, not all of these items can be combined into a single detector, which will be sufficiently sensitive for the entire desired frequency range. Thus, one plan is to build several different detectors into one site, which will cover well defined

frequency ranges with optimized sensitivity levels. Based on these considerations, a possible multiple detector assembly in a xylophone shaped geometry was introduced. As displayed in Fig. 6.3, different interferometer configurations with an angle of 60° at the beam splitter are combined in a huge triangular setup. In fact, an L-shaped GWD (A in Fig. 6.3) offers the better strain sensitivity, but the sum of the multiple detectors and their technological improvements will more than overcome this disadvantage.
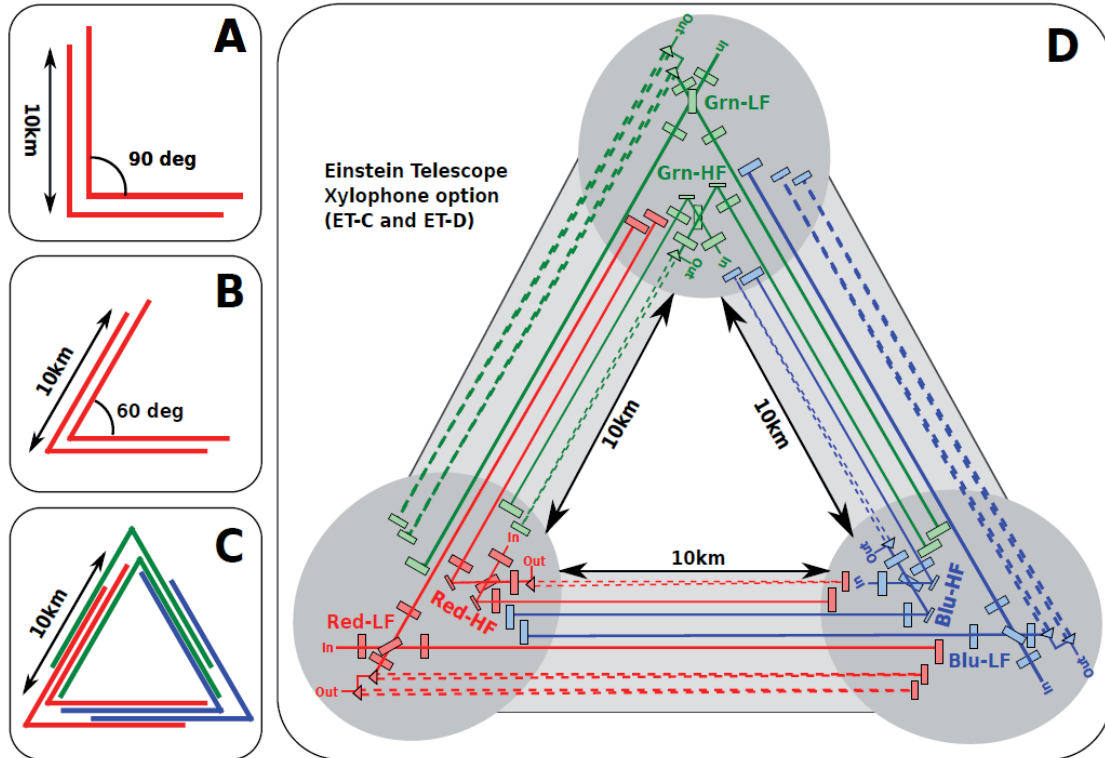
Figure 6.3: Different interferometer configurations considered for the realization of the *Einstein Telescope*. For the D configuration the optical paths for the *low frequency* (LF) and the *high frequency* (HF) detectors are shown in detail [Hil11].

In the actual design study for the third generation GWD ET-D [Hil11], two distinct laser system designs are required. For the high frequency (HF) interferometer, a high power laser beam with an output power of more than 500 W is desired. For a more uniform intensity distribution at the suspended test masses, a conversion of the single frequency fundamental mode to a higher Laguerre mode (LG_{33}) is required. For the low frequency (LF) interferometer, standard fused silica mirror substrates are replaced by silicon optics. These optical substrates offer very low absorption losses for laser radiation with a wavelength at 1550 nm. In addition, small structures can be etched onto the surface of the substrate in a lithography process. With these

structures with a scale of a few nm, diffractive optical elements can be fabricated, which do not have the disadvantage of additional optical losses in the thin film coatings.

For both types of interferometers, some effort will have to be put in the improvement of existing or the development of new concepts for continuous wave single-frequency lasers with a high power fundamental mode output beam. In the following sections, an overview of some of the most promising concepts for these future lasers will be discussed.

6.2.1 Laser at 1064 nm

Two basic concepts for high power single frequency laser systems have been previously described in Section 2.2: the Master Oscillator Power Amplifier (MOPA) concept and the injection locking of a high power slave to a low power seed. Both concepts have their advantages and disadvantages regarding fundamental mode content, long term stability, and power scalability.

As discussed before, injection-locked single-frequency lasers offer good beam quality at sufficient output power levels because of the filtering effect of the locked slave resonator. But one has to keep in mind that the output power of the high power slave laser will have to be significantly increased to achieve the output power levels desired by 3rd generation GWDs. In fact, a laser system with more than one kilowatt of output power in a fundamental mode output beam profile would be needed, which is a factor of five more power compared with the Advanced LIGO high power oscillator. In fact, the locking bandwidth decreases with higher output power of the slave oscillator. Thus, the power of the seed laser will have to be improved as well. In general, the requirement for such a high power system on its cooling scheme and safety measures would be very demanding, not to speak of the sophisticated alignment procedures needed. Consequently, the research in the field of single-frequency lasers for the third generation of GWD is currently focused on MOPA topologies.

In such a MOPA, a relatively low seed laser is amplified through a single or multiple laser active media. No control electronics are needed to keep the high power stage in resonance with the seed's carrier frequency, because the laser beam is simply amplified by passing through the laser gain media. While for injection-locked lasers, strong power and frequency fluctuations of the seed laser result in an unstable locking behavior, MOPA systems are less sensitive to those disturbances. Actually, the amplitude noise of such a MOPA system can be controlled by applying an adequate stabilization to the low power seed only. Controlling the seed instead of a direct manipulation of the high power beam significantly reduces the complexity of the overall laser system.

For amplification of narrow linewidth seed lasers with a wavelength at 1064 nm, two different types of amplifiers are being studied: solid-state amplifiers, which are usually based on Nd:YAG for high power applications, and ytterbium doped fiber amplifiers.

Recent developments in the fabrication and design of ytterbium doped fibers made it possible to scale the output power of such MOPA systems in excess of one kilowatt output power [Jeo04, IPG11]. Usually, those MOPA systems produce an output with a broad spectra of 10 nm. Being available in lengths of tens of meters at various doping concentrations, fiber amplifiers offer a very high single pass gain. Because of their rather small internal structures (usually the fiber core has a diameter of 5 to 25 μm), nonlinear effects have to be considered with increasing output power levels. The main limiting effect for the amplification of narrow linewidth sources is the *Stimulated Brillouin Scattering* (SBS), which is the scattering of the seed light by acoustic phonons in backward direction. As the onset of SBS results in a chaotic state of operation, which is usually accompanied by a destruction of the amplifiers fiber itself, the output power of standard-fiber-based MOPA systems is currently limited to approximately 200 W.

As the SBS threshold depends on the mode volume and the amplification length, larger core diameters and higher doping concentrations to reduce the fiber length are desired. In general, the fundamental beam profile of the seed laser is preserved during the amplification process by the optical guiding effect inside the fibers core. Unfortunately, the losses for higher-order modes within the signal core are reduced with increasing core diameter. Thus, the beam quality of the amplified seed would be negatively affected passing through those fibers. To suppress higher-order modes and to enhance the threshold for SBS, new core structures were developed in recent years. One approach to control the SBS and the losses for higher-order modes whilst increasing the signal core diameter is to incorporate photonic band-gap structures into the fiber's lattice, resulting in so-called *photonic crystal fibers*. A second approach utilizes a classical refractive index step profile structure, but with an alumina (Al_2O_3) and germania (GeO_2) doping of the core to create simultaneously an optical waveguide and a acoustic anti-guide. With this fiber, it was possible to amplify a seed source with a linewidth of 3 kHz to an output power of 502 W in a bidirectional pump configuration [Gra07]. As an example for such a fiber based MOPA system, a schematic of the laboratory setup used by Gray et al. is given in Fig. 6.4.
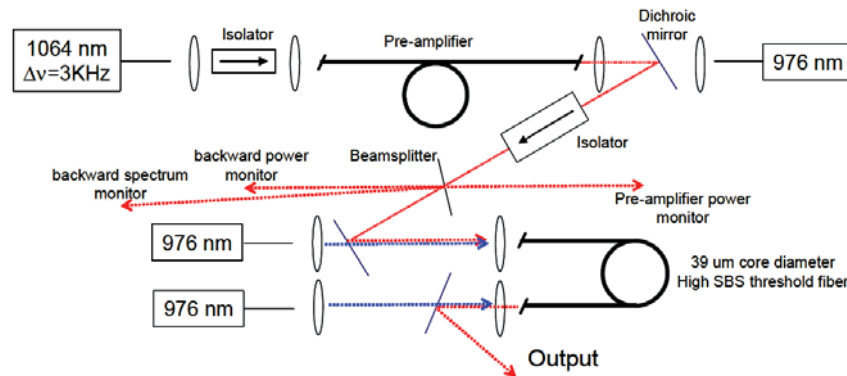
Figure 6.4: Schematic of the two stage amplifier system with high SBS threshold fiber (core diameter: 39 μm, hexagonal inner cladding: 420 μm, outer cladding: 520 μm, core numerical aperture (NA): 0.05 and inner cladding NA: 0.30). The 100 mW of output power from the fiber laser source was increased by a pre-amplifier based on a standard active fiber to 5 W. The two fiber coupled diode lasers have a maximum output power of 400 W each and a center wavelength of 976 nm [Gra07].

In such high power experiments, double-clad fiber structures were used in which the pump light propagates in a larger diameter second core that surround the signal core. The numerical aperture (NA) of this inner cladding is maximized to guarantee a low loss coupling of the supplied pump light. Nevertheless, high intensities are generated, when pump light with a power level of several hundred watts is injected into a core of approx. 400–500 μm diameter. In fact, the heat generated at the fiber tips, the appearance of parasitic laser oscillations, and the appearance of SBS limits the durability of small linewidth fiber MOPAs to a continuous operation of a few hours only. To use such MOPA systems in the third generation of GWD, the durability of such large-mode-area fiber amplifiers will have to be significantly improved to last for months or even years without failure.

In contrast to fiber based MOPAs, solid-state amplifiers have a higher reliability. Unfortunately, the achievable single pass gain of such systems is significantly lower, because of the reduced interaction length in comparison with a fiber. Nevertheless, new approaches were studied to validate the suitability of solid-state Nd:YAG amplifiers for use in next generation GWDs. For this purpose, an amplifier setup with two identical laser crystals (0.3 at.% doped Nd:YAG with a length of 120 mm and a diameter of 4.5 mm) was developed by the company neoLASE GmbH and acquired by LZH. The thermally induced birefringence was compensated by a standard birefringence compensation scheme, whose feasibility was already demonstrated in the Advanced LIGO high power oscillator. To scale the output power of such an amplifier system towards the kilowatt regime, an enhancement of the applicable pump power per laser crystal had to be engineered.

Two polarization coupled laser diode stacks with a maximum output power of 600 W each were used to pump the Nd:YAG crystal. The combined pump light was then homogenized by a glass rod, ground to an hexagonal shape for better mode mixing performance. To image the light emerging from the homogenizer tip through the undoped end-cap of the laser crystal, a pair of lenses was used, one of which has an aspherical shape. A highly reflective coating was applied to the back of the Nd:YAG crystal for double passing the pump light. In contrast to the setup of the laser head modules used in the Advanced LIGO high power oscillator, the center pump wavelength was chosen to be at 802 nm, where Nd:YAG has a low absorption coefficient. To achieve an absorption of 90 % of the incident pump light, an optimal doping concentration of 0.3 at.% and an overall length (including two times 10 mm end-caps) of 120 mm was determined. A schematic overview of the optical layout of one laser crystal including the pump light source and optics is presented in Fig. 6.5.
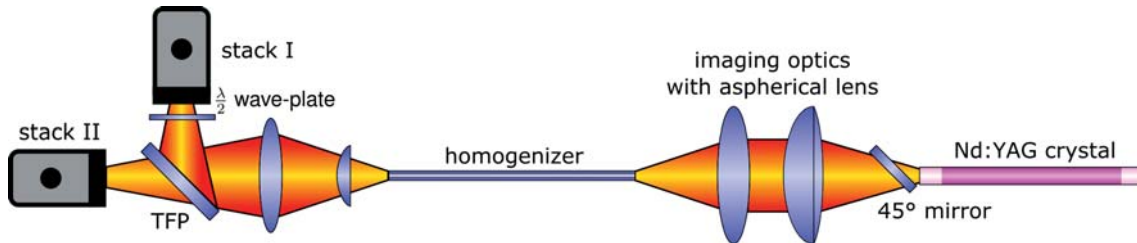
Figure 6.5: Optical layout of one of the high power stack pumped Nd:YAG crystals.

First experiments carried out in a two head laser configuration showed a linearly polarized output power of approximately 145 W in a fundamental mode intensity profile at a total pump power of 1 kW. However, the pump intensity distribution does not have a Gaussian shape at all, but can be better described by a flat-top distribution. This resulted in an almost spherical thermal lens. As a consequence, higher-order modes start oscillating virtually at the same zone of stability as the fundamental mode, making it difficult to discriminate them by appropriate choice of the resonator lengths.

In an early single pass amplifier experiment, an output power of 242 W at a total pump power of 1 kW was obtained. To saturate the amplifier, the output beam of one of the prototpye Advanced LIGO lasers was used as a seed source. The maximum achievable seed power during this experiment was 156 W in a fundamental mode beam profile. In future experiments, a power scaling by multiple passing of the laser crystals combined with an increase of pump power will be investigated. Moreover, a detailed analysis of the higher-order mode content will be performed. In a second

step, wave front distortions induced by the thermal lenses inside the laser crystal will be investigated with a wave-front detector.

6.2.2 Laser at 1550 nm

For the use of test masses made of silicon in future GWDs, a single-frequency laser source with a fundamental beam profile with a center wavelength at 1550 nm is required. Even though an implementation of such a laser system based on solid-state laser technology would be achievable, the poor efficiency and outdated available technology constrained further investigations in this field. All currently available light sources at 1550 nm that can be considered as a potential source for the third generation GWDs rely on fiber technology. Based on a typical MOPA scheme, two different types of fibers have a high potential to meet the requirements given by a next generation GWD.

In general, erbium doped fibers are used for the amplification of a small linewidth seed source with a center wavelength around 1550 nm. Either frequency stabilized diode lasers with a typical linewidth of a few megahertz or Bragg grating stabilized fiber ring lasers with a linewidth of a few kilohertz are used as a seed source. Most of these lasers can deliver output power levels of some tens of milliwatts only. Thus, a pre-amplifier, usually based on single-mode Er-doped standard telecommunication fiber, is included in each setup.

Compared with Yb-doped fibers, Er-doped fibers have a rather low absorption cross-section at wavelengths around 980 nm. Furthermore, the quantum defect of Er-doped fibers is significantly higher (at least 37 % of the incident pump power will be transferred in heat) than the one for Yb-doped MOPAs. To overcome these constraints one could resonantly pump at wavelengths between 1480 nm and 1530 nm. Unfortunately, only low power pump sources are commercially available in this wavelength regime. Thus, methods for efficient pumping at 980 nm had to be found.

One way to increase the absorption of Er-fibers is to co-dope the signal core with ytterbium. Pump light, which is absorbed by the Yb-ions is then transferred via a cross-relaxation process to the upper laser level of the Er-ions. With this technique, an output power of 151 W was demonstrated [Jeo05]. However, these Yb-co-doped fiber MOPAs are limited by the onset of parasitic amplified spontaneous emission (ASE) from the Yb^{3+} ions, which significantly reduces the life-time of the system. Although several schemes to control the onset of the parasitic 1 μm radiation are available [Yus05, Mor07, Shi08, Kuh09], these techniques either limit the power scalability or increase the complexity and cost of such MOPA systems.
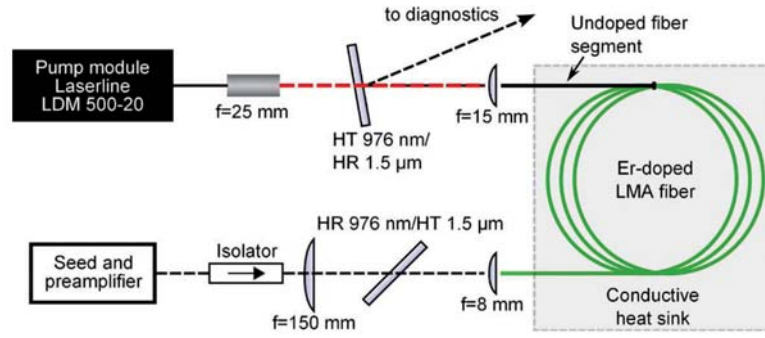
Figure 6.6: Optical layout of the Yb-free fiber MOPA. **Black:** seed and signal radiation. **Red:** pump radiation [Kuh11]©2011 IEEE.

In Fig. 6.6, a large-mode area fiber amplifier developed by Kuhn et al. is shown. With this laboratory table top experiment it was possible to demonstrate an output power of 67 W for an Yb-free fiber pumped at a wavelength of 976 nm [Kuh11]. At an absorbed pump power of 250 W the onset of parasitic laser oscillations was detected. The launching efficiency from the fiber coupled pump light module (Laserline LDM 500-20 with a 200 μm multimode fiber with NA 0.22) into the double-clad fiber was 60 %. Thus, an effective cooling scheme had to be implemented into the setup. For this purpose an undoped fiber segment was spliced to the end of the active fiber, which was embedded in thermally conductive paste and mounted on a conductive heat sink. With this configuration, the cladding temperature of the pumped fiber could be kept below the damage threshold temperature of the low index polymer coating for all launched pump power levels.

Even though the output power of Er-fiber MOPAs is adequate for GWDs, the mode content, frequency and amplitude stability have to be studied and improved in future experiments. First comparisons of different fiber MOPAs in respect to their mode content have been performed by Kuhn et al. using a passive pre-mode cleaner cavity as a modal analysis tool [Kuh10]. During these experiments, a TEM_{00} mode content of 82% at an output power of 20 W was measured.

In summary, MOPA systems for the amplification of low power seed lasers to the desired output power regime have a high potential as light sources for the third generation of gravitational wave detectors. Even though the experimental basis to achieve the required output power levels have been demonstrated, a lot of technological issues are not yet solved. To find solutions for those technological limitations and to improve the laser system's reliability and output beam characteristics will be the focus of future work in this field.

Chapter 7

Conclusion

For the scientific community, a detection of a gravitational wave would be a major break-through, but for the future, a daily observation of astrophysical objects emitting these waves is desired. For that purpose, the sensitivity of today's ground-based GWDs will be improved by an upgrade of its internal subcomponents. One major component of the large scale interferometer of the LIGO detector to be upgraded is the pre-stabilized laser.

The development of the main component of this laser, the injection-locked high power oscillator, was described in this thesis. Starting from preliminary results, based on preliminary laboratory table-top experiments, a complete laser concept was established, which has fulfilled the free-running final design requirements of the LIGO community and was therefore chosen as light source for the next generation GWD.

During the development of the Advanced LIGO high power oscillator, general strategies to discriminate higher-order modes by appropriate resonator design were established. Carefully setting the lengths of an asymmetric laser resonator, the output power within the fundamental mode beam could be scaled with increasing pump power. With the derived guidelines for resonator design, a high power ring laser with four Nd:YAG crystals was made, delivering an output power of 172 W in a fundamental mode beam. In a subsequent step, this ring laser was injection-locked to a low power MOPA system (35 W output power), resulting in a total single-frequency output power of more than 220 W.

For a long term stable low noise operation of the injection locked laser, all optical and mechanical parts within the high power oscillator were evaluated, designed, and optimized. The result was a modular system, which can be easily fabricated and maintained, but that was sufficiently rugged to survive transportation to the GWD's location without any harm. Based on the results of FEM thermal analysis

of the mechanical structures, a water cooling scheme was incorporated into the laser to reduce the heat load of the components and thus increase the life-time and reliability of the laser. The effectiveness of this cooling scheme could be demonstrated by comparing thermal measurements of the structure with computationally derived temperature values of the mechanical components. Furthermore, a slow actuator was included into the laser setup for decoupling the environmental length variations of the resonator to the injection-locked output performance. This scheme for a long term expansion compensation proved feasible in laboratory experiments and during long term operation of the laser system at various locations.

Before a laser is delivered to the Advanced LIGO observatory for installation, a full characterization of its output performance was carried out. In the experimental results chapter of this thesis, the results obtained during such a characterization were presented. It was demonstrated that the laser system fulfills the given requirements on its free-running frequency and relative power noise. Furthermore, the measured output power in a pure TEM_{00} mode exceeded the requirements of 165 W, which is the highest reported power in a filtered fundamental mode beam to my knowledge. For completeness of the characterization, first results for the stabilized Advanced LIGO high power laser were presented. Even though the desired design requirements with respect to the active stabilization were not yet satisfied, one is confident to solve the remaining technological challenges during the installation at the different observatory sites.

It is a fact that the assembly of the Advanced LIGO detector will not be completed in a few years. Nevertheless, scientists in various groups have started to work on new concepts to further improve the sensitivity of advanced GWDs. As an example, the Einstein Telescope was presented and their need for high power laser systems with wavelengths at 1064 nm and 1550 nm was discussed. To achieve an output power of a kilowatt for radiation with a wavelength of 1064 nm, fiber and solid-state MOPAs are the most promising approaches, to date. However, even though the actual results look very promising, none of the presented systems have reached the long term stability of the Advanced LIGO laser presented in this work, so far.

If successful, the Advanced LIGO interferometers will be the most sensitive instruments for the detection of GWs for years. Hopefully, the detection of a GW will enable us to obtain a more detailed view of our Universe and thus of its origin.

Appendix A

Material properties

The data of the presented materials was taken from Matweb [Mat].

MACOR - machinable ceramic - Corning

Mechanical	
Density	2.52 g/cm^3
Young's Modulus	66.9 GPa
Poisson's Ratio	0.29
Shear Modulus	25.5 GPa
Flexure Strength	94 MPa
Compressive Strength	345 MPa

Thermal	
Expansion Coefficient for:	
-200 °C to 25 °C	$7.4 \cdot 10^{-6}/K$
25 °C to 300 °C	$9.3 \cdot 10^{-6}/K$
25 °C to 600 °C	$11.4 \cdot 10^{-6}/K$
25 °C to 800 °C	$12.6 \cdot 10^{-6}/K$
Specific Heat (25 °C)	0.79kJ/kg·C
Thermal Conductivity (25 °C)	1.46W/m·K

Optical	
Reflectivity at 800 nm [Kra94]	75 %

INVAR 36 - 36 % nickel-iron low expansion alloy

Mechanical	
Density	8.05 g/cm^3
Young's Modulus	137 GPa
Shear Modulus	54.0 GPa
Poisson's Ratio	0.280
Yield Strength	483 MPa
Tensile Strength	621 MPa
Failure Strain	20 %
Thermal	
Expansion Coefficient for:	
0 °C to 100 °C	$1.3 \cdot 10^{-6}/K$
0 °C to 260 °C	$4.18 \cdot 10^{-6}/K$
0 °C to 371 °C	$7.60 \cdot 10^{-6}/K$
Specific Heat (20 °C)	0.515kJ/kg·C
Thermal Conductivity (20 °C)	10.15W/m·K

Stainless steel 304 - X5CrNi18-10 - DIN 1.4301

Mechanical	
Density	8.0 g/cm^3
Young's Modulus	200 GPa
Shear Modulus	86.0 GPa
Poisson's Ratio	0.290
Yield Strength	215 MPa
Tensile Strength	505 MPa
Failure Strain	70 %

Thermal	
Expansion Coefficient for:	
0 °C to 100 °C	$17.3 \cdot 10^{-6}/K$
0 °C to 315 °C	$17.8 \cdot 10^{-6}/K$
0 °C to 650 °C	$18.7 \cdot 10^{-6}/K$
Specific Heat (20 °C)	0.5kJ/kg·C
Thermal Conductivity (20 °C)	16.2W/m·K

Stainless steel 420 - X20Cr13 - DIN 1.4021

Mechanical	
Density	7.7 g/cm^3
Young's Modulus	200 GPa
Shear Modulus	80.7 GPa
Poisson's Ratio	0.240
Yield Strength	680 MPa
Tensile Strength	830 MPa
Failure Strain	16 %

Thermal	
Expansion Coefficient for:	
0 °C to 100 °C	$10.3 \cdot 10^{-6}/K$
0 °C to 100 °C	$10.5 \cdot 10^{-6}/K$
0 °C to 200 °C	$11.0 \cdot 10^{-6}/K$
0 °C to 300 °C	$11.5 \cdot 10^{-6}/K$
0 °C to 400 °C	$12.0 \cdot 10^{-6}/K$
Specific Heat (20 °C)	0.460kJ/kg·C
Thermal Conductivity (20 °C)	30W/m·K

Stainless steel 430 - X6Cr17 - DIN 1.4016

Mechanical	
Density	7.7 g/cm^3
Young's Modulus	200 GPa
Shear Modulus	86.0 GPa
Poisson's Ratio	0.290
Yield Strength	300 MPa
Tensile Strength	480 MPa
Failure Strain	28 %

Thermal	
Expansion Coefficient for:	
0 °C to 100 °C	$10.4 \cdot 10^{-6}/K$
0 °C to 100 °C	$10.0 \cdot 10^{-6}/K$
0 °C to 200 °C	$10.0 \cdot 10^{-6}/K$
0 °C to 300 °C	$10.5 \cdot 10^{-6}/K$
0 °C to 300 °C	$11.0 \cdot 10^{-6}/K$
Specific Heat (20 °C)	0.460kJ/kg·C
Thermal Conductivity (20 °C)	25W/m·K

Stainless steel - X3CrNiMo13-4 - DIN 1.4313

Mechanical	
Density	7.7 g/cm^3
Young's Modulus	206 GPa
Shear Modulus	80.0 GPa
Poisson's Ratio	0.288
Yield Strength	690 MPa
Tensile Strength	760 MPa
Failure Strain	20 %

Thermal	
Expansion Coefficient for:	
20 °C to 100 °C	$10.5 \cdot 10^{-6}/K$
20 °C to 200 °C	$10.9 \cdot 10^{-6}/K$
20 °C to 300 °C	$11.3 \cdot 10^{-6}/K$
20 °C to 400 °C	$11.6 \cdot 10^{-6}/K$
Specific Heat (20 °C)	0.430kJ/kg·C
Thermal Conductivity (20 °C)	25W/m·K

High-tensile aluminum alloy - EN AW 7075 - DIN 3.4365 - AlZnMgCu1.5

Mechanical	
Density	2.8 g/cm^3
Young's Modulus	71 GPa
Shear Modulus	26.9 GPa
Poisson's Ratio	0.33
Yield Strength	462 MPa
Tensile Strength	533 MPa
Failure Strain	8.5 %

Thermal	
Expansion Coefficient for:	
20 °C to 100 °C	$23.4 \cdot 10^{-6}/K$
Specific Heat (20 °C)	0.862kJ/kg·C
Thermal Conductivity (20 °C)	130W/m·K

Free-cutting brass - UNS C36000

Mechanical	
Density	8.49 g/cm^3
Young's Modulus	97 GPa
Shear Modulus	37.0 GPa
Poisson's Ratio	0.310
Yield Strength	310 MPa
Tensile Strength	469 MPa
Failure Strain	53.0 %

Thermal	
Expansion Coefficient for:	
20 °C to 300 °C	$20.5 \cdot 10^{-6}/K$
Specific Heat (20 °C)	0.380kJ/kg·C
Thermal Conductivity (20 °C)	115W/m·K

Electrolytically refined copper - ECU 2.0060 - CW004A

Mechanical	
Density	8.93 g/cm^3
Young's Modulus	110 GPa
Shear Modulus	46.0 GPa
Poisson's Ratio	0.350
Yield Strength	120 MPa
Tensile Strength	200 MPa
Failure Strain	35.0 %

Thermal	
Expansion Coefficient for:	
20 °C to 100 °C	$16.7 \cdot 10^{-6}/K$
20 °C to 100 °C	$16.4 \cdot 10^{-6}/K$
20 °C to 250 °C	$18.5 \cdot 10^{-6}/K$
20 °C to 500 °C	$20.2 \cdot 10^{-6}/K$
20 °C to 925 °C	$24.8 \cdot 10^{-6}/K$
Specific Heat (20 °C)	0.385kJ/kg·C
Thermal Conductivity (20 °C)	385W/m·K

Fused silica glass - SiO_2

Mechanical	
Density	2.2 g/cm^3
Young's Modulus	73 GPa
Shear Modulus	31.0 GPa
Poisson's Ratio	0.170
Compressive Strength	1108 MPa
Thermal	
Expansion Coefficient for:	
20 °C to 100 °C	$0.55 \cdot 10^{-6}/K$
Specific Heat (20 °C)	0.74kJ/kg·C
Thermal Conductivity (20 °C)	1.38W/m·K

Nd:YAG doping 0.2-1.4 at.% - $Y_{3-X}Nd_XAl_5O_{12}$

Mechanical	
Density	4.55 g/cm^3
Young's Modulus for (111) cut	300 GPa
Poisson's Ratio	0.25
Tensile Strength	280 MPa
Thermal	
Expansion Coefficient for:	
(111) cut crystal	$7.8 \cdot 10^{-6}/K$
Specific Heat (20 °C)	0.59kJ/kg·C
Thermal Conductivity (20 °C)	13W/m·K

Polytetrafluoroethylene - PTFE

Mechanical	
Density	2.15 g/cm^3
Young's Modulus	904 GPa
Poisson's Ratio	0.46
Yield Strength	11 MPa
Tensile Strength	26 MPa
Failure Strain	≈ 300.0 %
Thermal	
Expansion Coefficient for:	
-100 °C to 0 °C	$86.0 \cdot 10^{-6}/K$
0 °C to 20 °C	$\approx 114.5 \cdot 10^{-6}/K$
20 °C to 100 °C	$\approx 155 \cdot 10^{-6}/K$
100 °C to 250 °C	$\approx 195 \cdot 10^{-6}/K$
Specific Heat (20 °C)	1.3kJ/kg·C
Thermal Conductivity (20 °C)	0.3W/m·K

Thermal conductivity of air

The heat transfer coefficient of laminar flowing air can be approximated by the following rule of thumb

$$\lambda_{air} = 2 + 12 \cdot V^{0.5}, \tag{A.1}$$

where V is the speed of the laminar air flow in ms^{-1}. Inside the clean room used during development and assembly of the laser system an air flow rate of 0.5ms^{-1} was present.

Appendix B

Rod designer program interface

For the optimization of end-pumped diode laser systems, various pump spot configurations have to be tested. Thus a large number of different pump light distributions and resulting temperature profiles has to be simulated. Even with the recent increases in computing speed and power, which has enabled even more complex FEM simulations and higher element numbers, the analysis of a pumped laser crystal via the ANSYS software is a time consuming process in scales up to several hours. To shorten this process, a software called Rod Designer was developed by Wilhelm et al. [Wil09].

With this software, a numerical *Fourier-Bessel* approach is used to solve the stationary heat equation in a cylindrically symmetric geometry. This approach eliminates the need for extensive computational calculations, while taking the axial heat transport and the temperature dependent material properties into account.

Even though the Rod Designer software requires the same parameter set needed for the simulation of the temperature and stress/strain distribution, it has some internal calculation restrictions:

- The incident pump light profile is approximated by an algebraic function within the algorithm. This function is defined by a Gaussian profile with and without a background, a parabolic distribution with and without a background, or a top-hat profile within the user interface of the software. The FWHM and height of the background has to be chosen, so that the created function has the best approximation to the real pump light profile.

- The propagation of the pump light inside the laser crystal rod is neglected. To compensate for this simplification of the algorithm, one has to take the beam parameters of the integrated pump light profile inside the laser crystal rod instead of the pump spot dimensions into account. These values can be either

calculated using ray tracing software or they are experimentally determined by a measurement of the rod's internal fluorescence profile.

- The boundary conditions that are defined by the heat transfer coefficient are limited to a constant value over the full length of the crystal.

- The doping concentration of a laser crystal can be split in different regions. This feature is necessary to compute results for multi-segmented laser crystals. Unfortunately, it is not possible to introduce a doping gradient to one of the segments.
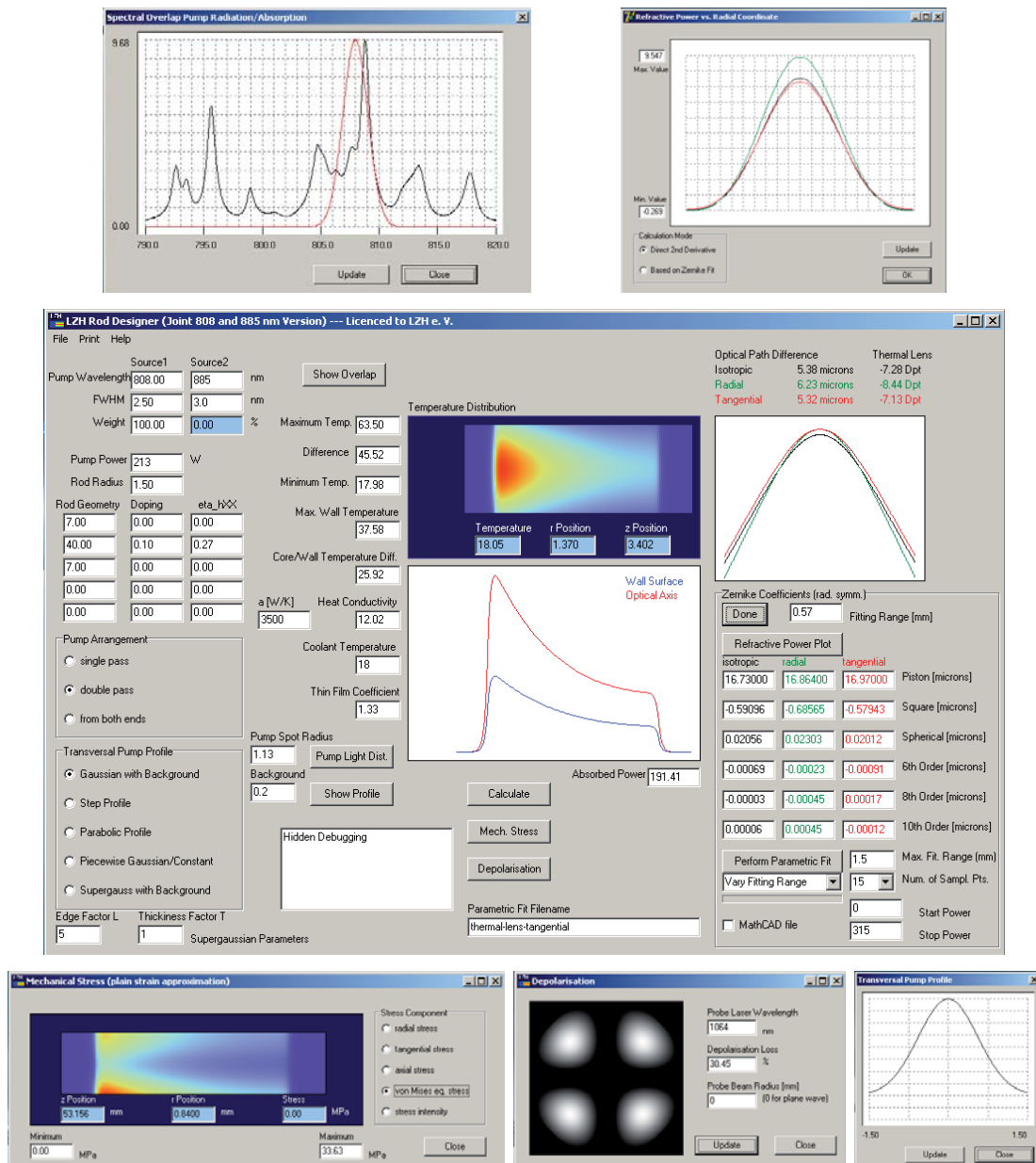

Figure B.1: Rod designer software interface.

Appendix C

Stress and strain coefficients

Empirical formula for the thermal expansion coefficient (T as numerical value in K) [Fan98]

$$\alpha(T) = -1.78 \cdot 10^{-6} + 3.3 \cdot 10^{-8} \cdot T \tag{C.1}$$

Empirical formula for the temperature dependent refractive index change (T as numerical value in K) [Bro98a]

$$\frac{dn}{dT}(T) = -2.59 \cdot 10^{-6} + 2.61 \cdot 10^{-8} \cdot T + 6.02 \cdot 10^{-11} \cdot T^2 \tag{C.2}$$

Constants involving Poisson's ratio ν and the photo-elastic coefficients p_{ij} [Bro98b]

$$C_r = \frac{(17\nu - 7)p_{11} + (31\nu - 17)p_{12} + 8(\nu + 1)p_{44}}{48(\nu - 1)}, \tag{C.3}$$

for the radial constant, and

$$C_t = \frac{(10\nu - 6)p_{11} + 2(11\nu - 5)p_{12}}{32(\nu - 1)}, \tag{C.4}$$

for the tangential constant with the values for p_{ij} for a [111] cut crystal:

$$
\begin{array}{ll}
p_{11} = -0.07145 & p_{12} = +0.02325 \\
p_{13} = +0.03740 & p_{33} = -0.08560 \\
p_{44} = -0.03320 & p_{66} = -0.04735 \\
p_{14} = -0.02\cos(3\Phi) & p_{15} = -0.02\sin(3\Phi)
\end{array}
$$

Table C.1: Table of p_{ij} taken from Refs. [Bro98a, Lü95b], with Φ being the angle from the x-axis of the crystal.

Appendix D

SPC laser control visualization

In the following an overview of the laser control software user interface is given. This interface can be accessed from the inside of the laser enclosure using a virtual network computing connection (VNC) for remote control of the laser.
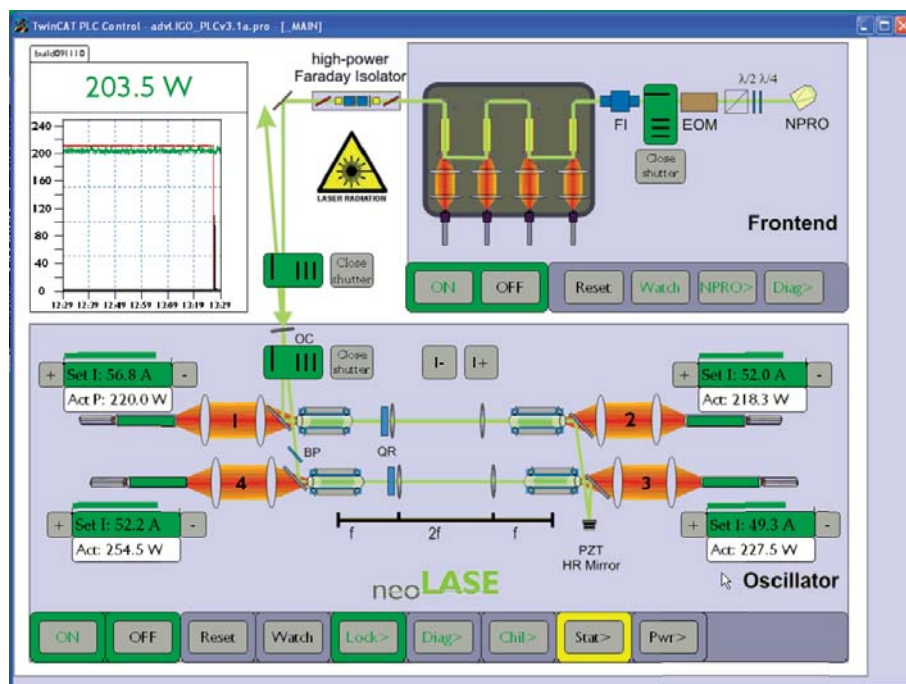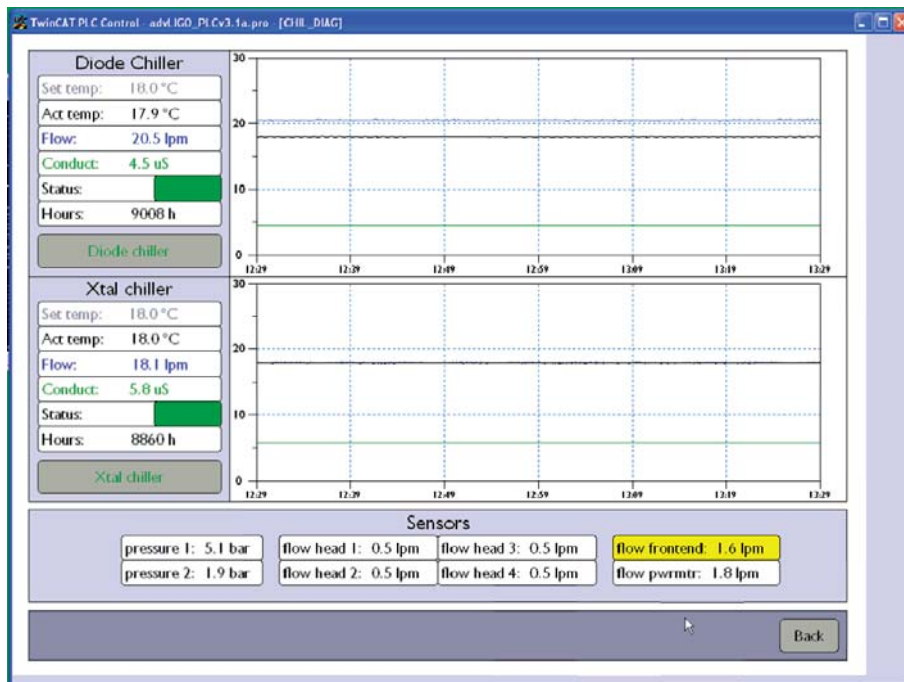

Figure D.1: Main control screen.
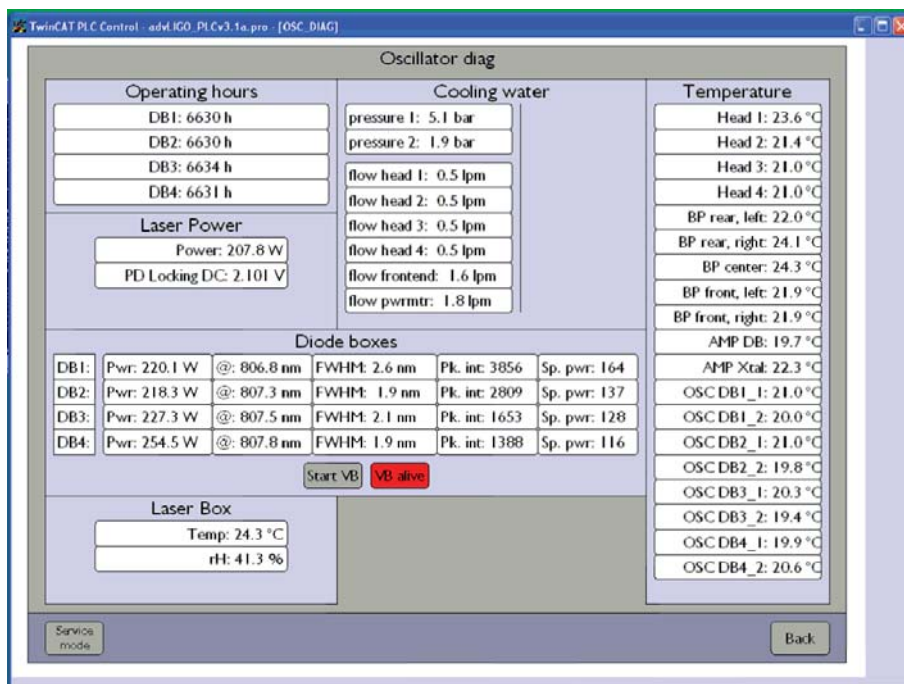
Figure D.2: Chiller control screen.
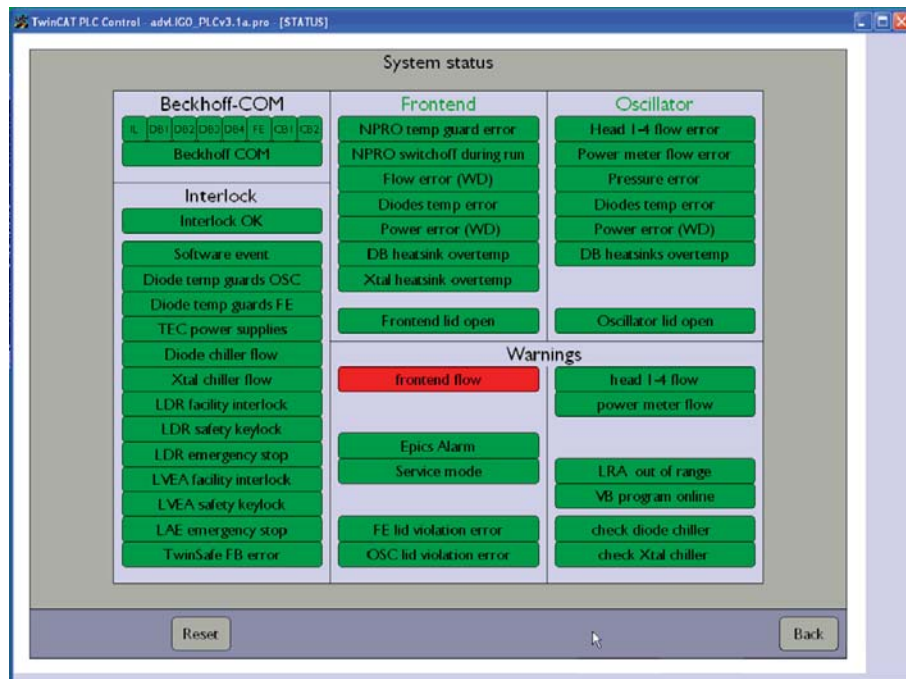

Figure D.3: Diagnostics screen.

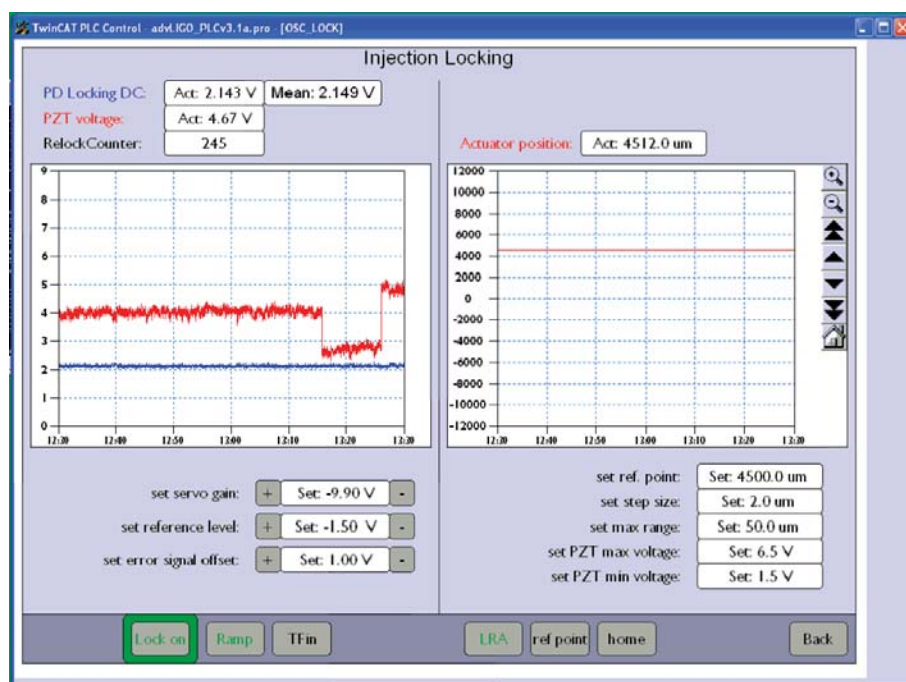Figure D.4: Laser status screen.

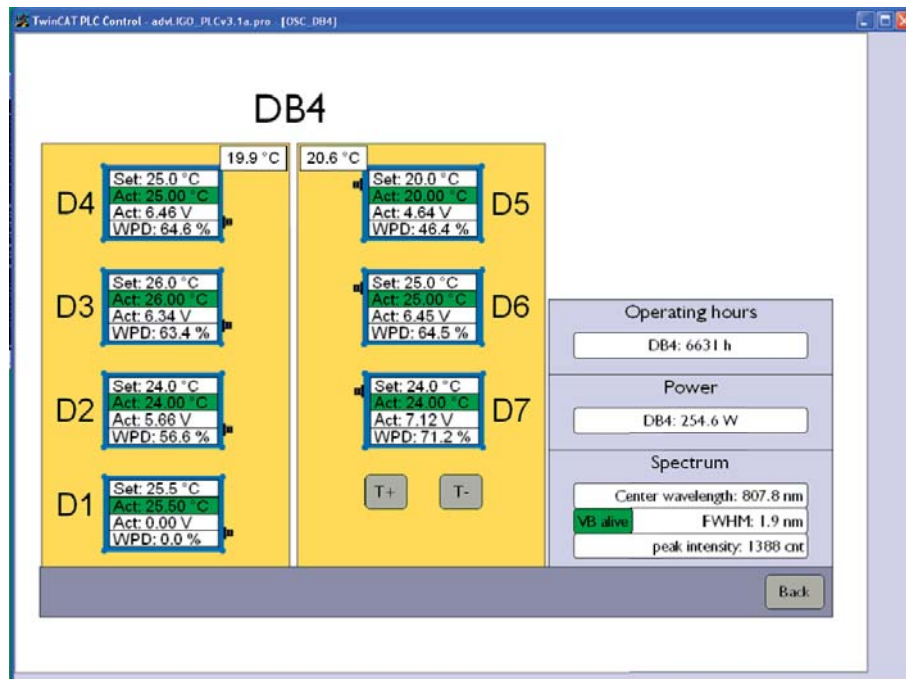Figure D.5: Injection locking and LRA control screen.

Figure D.6: Laser diode box control screen.

References

[Abb09] B. Abbott, R. Abbott, R. Adhikari et al. *LIGO: The laser interferometer gravitational-wave observatory.* Reports on Progress in Physics, Vol. 72, (2009) 076901.

[Ace08] F. Acernese, P. Amico, M. Alshourbagy et al. *The Virgo 3 km interferometer for gravitational wave detection.* Journal of Optics A: Pure and Applied Optics, Vol. 10, No. 6, (2008) 064009.

[Adl46] R. Adler. *A Study of Locking Phenomena in Oscillators.* Proceedings of the IRE, Vol. 34, No. 6, (1946) 351–357.

[And05] M. Ando and the TAMA Collaboration. *Current status of the TAMA300 gravitational-wave detector.* Classical and Quantum Gravity, Vol. 22, No. 18, (2005) S881.

[Apf82] J. Apfel. *Phase retardance of periodic multilayer mirrors.* Applied Optics, Vol. 21, No. 4, (1982) 733–738.

[Ast97] P. Astone, M. Bassan, P. Bonifazi et al. *The gravitational wave detector NAUTILUS operating at T = 0.1 K.* Astroparticle Physics, Vol. 7, No. 3, (1997) 231–243.

[Bec11] Beckhoff Automation GmbH. *More information found at `http://www.beckhoff.com`* (2011).

[Bir93] K. P. Birch and M. J. Downs. *An Updated Edlén Equation for the Refractive Index of Air.* Metrologia, Vol. 30, No. 3, (1993) 155.

[Bir94] K. P. Birch and M. J. Downs. *Correction to the Updated Edlén Equation for the Refractive Index of Air.* Metrologia, Vol. 31, No. 4, (1994) 315.

[Bla01] E. Black. *An introduction to Pound–Drever–Hall laser frequency stabilization.* American Journal of Physics, Vol. 69, (2001) 79–87.

[Bro98a] D. Brown. *Heat, fluorescence, and stimulated-emission power densities and fractions in Nd:YAG.* IEEE Journal of Quantum Electronics, Vol. 34, No. 3, (1998) 560–572.

[Bro98b] D. Brown. *Nonlinear thermal distortion in YAG rod amplifiers.* IEEE Journal of Quantum Electronics, Vol. 34, No. 12, (1998) 2383 –2392.

[Cla99] W. A. Clarkson, N. S. Felgate, and D. C. Hanna. *Simple method for reducing the depolarization loss resulting from thermally induced birefringence in solid-state lasers.* Optics Letters., Vol. 24, No. 12, (1999) 820–822.

[Cla01] W. A. Clarkson. *Thermal effects and their mitigation in end-pumped solid-state lasers.* Journal of Physics D: Applied Physics, Vol. 34, No. 16, (2001) 2381.

[Cou92] A. Cousins. *Temperature and thermal stress scaling in finite-length end-pumped laser rods.* IEEE Journal of Quantum Electronics, Vol. 28, No. 4, (1992) 1057–1069.

[Dre83] R. Drever, J. Hall, F. Kowalski et al. *Laser phase and frequency stabilization using an optical resonator.* Applied Physics B: Lasers and Optics, Vol. 31, No. 2, (1983) 97–105.

[Edl66] B. Edlen. *The refractive index of air.* Metrologia, Vol. 2, (1966) 71.

[Ein15] A. Einstein. *Erklärung der Perihelbewegung des Merkur aus der allgemeinen Relativitätstheorie.* Albert Einstein: Akademie-Vorträge, 78–87.

[Ein16] A. Einstein. *Näherungsweise Integration der Feldgleichungen der Gravitation.* Albert Einstein: Akademie-Vorträge, 99–108.

[Fan93] T. Fan. *Heat generation in Nd:YAG and Yb:YAG.* IEEE Journal of Quantum Electronics, Vol. 29, No. 6, (1993) 1457–1459.

[Fan98] T. Y. Fan and J. L. Daneu. *Thermal Coefficients of the Optical Path Length and Refractive Index in YAG.* Applied Optics, Vol. 37, No. 9, (1998) 1635–1637.

[Far88] U. Farrukh, A. Buoncristiani, and C. Byvik. *An analysis of the temperature distribution in finite solid-state laser rods.* IEEE Journal of Quantum Electronics, Vol. 24, No. 11, (1988) 2253–2263.

[For78] R. Forward. *Wideband laser-interferometer graviational-radiation experiment.* Physical Review D, Vol. 17, No. 2, (1978) 379–390.

[Fre04] M. Frede, R. Wilhelm, M. Brendel et al. *High power fundamental mode Nd:YAG laser with efficient birefringence compensation.* Optics Express, Vol. 12, No. 15, (2004) 3581–3589.

[Fre05a] M. Frede, P. King, R. Savage et al. *Advanced LIGO Pre-stabilized Laser Conceptual Design Document.* LIGO Technical Document, Vol. T050035-02-D, available at `http://www.ligo.caltech.edu/docs/T/T050035-02/T050035-02.pdf`.

[Fre05b] M. Frede, R. Wilhelm, D. Kracht et al. *195 W injection-locked single-frequency laser system.* In *Conference on Lasers and Electro-Optics, Baltimore, MD.* (2005).

[Fre05c] M. Frede, R. Wilhelm, D. Kracht et al. *Nd:YAG ring laser with 213 W linearly polarized fundamental mode output power.* Optics Express, Vol. 13, No. 19, (2005) 7516–7519.

[Fre07a] M. Frede. *Einfrequentes Laserlicht höchster Brillianz.* Dissertation, Leibniz Universität Hannover (2007).

[Fre07b] M. Frede, B. Schulz, R. Wilhelm et al. *Fundamental mode, single-frequency laser amplifier for gravitational wave detectors.* Optics Express, Vol. 15, No. 2, (2007) 459–465.

[Fri08] P. Fritschel. *Advanced LIGO system design.* LIGO Technical document, LIGO-T010075-01-I, available at `http://www.ligo.caltech.edu/docs/T/T010075-01.pdf`.

[Gau03] R. Gau. *Entwicklung und Charakterisierung eines Pumplichtsystems für endgepumpte, doppelbrechungskompensierte Nd:YAG Hochleistungs-Laser hoher Strahlqualität* (2003).

[Gol03] D. H. Goldstein and E. Collett. *Polarized light* (Marcel Dekker Inc, 2003).

[Gra07] S. Gray, A. Liu, D. T. Walton et al. *502 Watt, single transverse mode, narrow linewidth, bidirectionally pumped Yb-doped fiber amplifier.* Optics Express, Vol. 15, No. 25, (2007) 17044–17050.

[Har10] G. Harry et al. *Advanced LIGO: the next generation of gravitational wave detectors.* Classical and Quantum Gravity, Vol. 27, (2010) 084006.

[Hei98] G. Heinzel, K. A. Strain, J. Mizuno et al. *Experimental Demonstration of a Suspended Dual Recycling Interferometer for Gravitational Wave Detection.* Phys. Rev. Letters., Vol. 81, (1998) 5493–5496.

[Hil08] S. Hild, S. Chelkowski, and A. Freise. *Pushing towards the ET sensitivity using 'conventional' technology.* arXiv:0810.0604v2.

[Hil11] S. Hild, M. Abernathy, F. Acernese et al. *Sensitivity studies for third-generation gravitational wave observatories.* Classical and Quantum Gravity, Vol. 28, No. 9, (2011) 094013.

[Hsü63] S. Hsü. *Engineering heat transfer* (Van Nostrand, 1963).

[Hul75] R. Hulse and J. Taylor. *Discovery of a pulsar in a binary system.* The Astrophysical Journal, Vol. 195, (1975) L51–L53.

[Inn90] M. Innocenzi, H. Yura, C. Fincher et al. *Thermal modeling of continuous-wave end-pumped solid-state lasers.* Applied Physics Letters, Vol. 56, (1990) 1831.

[Inn11] InnoLight. *Mephisto Product Sheet* `http://www.innolight.de/pdf/mephisto_und_mephisto_s.pdf` (2011).

[IPG11] IPG Photonics Corporation. *Information from* `http://www.ipgphotonics.com` (2011).

[Jen10] Jenoptik AG. Fiber-Coupled Diode Laser JOLD-45-CPXF-1L *datasheet available at* `http://www.jenoptik.com/` (2010).

[Jeo04] Y. Jeong, J. Sahu, D. Payne et al. *Ytterbium-doped large-core fiber laser with 1.36 kW continuous-wave output power.* Optics Express, Vol. 12, No. 25, (2004) 6088–6092.

[Jeo05] Y. Jeong, J. K. Sahu, D. B. S. Soh et al. *High-power tunable single-frequency single-mode erbium:ytterbium codoped large-core fiber master-oscillator power amplifier source.* Optics Letters, Vol. 30, No. 22, (2005) 2997–2999.

[Kan85] T. Kane and R. Byer. *Monolithic, unidirectional single-mode Nd: YAG ring laser.* Optics letters, Vol. 10, No. 2, (1985) 65–67.

[Kha04] E. Khazanov, N. Andreev, A. Mal'shakov et al. *Compensation of thermally induced modal distortions in Faraday isolators.* IEEE Journal of Quantum Electronics, Vol. 40, No. 10, (2004) 1500–1510.

[Kim91] K. S. Kim, H. J. Kong, and C. J. Kim. *Measurement of the temperature and the pumping uniformity inside a Nd:YAG rod by an interferometric method.* Applied Physics Letters, Vol. 58, No. 17, (1991) 1810–1812.

[Kim10] H. Kim, P. King, C. Krämer et al. *PSL Final Design.* LIGO technical document, LIGO-T0900649-v4.

[Kno98] S. Knoke. *Einfrequenzbetrieb von diodengepumpten Nd:YAG-Hochleistungslasern in Stab-und Slabgeometrie.* Dissertation, University Hannover (1998).

[Koe70] W. Koechner. *Thermal lensing in a Nd: YAG laser rod.* Applied Optics, Vol. 9, No. 11, (1970) 2548–2553.

[Kog65] H. Kogelnik. *On the propagation of Gaussian beams of light through lenslike media including those with a loss or gain variation.* Applied Optics, Vol. 4, No. 12, (1965) 1562–1569.

[Kog66] H. Kogelnik and T. Li. *Laser beams and resonators.* Applied Optics, Vol. 5, No. 10, (1966) 1550–1567.

[Kra94] A. Krajewski and P. Mazzinghi. *Study of the reflectivity of ceramic materials for laser-cavity mirrors.* Journal of materials science, Vol. 29, No. 1, (1994) 232–238.

[Kra05] D. Kracht, R. Wilhelm, M. Frede et al. *407 W End-pumped Multi-segmented Nd:YAG Laser.* Optics Express, Vol. 13, No. 25, (2005) 10140–10144.

[Kug97] N. Kugler, S. Dong, Q. Lü et al. *Investigation of the misalignment sensitivity of a birefringence-compensated two-rod Nd:YAG laser system.* Applied Optics, Vol. 36, No. 36, (1997) 9359–9366.

[Kuh09] V. Kuhn, P. Weßels, J. Neumann et al. *Stabilization and power scaling of cladding pumped Er:Yb-codoped fiber amplifier via auxiliary signal at 1064 nm.* Optics Express, Vol. 17, No. 20, (2009) 18304–18311.

[Kuh10] V. Kuhn, S. Unger, S. Jetschke et al. *Experimental Comparison of Fundamental Mode Content in Er:Yb-Codoped LMA Fibers With Multifilament- and Pedestal-Design Cores.* Journal of Lightwave Technology, Vol. 28, No. 22, (2010) 3212–3219.

[Kuh11] V. Kuhn, D. Kracht, J. Neumann et al. *67 W of Output Power From an Yb-Free Er-Doped Fiber Amplifier Cladding Pumped at 976 nm.* IEEE Photonics Technology Letters, Vol. 23, No. 7.

[Kwe07] P. Kwee, F. Seifert, B. Willke et al. *Laser beam quality and pointing measurement with an optical resonator.* Review of Scientific Instruments, Vol. 78, (2007) 073103.

[Kwe09] P. Kwee, B. Willke, and K. Danzmann. *Shot-noise-limited laser power stabilization with a high-power photodiode array.* Optics Letters, Vol. 34, No. 19, (2009) 2912–2914.

[Lör75] J. P. Lörtscher, J. Steffen, and G. Herziger. *Dynamic stable resonators: a design procedure.* Optical and Quantum Electronics, Vol. 7, (1975) 505–514.

[Lü95a] Q. Lü, S. Dong, and H. Weber. *Analysis of TEM_{00} laser beam quality degradation caused by a birefringent Nd:YAG rod.* Optical and Quantum Electronics, Vol. 27, No. 9, (1995) 777–783.

[Lü95b] Q. Lü, U. Wittrock, and S. Dong. *Photoelastic effects in Nd:YAG rod and slab lasers.* Optics and Laser Technology, Vol. 27, No. 2, (1995) 95–101.

[Lü96] Q. Lü, N. Kugler, H. Weber et al. *A novel approach for compensation of birefringence in cylindrical Nd: YAG rods.* Optical and Quantum Electronics, Vol. 28, No. 1, (1996) 57–69.

[Mag86] V. Magni. *Resonators for solid-state lasers with large-volume fundamental mode and high alignment stability.* Applied Optics, Vol. 25, No. 1, (1986) 107–117.

[Mag91] V. Magni, G. Valentini, and S. Silvestri. *Recent developments in laser resonator design.* Optical and Quantum Electronics, Vol. 23, (1991) 1105–1134. 10.1007/BF00619980.

[Mat] *Material properties data at `www.matweb.com`.*

[Mic87] A. Michelson and E. Morley. *LVIII. On the relative motion of the earth and the luminiferous Æther.* Philosophical Magazine Series 5, Vol. 24, No. 151, (1887) 449–463.

[Mor07] B. Morasse, S. Agger, S. Chatigny et al. *10W ASE-free single mode high power double cladding Er^{3+}-Yb^{3+} amplifier.* In *Proc. SPIE*, Vol. 6453, 645324 (2007).

[Mue03] G. Mueller, T. Delker, D. Tanner et al. *Dual-recycled cavity-enhanced Michelson interferometer for gravitational-wave detection.* Applied Optics, Vol. 42, (2003) 1257–1268.

[Mur96] M. Murdough and C. Denman. *Mode-volume and pump-power limitations in injection-locked TEM$_{00}$ Nd:YAG rod lasers.* Applied Optics, Vol. 35, No. 30, (1996) 5925–5936.

[Nab89] C. D. Nabors, A. D. Farinas, T. Day et al. *Injection locking of a 13-W cw Nd:YAG ring laser.* Optics Letters, Vol. 14, No. 21, (1989) 1189–1191.

[Pec72] E. Peck and K. Reeder. *Dispersion of air.* Journal of the Optical Society of America, Vol. 62, No. 8, (1972) 958–962.

[Pen01] X. Peng, A. Asundi, Y. Chen et al. *Study of the Mechanical Properties of Nd:YVO4 Crystal by use of Laser Interferometry and Finite-Element Analysis.* Applied Optics, Vol. 40, No. 9, (2001) 1396–1403.

[Pen04] X. Peng, L. Xu, and A. Asundi. *Thermal lensing effects for diode-end-pumped Nd:YVO$_4$ and Nd:YAG lasers.* Optical Engineering, Vol. 43, No. 10, (2004) 2454–2461.

[Pir56] F. Pirani. *On the physical significance of the Riemann tensor.* Acta Physica Polonica, Vol. 15, (1956) 389–405.

[Pöl10] J. Pöld. *aLIGO bow-tie Pre-Modecleaner document.* LIGO technical document, LIGO-T0900619-v2.

[Pun11] O. Puncken. *Pumpkopfdesign für advanced LIGO.* Dissertation, Leibniz Universität Hannover, Fachbereich Physik (2011).

[Sau94] P. Saulson. *Fundamentals of interferometric gravitational wave detectors* (World Scientific, 1994).

[Sav98] R. Savage, P. King, and S. Seel. *A highly stabilized 10-watt Nd:YAG laser for the laser interferometer gravitational-wave observatory (LIGO).* Laser Phys, Vol. 8, (1998) 679–685.

[Sch98] W. Schöne. *Theoretische und experimentelle Untersuchung thermischer Effekte in diodengepumpten Hochleistungs-Nd:YAG-Stablasern.* Dissertation, Universität Hannover (1998).

[Sco72] W. Scott and M. De Wit. *BIREFRINGENCE COMPENSATION AND TEM$_{00}$ MODE ENHANCEMENT IN A Nd:YAG LASER.* Applied Physics Letters, Vol. 18, No. 1, (1972) 3–4.

[Sei06] F. Seifert, P. Kwee, M. Heurs et al. *Laser power stabilization for second-generation gravitational wave detectors.* Optics letters, Vol. 31, No. 13, (2006) 2000–2002.

[Shi08] A. Shirakawa, H. Suzuki, M. Tanisho et al. *Yb-ASE-free Er amplification in short-wavelength filtered Er: Yb photonic-crystal fiber.* In *Optical Fiber Communication Conference* (Optical Society of America, 2008).

[Sie86] A. Siegman. *Lasers* (University Science Books, 1986).

[Sov07] M. Sovizi and R. Massudi. *Thermal distribution calculation in diode pumped Nd:YAG laser rod by boundary element method.* Optics and Laser Technology, Vol. 39, No. 1, (2007) 46–52.

[Str91] K. A. Strain and B. J. Meers. *Experimental demonstration of dual recycling for interferometric gravitational-wave detectors.* Physics Review Letters, Vol. 66, (1991) 1391–1394.

[Tay76] J. Taylor, R. Hulse, L. Fowler et al. *Further observations of the binary pulsar PSR 1913+ 16.* The Astrophysical Journal, Vol. 206, (1976) L53–L58.

[Tid92] S. Tidwell, J. Seamans, M. Bowers et al. *Scaling CW diode-end-pumped Nd:YAG lasers to high average powers.* IEEE Journal of Quantum Electronics, Vol. 28, No. 4, (1992) 997–1009.

[Tsu97] M. Tsunekane, N. Taguchi, T. Kasamatsu et al. *Analytical and experimental studies on the characteristics of composite solid-state laser rods in diode-end-pumped geometry.* IEEE Journal of selected Topics in Quantum Electronics, Vol. 3, No. 1, (1997) 9–18.

[Web60] J. Weber. *Detection and Generation of Gravitational Waves.* Phys. Rev., Vol. 117, No. 1, (1960) 306–313.

[Web98] R. Weber, B. Neuenschwander, M. Mac Donald et al. *Cooling schemes for longitudinally diode laser-pumped Nd:YAG rods.* IEEE Journal of Quantum Electronics, Vol. 34, No. 6, (1998) 1046–1053.

[Wei72] R. Weiss. *Electromagnetically coupled broadband gravitational antenna.* MIT Res. Lab. Electron. Q. Prog. Rep, Vol. 105, (1972) 54–76.

[Wil98] B. Willke, N. Uehara, E. K. Gustafson et al. *Spatial and temporal filtering of a 10-W Nd:YAG laser with a Fabry–Perot ring-cavity premode cleaner.* Optics Letters, Vol. 23, No. 21, (1998) 1704–1706.

[Wil02] B. Willke, P. Aufmuth, C. Aulbert et al. *The GEO 600 gravitational wave detector.* Classical and Quantum Gravity, Vol. 19, (2002) 1377–1387.

[Wil08] R. Wilhelm, M. Frede, and D. Kracht. *Power Scaling of End-Pumped Solid-State Rod Lasers by Longitudinal Dopant Concentration Gradients.* IEEE Journal of Quantum Electronics, Vol. 44, No. 3, (2008) 232–244.

[Wil09] R. Wilhelm, D. Freiburg, M. Frede et al. *Design and comparison of composite rod crystals for power scaling of diode end-pumped Nd:YAG lasers.* Optics Express, Vol. 17, No. 10, (2009) 8229–8236.

[Wil10] B. Willke. *Stabilized lasers for advanced gravitational wave detectors.* Laser & Photonics Reviews, Vol. 4, No. 6, (2010) 780–794.

[Yan96] S. T. Yang, Y. Imai, M. Oka et al. *Frequency-stabilized, 10-W continuous-wave, laser-diode end-pumped, injection-locked Nd:YAG laser.* Optics Letters, Vol. 21, No. 20, (1996) 1676–1678.

[YJ06] T. Yu-Jia, H. Xiu-Lan, and L. Zhi-Gang. *Numerical Simulation of the Non-Fourier Heat Conduction in a Solid-State Laser Medium.* Chinese Physics Letters, Vol. 23, No. 9, (2006) 2487.

[Yus05] A. Yusim, J. Barsalou, D. Gapontsev et al. *100 watt single-mode CW linearly polarized all-fiber format 1.56 µm laser with suppression of parasitic lasing effects.* In *Proceedings of SPIE*, Vol. 5709, 69 (2005).

[Zaw02] I. Zawischa, M. Brendel, K. Danzmann et al. *The GEO 600 laser system.* Classical and Quantum Gravity, Vol. 19, (2002) 1775.

Publications and Conferences

J. Abadie, ... L. Winkelmann, and ... et al. [1] *All-sky search for gravitational-wave bursts in the joint LIGO-GEO-Virgo run.* Physical Review D, Vol. 81, (2010) 102001–1–20.

J. Abadie, ... L. Winkelmann, and ... et al. [1] *Calibration of the LIGO gravitational wave detectors in the fifth science run.* Nuclear Instruments and Methods A, Vol. 624, (2010) 223–240.

J. Abadie, ... L. Winkelmann, and ... et al. [1] *First search for gravitational waves from the youngest known Neutron star.* The Astrophysical Journal, Vol. 722, No. 2, (2010) 1504–1513.

J. Abadie, ... L. Winkelmann, and ... et al. [1] *First Search for Gravitational Waves from the Youngest Known Neutron Star.* The Astrophysical Journal, Vol. 722, No. 2, (2010) 1504.

J. Abadie, ... L. Winkelmann, and ... et al. [1] *Predictions for the rates of compact binary coalescences observable by ground-based gravitational-wave detectors.* Classical Quantum Gravity, Vol. 27, No. 17, (2010) 173001–1–25.

J. Abadie, ... L. Winkelmann, and ... et al. [1] *Search for gravitational-wave inspiral signals associated with short gamma-ray bursts during LIGO's fifth and VIRGO's first science run.* The Astrophysical Journal, Vol. 715, (2010) 1453–1461.

J. Abadie, ... L. Winkelmann, and ... et al. [1] *Search for gravitational waves from compact binary coalescence in LIGO and Virgo data from S5 and VSR1.* Phys. Rev. D, Vol. 82, (2010) 102001.

J. Abadie, ... L. Winkelmann, and ... et al. [1] *Beating the Spin-down Limit on Gravitational Wave Emission from the Vela Pulsar.* The Astrophysical Journal, Vol. 737, No. 2, (2011) 93.

---

[1]The complete author list can be found at `https://dcc.ligo.org/public/0002/T0900264/002/authors_list_ApJ.pdf`.

J. Abadie, ... L. Winkelmann, and ... et al. [1] *Search for Gravitational Wave Bursts from Six Magnetars.* The Astrophysical Journal Letters, Vol. 734, No. 2, (2011) L35.

J. Abadie, ... L. Winkelmann, and ... et al. [1] *Search for gravitational waves associated with the August 2006 timing glitch of the Vela pulsar.* Physical Review D, Vol. 83, No. 4, (2011) 042001–1–13.

J. Abadie, ... L. Winkelmann, and ... et al. [1] *Search for gravitational waves from binary black hole inspiral, merger, and ringdown.* Phys. Rev. D, Vol. 83, (2011) 122005.

B. Abbott, ... L. Winkelmann, and ... et al. [1] *An upper limit on the Amplitude of Stochastic Gravitational-Wave Background of Cosmological Origin.* Nature, Vol. 460, (2009) 990–994.

B. Abbott, ... L. Winkelmann, and ... et al. [1] *Einstein@Home search for periodic gravitational waves in early S5 LIGO data.* Physical Review D, Vol. 80, (2009) 042003.

B. Abbott, ... L. Winkelmann, and ... et al. [1] *First LIGO search for gravitational wave bursts from cosmic (super)strings.* Physical Review D, Vol. 80, (2009) 062002–1–11.

B. Abbott, ... L. Winkelmann, and ... et al. [1] *LIGO: the Laser Interferometer Gravitational-Wave Observatory.* Reports on progress in physics, Vol. 72, (2009) 076901.

B. Abbott, ... L. Winkelmann, and ... et al. [1] *Search for gravitational-wave bursts in the first year of the fifth LIGO science run.* Physical Review D, Vol. 80, (2009) 102001–1–26.

B. Abbott, ... L. Winkelmann, and ... et al. [1] *Search for gravitational wave ringdowns from perturbed black holes in LIGO S4 data.* Phys. Rev. D, Vol. 80, (2009) 062001.

B. Abbott, ... L. Winkelmann, and ... et al. [1] *Search for gravitational waves from low mass binary coalescences in the first year of LIGO's S5 data.* Physical Review D, Vol. 79, (2009) 122001.

B. Abbott, ... L. Winkelmann, and ... et al. [1] *Search for gravitational waves from low mass compact binary coalescence in 186 days of LIGO's fifth science run.* Physical Review D, Vol. 80, (2009) 047101–1–7.

B. Abbott, ... L. Winkelmann, and ... et al. [1] *Search for high frequency gravitational-wave bursts in the first calendar year of LIGO's fifth science run.* Physical Review D, Vol. 80, (2009) 102002–1–14.

B. Abbott, ... L. Winkelmann, and ... et al. [1] *Stacked search for gravitational waves from the 2006 SGR 1900+14 storm.* The Astrophysical Journal, Vol. 701, No. 2, (2009) L68–L74.

B. Abbott, ... L. Winkelmann, and ... et al. [1] *Search for gravitational-wave bursts associated with gamma-ray bursts using data from LIGO science run 5 and VIRGO science run 1.* The Astrophysical Journal, Vol. 715, (2010) 1438–1452.

B. Abbott, ... L. Winkelmann, and ... et al. [1] *Searches for gravitational waves from known pulsars with science run 5 LIGO data.* The Astrophysical Journal, Vol. 713, (2010) 671–685.

D. Buskulic, ... L. Winkelmann, and ... et al. [1] *Very low latency search for low mass compact binary coalescences in the LIGO S6 and Virgo VSR2 data.* In *Classical and Quantum Gravity*, Vol. 27, 194013 (Rome, Italie, 2010).

M. Frede, L. Winkelmann, O. Puncken et al. *Status of AdvLIGO laser program.* LSC Meeting, March 20–23, 2007, Livingston LA (2007).

P. Kwee, B. Willke, L. Winkelmann et al. *Stabilized high-power laser system for the gravitational wave detector advanced LIGO.* Optics Express, Vol. 20, No. 10, (2012) 10617–10634.

O. Puncken, L. Winkelmann, R. Wilhelm et al. *Modenselektiv gepumptes Zweikopflasersystem mit Doppelbrechungskompensation.* DPG-Meeting March 2006, Frankfurt (2006).

O. Puncken, L. Winkelmann, M. Frede et al. *Status of the Advanced LIGO Laser.* LSC/Virgo Collaborations Meeting, March 17–20, 2008, Arcadia CA (2008).

O. Puncken, L. Winkelmann, C. Veltkamp et al. *Status of the advanced LIGO high power oscillator.* LSC/Virgo Collaborations Meeting, March 13–18, 2010, Arcadia CA (2010).

O. Puncken, L. Winkelmann, C. Veltkamp et al. *Status of the advanced LIGO PSL.* LSC/Virgo Collaborations Meeting, March 13–18, 2010, Arcadia CA (2010).

P. Weßels, L. Winkelmann, O. Puncken et al. *Advanced LIGO laser development.* LSC Meeting, October 20 – 26, 2007, Hannover (2007).

B. Willke, K. Danzmann, M. Frede et al. *Stabilized lasers for advanced gravitational wave detectors.* Classical and Quantum Gravity, Vol. 25, No. 11, (2008) 114040.

L. Winkelmann, M. Frede, R. Wilhelm et al. *50 Watt Laser Concepts for Initial LIGO.* LSC Meeting, March 20–23, 2005, Livingston LA (2005).

L. Winkelmann, M. Frede, O. Puncken et al. *Adv-LIGO Laser Status.* LSC Meeting, March 19–22, 2006, Hanford WA (2006).

L. Winkelmann, M. Frede, R. Wilhelm et al. *Einfrequenter Nd:YAG-Laser für die nächste Generation erdgebundener Gravitationswellendetektoren.* DPG-Meeting March 2006, Frankfurt (2006).

L. Winkelmann, D. Kracht, O. Puncken et al. *Solid state lasers for gravitational-wave detection.* 17th International Laser Physics Workshop, June 30 – July 4, 2008, Trondheim, Norway (2008).

L. Winkelmann, O. Puncken, B. Schulz et al. *Mode discrimination in injection locked high-power single-frequency lasers.* In *Conference on Lasers and Electro-Optics* (Optical Society of America, 2008).

L. Winkelmann, O. Puncken, R. Kluzik et al. *The 200 W Laser Engineering Prototype.* LSC/Virgo Collaborations Meeting, March 14–19, 2009, Arcadia CA (2009).

L. Winkelmann, O. Puncken, C. Veltkamp et al. *210 W single-frequency laser with 88% of output power in TEM00 mode for Advanced LIGO.* In *Laser Science* (Optical Society of America, 2009).

L. Winkelmann, O. Puncken, M. Frede et al. *Einfrequentes Lasersystem mit 210W Ausgangsleistung für die nächste Generation von Gravitationswellendetektoren.* DPG-Meeting March 2010, Hannover (2010).

L. Winkelmann, O. Puncken, R. Kluzik et al. *Injection-locked single-frequency laser with an output power of 220 W.* Applied Physics B: Lasers and Optics, Vol. 102, No. 3, (2011) 529–538.

Curriculum vitae

Personal information

Name:	Lutz Winkelmann
Address:	Bargteheider Str. 229
City, ZIP:	Hamburg, 22143
Date of birth:	1979/09/18
Place of birth:	Oelde, Germany
Citizenship:	German
Gender:	male
Cell phone:	+49-170-8792454
Email:	mailto:L.winkelmann@gmx.de

Education

1986 – 1990	Marien Grundschule Oelde
1990 – 1999	Thomas-Morus-Gymnasium Oelde
2000 – 2004	Univerisity of Applied Science Münster with degree Dipl.-Ing.(FH) in Applied Physics

Employment history

November 1st 1999 – August 31st 2000	German military service
May 31st – August 22nd 2003	Internship at F.O.R.T.H. Crete/Greece
April 1st – September 31st 2004	Diploma Thesis at Tesat Spacecom GmbH & Co. KG
January 1st 2005 until present	PhD at the Laser Zentrum Hannover e.V.

Acknowledgment

When I started my doctoral studies at the Laser Zentrum Hannover e.V. in the Laser Development group, I never imagined how outstanding and interesting being part of a huge collaboration for the detection of gravitational waves would be. In particular the contact with so many experts in gravitational wave, and laser physics, mechanics and instrument science have been an experience I never want to miss.

First of all I want to thank my supervisor Prof. Ludger Overmeyer and my co-assessor Prof. Uwe Morgner from the Leibniz University Hannover for their support over the recent years.

A special thank goes to all the people, which contributed to the development of the single-frequency high power laser for the Advanced LIGO detector. I would like to thank Dr. Dietmar Kracht and Dr. Jörg Neumann from the Laser Zentrum Hannover e.V., who gave me the opportunity to work in the laser development group, providing excellent working conditions and an enjoyable working environment. I want to thank Dr. Maik Frede and Dr. Peter Weßels for their mentoring and scientific guidance within the recent years.

A very special thank goes to Dr. Oliver Puncken, who shared my fate in working on his doctoral thesis within the same project. It was always fun to work with him in the laboratory, have a discussion about scientific or non so scientific topics.

Furthermore I am grateful to all my colleges of the Solid State Photonics and the Single Frequency Lasers working group and especially Christian Veltkamp, Rebecca Wachter, Matthias Janssen, Matthias Hildebrandt, Sascha Wagner, Raphael Kluzik, Marcin Damjanic, and Bastian Schulz, which made my work at the Laser Zentrum Hannover such a good and enjoyable time. In addition I want to thank Dr. Benno Willke from the Max-Planck Institute of Gravitational Physics in Hannover and his laser development group, namely Frank Seifert, Patrick Kwee, Jan Poeld, and Christina Bogan for their extended support. It was always a pleasure to work with all of you.

A special thank goes out to Dr. Peter King from the California Institute of Technology, who became a good friend during several laser alignment sessions in laboratory seven. He also contributed a lot to this thesis by proofreading, which I am particularly grateful for.

Finally a very special thank goes out to my family for their extensive support during the recent years and beyond. In particular I want to thank my wife Anika for lightening the load of being a father for a new born child and writing this thesis.